Copyright Warning & Restrictions

The copyright law of the United States (Title 17, United States Code) governs the making of photocopies or other reproductions of copyrighted material.

Under certain conditions specified in the law, libraries and archives are authorized to furnish a photocopy or other reproduction. One of these specified conditions is that the photocopy or reproduction is not to be "used for any purpose other than private study, scholarship, or research." If a, user makes a request for, or later uses, a photocopy or reproduction for purposes in excess of "fair use" that user may be liable for copyright infringement,

This institution reserves the right to refuse to accept a copying order if, in its judgment, fulfillment of the order would involve violation of copyright law.

Please Note: The author retains the copyright while the New Jersey Institute of Technology reserves the right to distribute this thesis or dissertation

Printing note: If you do not wish to print this page, then select "Pages from: first page # to: last page #" on the print dialog screen

NJIT New Jersey's Science & Technology University

The Van Houten library has removed some of the personal information and all signatures from the approval page and biographical sketches of theses and dissertations in order to protect the identity of NJIT graduates and faculty.

ABSTRACT

PERIODIC FAST MULTIPOLE METHOD

by
Ruqi Pei

Applications in electrostatics, magnetostatics, fluid mechanics, and elasticity often involve sources contained in a unit cell C, centered at the origin, on which periodic boundary condition are imposed. The free-space Green's functions for many classical partial differential equations (PDE), such as the modified Helmholtz equation, are well-known. Among the existing schemes for imposing the periodicity, three common approaches are: direct discretization of the governing PDE including boundary conditions to yield a large sparse linear system of equations, spectral methods which solve the governing PDE using Fourier analysis, and the method of images based on tiling the plane with copies of the unit cell and computing the formal solution. In the method of images, the lattice of image cells is divided into a "near" region consisting of the unit source cell and its nearest images and an infinite "far" region covered by the remaining images. Recently, two new approaches were developed to carry out calculation of the free-space Green's function over sources in the near region and correct for the lack of periodicity using an integral representation or a representation in terms of discrete auxiliary Green's functions. Both of these approaches are effective even for unit cells of high aspect ratio, but require the solution of a possibly ill-conditioned linear system of equations in the correction step.

In this dissertation, a new scheme is proposed to treat periodic boundary conditions within the framework of the fast multipole method (FMM). The scheme is based on an explicit, low-rank representation for the influence of all far images. It avoids the lattice sum/Taylor series formalism altogether and is insensitive to the aspect ratio of the unit cell. The periodizing operators are formulated with plane-wave factorizations that are valid for half spaces, leading to a simple fast algorithm. When the rank is large, a more elaborate algorithm using the Non-Uniform Fast

Fourier Transform (NUFFT) can further reduce the computational cost. The computation for modified Helmholtz case is explained in detail. The Poisson equation is discussed, with charge neutrality as a necessary constraint. Both the Stokes problem and the modified Stokes problem are formulated and solved. The full scheme including the NUFFT acceleration is described in detail and the performance of the method is illustrated with extensive numerical examples.

In the last chapter, another project about boundary integral equations is presented. Boundary integral equations and Nyström discretization methods provide a powerful tool for computing the solution of Laplace and Helmholtz boundary value problems (BVP). Using the fundamental solution (free-space Green's function) for these equations, such problems can be converted into boundary integral equations, thereby reducing the dimension of the problem by one. The resulting geometric simplicity and reduced dimensionality allow for high-order accurate numerical solutions with greater efficiency than standard finite-difference or finite-element discretizations. Integral equation methods require appropriate quadrature rules for evaluating the singular and nearly singular integrals involved. A standard approach uses a panel-based discretization of the curve and Generalized Gaussian Quadrature (GGQ) rules for treating singular and nearly-singular integrals separately, which correspond to a panel's interaction with itself and its neighbors, respectively. In this dissertation, a new panel-based scheme is developed which circumvents the difficulties of the nearly-singular integrals. The resulting rule is more efficient than standard GGQ in terms of the number of required kernel evaluations.

PERIODIC FAST MULTIPOLE METHOD

by
Ruqi Pei

A Dissertation
Submitted to the Faculty of
New Jersey Institute of Technology and
Rutgers, The State University of New Jersey - Newark
in Partial Fulfillment of the Requirements for the Degree of
Doctor of Philosophy in Mathematical Sciences

Department of Mathematical Sciences
Department of Mathematics and Computer Science, Rutgers-Newark

May 2022

Copyright © 2022 by Ruqi Pei

ALL RIGHTS RESERVED

APPROVAL PAGE

PERIODIC FAST MULTIPOLE METHOD

Ruqi Pei

Dr. Shidong Jiang, Dissertation Co-Advisor — Date
Professor of Mathematical Sciences, NJIT

Dr. Travis Askham, Dissertation Co-Advisor — Date
Assistant Professor of Mathematical Sciences, NJIT

Dr. Michael Siegel, Committee Member — Date
Professor of Mathematical Sciences, NJIT

Dr. Brittany D. Hamfeldt, Committee Member — Date
Associate Professor of Mathematical Sciences, NJIT

Dr. Leslie Greengard, Committee Member — Date
Professor of Mathematics, New York University, New York, NY

BIOGRAPHICAL SKETCH

Author: Ruqi Pei

Degree: Doctor of Philosophy

Date: May 2022

Undergraduate and Graduate Education:

- Doctor of Philosophy in Mathematical Sciences,
  New Jersey Institute of Technology, Newark, NJ, 2022
- Bachelor of Science in Mathematical Sciences
  Hawaii Pacific University, Honolulu, HI, 2017

Major: Mathematical Sciences

Publications:

Pei, R., Askham, T., Greengard, L., Jiang, S. (2021). Periodic fast multipole method. *arxiv.org*.
https://arxiv.org/abs/2111.01083

感谢我的爸爸妈妈的爱与支持!

I am grateful for my parents' love and support!

ACKNOWLEDGMENT

First and foremost, I would like to thank my advisors - Prof. Travis Askham and Prof. Shidong Jiang for their constant support both academically and personally, and their guidance over the last four years. Prof. Travis Askham has been very understanding and patient throughout the whole period. Prof. Shidong Jiang has been teach me over a broad range of topics, from the big picture of my dissertation project, to fine details in coding and writing, and very useful advice on my career path. I am extremely grateful to both of them.

I am also very grateful to Prof. Leslie Greengard for having suggested periodic fast multipole method as my thesis project. His deep insight on scientific computing and fast algorithms has had a great impact on my understanding of the thesis project and has largely shaped my style of thinking on applied and computational mathematics in general.

I would like to thank Prof. Michael Siegel and Prof. Brittany D. Hamfeldt, for agreeing to serve on my dissertation committee and for their careful reading of my proposal and dissertation.

Thanks to the Department of Mathematical Sciences at the New Jersey Institute of Technology for the teaching assistant support throughout my Ph.D. study, and to the National Science Foundation (Grant DMS-1720405) for funding my research assistantship during certain periods.

I am also thankful to Prof. Michael O'Neil, Dr. Manas Rachh and Dr.Zydrunas Gimbutas from whom I have learned a lot over the past few years and working with them has a very enriching and enjoyable experience. I would like to thank Clarisa Gonzalez-Lenahan for her unwavering support and constant encouragement throughout the course of the dissertation.

Special thanks go to my student mentor Axel Turnquist and other NJIT students including Kosuke Sugita, Connor Robertson, Lauren Barnes, Rituparna Basak, Gan Luan, Beibei Li, Atefeh Javidi, Yuexin Liu, Binan Gu, and Erli Wind-Andersen. They have made this journey a very memorable experience, helping me

see through tough times and sharing happy moments.

Finally, I would like to thank my beloved parents for their endless love and support.

TABLE OF CONTENTS

TABLE OF CONTENTS
(Continued)

LIST OF TABLES

Table **Page**

LIST OF FIGURES

PART 1

Figure **Page**

CHAPTER 1

INTRODUCTION

Applications in electrostatics, magnetostatics, fluid mechanics, and elasticity involve sources contained in a unit cell $\mathcal{C}$, centered at the origin, on which are imposed periodic boundary conditions. In two dimensions, define a unit cell by two fundamental translation vectors $\hat{\mathbf{e}}_1$ and $\hat{\mathbf{e}}_2$. In the doubly periodic case, without loss of generality, we assume $\|\hat{\mathbf{e}}_1\| \geq \|\hat{\mathbf{e}}_2\|$ and by rotation, we can have $\hat{\mathbf{e}}_1$ aligned with the x-axis and $\hat{\mathbf{e}}_2$ lie in the upper half space (see Figure 1.1). Let $\mathcal{C} = \left\{x_1\hat{\mathbf{e}}_1 + x_2\hat{\mathbf{e}}_2 \in \mathbb{R}^2 |\ x_1, x_2 \in [-\frac{1}{2}, \frac{1}{2}]\right\}$, where $\hat{\mathbf{e}}_1 = \langle d, 0\rangle$, $\hat{\mathbf{e}}_2 = \langle \xi, \eta\rangle$, with $d \geq \sqrt{\xi^2 + \eta^2}$ and $d, \eta > 0$. For the singly periodic case, we assume that the periodic direction is aligned with the x-axis without $\|\hat{\mathbf{e}}_1\| \geq \|\hat{\mathbf{e}}_2\|$. Without loss of generality, we can assume that the unit cell is rectangular and of dimension $d \times \eta$, see Figure 1.1. Let $\mathbf{t} = (x, y)$ and $u(\mathbf{t})$ denote a scalar quantity of interest. We define *doubly periodic* boundary conditions as:

$$\begin{aligned} u(\mathbf{t} + \hat{\mathbf{e}}_1) &= u(\mathbf{t}), \\ u(\mathbf{t} + \hat{\mathbf{e}}_2) &= u(\mathbf{t}). \end{aligned} \tag{1.1}$$

We define *singly periodic* boundary conditions as:

$$u(\mathbf{t} + \hat{\mathbf{e}}_1) = u(\mathbf{t}), \tag{1.2}$$

with a standard outgoing/decay condition in the y-direction.

Assuming we have a governing partial differential equation (PDE)

$$\Delta u(\mathbf{t}) - \beta^2 u(\mathbf{t}) = \sum_{j=1}^{N_S} q_j \delta(\mathbf{t} - \mathbf{s}_j), \tag{1.3}$$

with β non-negative and real and $\mathbf{t}, \mathbf{s}_j$ are points lying within the unit cell $\mathcal{C}$. Equation (1.3) is called modified Helmholtz equation when $\beta > 0$. When $\beta = 0$,

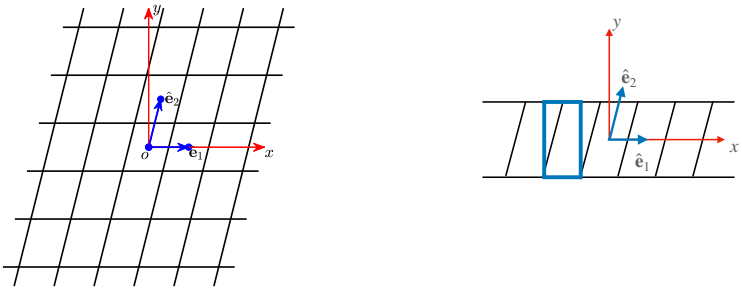

Figure 1.1 In the doubly periodic case (left), the unit cell is a parallelogram which tiles the entire plane. By convention, we assume that the lattice is oriented so that the longer cell dimension is aligned with the x-axis: $\|\hat{\mathbf{e}}_1\| \geq \|\hat{\mathbf{e}}_2\|$. In the singly periodic case (right), we assume the periodic direction is aligned with the x-axis. The unit cell may still be a parallelogram, but we can always define a corresponding rectangular unit cell, indicated by thick blue lines. In this case, we cannot assume that the long cell dimension is aligned with the x-axis. Periodic boundary conditions are imposed through the method of images: that is, by including the influence of the translated sources in every image cell on the targets in the fundamental unit cell.

Equation (1.3) becomes the Poisson equation. In two dimensions, the free-space Green's functions for these equations are well-known and given by (Mikhlin and Prossdorf, 1986; Stakgold, 1968)

$$\begin{aligned} G(\mathbf{t},\mathbf{s}) &= \frac{1}{2\pi} K_0(\beta\|\mathbf{t}-\mathbf{s}\|), \\ G(\mathbf{t},\mathbf{s}) &= \frac{1}{2\pi} \log(1/\|\mathbf{t}-\mathbf{s}\|). \end{aligned} \tag{1.4}$$

where K_0 refers to the zeroth order modified Bessel function of the second kind (Olver et al., 2010).

Therefore, in free space, the solution to Equation (1.3) at targets $\mathbf{t}_1, \ldots, \mathbf{t}_{N_T}$ can be written as

$$u^{(f)}(\mathbf{t}_i) = \sum_{j=1}^{N_S} G(\mathbf{t}_i, \mathbf{s}_j)\, q_j, \qquad i = 1, \ldots, N_T. \tag{1.5}$$

where $G(\mathbf{t},\mathbf{s})$ denotes the relevant free-space Green's function. Knowing the well-known fast multipole method (FMM) (Cheng et al., 1999; Greengard and Rokhlin, 1987; Greengard and Rokhlin, 1997; Ying et al., 2004) can reduce the computational cost of evaluating Equation (1.5) from $O(N_S \cdot N_T)$ to $O(N_S + N_T)$, with

a prefactor depending logarithmically on the desired precision, we consider this problem as a classical problem. We have three common approaches available for imposing periodicity. We can directly discretize governing PDE including boundary conditions to yield a large sparse linear system of equations or we can use spectral methods which solves Equation (1.3) using Fourier analysis or we can apply the method of images, based on tiling the plane with copies of a unit cell and computing the solution as:

$$u(\mathbf{t}_i) = \sum_{j=1}^{N_S} K^{(p)}(\mathbf{t}_i, \mathbf{s}_j) q_j \,, \tag{1.6}$$

where

$$K^{(p)}(\mathbf{t}, \mathbf{s}) = \sum_{(m,n)\in\mathbb{Z}^2} G(\mathbf{t}, \mathbf{s} + \mathbf{l}_{mn})$$

is the periodic Green's function and $\mathbb{Z}^2 = \{(m,n)|m,n \in \mathbb{Z}\}$ is the set of integer lattice points on the 2D plane and $\mathbf{l}_{mn} = m\hat{\mathbf{e}}_1 + n\hat{\mathbf{e}}_2$. This formal solution satisfies the PDE and the boundary conditions. For the modified Helmholtz equation, the $K^{(p)}(\mathbf{t}, \mathbf{s})$ is convergent. For the Poisson equation, the series is conditionally convergent.

The spectral approach is standard in quantum mechanics and solid-state physics (Ewald, 1921) (Bloch, 1928) (with earlier work in the mathematics literature by Floquet, Hill and others). Here, we focus on the method of images, using Equation (1.6), which is common in acoustics, electromagnetics, and fluid dynamics and dates back to Rayleigh (Rayleigh, 1892).

Definition 1. In the doubly periodic case, we decompose the two-dimensional integer lattice $\mathbb{Z}^2$ into $\Lambda_{near} = \{(m,n)|m \in \{-m_0, \ldots, m_0\}, n \in \{-1, 0, 1\}\}$ and $\Lambda_{far} = \mathbb{Z}^2 - \Lambda_{near}$. $m_0 = 1$ is sufficient for rectangular unit cells. In order to allow for parallelograms with arbitrarily small angles ($\xi \gg \eta$), it is sufficient to set $m_0 = 3$. The region covered by the unit cell $\mathcal{C}$ and its nearest images, indexed by Λ_{near}, will be referred to as the near field and denoted by $\mathcal{N}$. The region covered by the remaining image cells, indexed by Λ_{far}, will be referred to as the far field

and denoted by $\mathcal{F}$. For consistency in notation, in the singly periodic case, we define $\Lambda^{(1)}_{near} = \{(m,0)|m \in \{-1,0,1\}\}$ and $\Lambda^{(1)}_{far} = \{(m,0)|m \in \mathbb{Z}\} - \Lambda^{(1)}_{near}$.

Definition 2. In the two-dimensional case, we define the aspect ratio of the fundamental unit cell by $A = d/\eta$. Since we have chosen to orient the longer lattice vector $\hat{\mathbf{e}}_1$ with the x-axis, $A \geq 1$. The problem is computationally more involved when A is large. In the one-dimensional case, we define the aspect ratio by $A = \max(1, \eta/d)$ As we shall see below, it is again when A is large that the computation is most difficult. (See Figure 1.1.)

The singly or doubly periodic Green's function can be expressed as:

$$K^{(p)}(\mathbf{t},\mathbf{s}) = K^{near}(\mathbf{t},\mathbf{s}) \ + \ K^{far}(\mathbf{t},\mathbf{s}), \tag{1.7}$$

where

$$\begin{aligned} K^{near}(\mathbf{t},\mathbf{s}) &= \sum_{(m,n)\in\Lambda_{near}} G(\mathbf{t},\mathbf{s}+\mathbf{l}_{mn}) \\ K^{far}(\mathbf{t},\mathbf{s}) &= \sum_{(m,n)\in\Lambda_{far}} G(\mathbf{t},\mathbf{s}+\mathbf{l}_{mn}) \end{aligned} \tag{1.8}$$

Since the sources in $K^{far}(\mathbf{t},\mathbf{s})$ are far-distanced from the unit cell, we can express their contributions within the unit cell as a series

$$K^{far}(\mathbf{t},\mathbf{s}) = \sum_{l=-\infty}^{\infty} S_l I_l(\lambda\|\mathbf{t}-\mathbf{s}\|)e^{il\theta_{\mathbf{t},\mathbf{s}}} \tag{1.9}$$

with $\theta_{\mathbf{t},\mathbf{s}} = \arg(\mathbf{t}-\mathbf{s})$, where I_l is modified Bessel function of the first kind (Olver et al., 2010) and S_l is *lattice sum*

$$S_l = \sum_{(m,n)\in\Lambda_{far}} K_l(\lambda|\mathbf{l}_{mn}|)e^{il\phi_{mn}}, \tag{1.10}$$

with $\phi_{nm} = \arg(\mathbf{l}_{mn})$. (This is a straightforward application of the Graf addition theorem (Olver et al., 2010, §10.23).)

We omit the nearest image cells from $K^{far}(\mathbf{t},\mathbf{s})$ because the convergence behavior of the series expansion in Equation (1.9) is controlled by the distance

of the nearest source from the disk centered at the origin and enclosd in the unit cell, see Figure 1.2. The more images included in the near field, the faster the convergence rate of the local expansion.

When the unit cell has aspect ratio near or equal to 1, this yields an optimal scheme and is widely used in periodic versions of the fast multipole method (Berman and Greengard, 1994; Greengard and Rokhlin, 1987; Malhotra and Biros, 2015). In the work of Yan and Shelley (Yan and Shelley, 2018), this problem extends a three-dimensional (3D) version of the kernel-independent FMM library (Malhotra and Biros, 2015) to allow the imposition of periodicity on the unit cube in one, two or three directions. There are also many other works having a lot of dicussion in the context of the Poisson, Helmholtz and Maxwell equations, see (Berman and Greengard, 1994; Denlinger et al., 2017; Dienstfrey et al., 2001; Enoch et al., 2001; Huang, 1999; Linton, 2010; McPhedran et al., 2000; Moroz, 2006; Otani and Nishimura, 2008). The lattice sum-based approaches are comparably less efficient when the unit cell has comparably high aspect ratio. This is illustrated with a doubly periodic problem in Figure 1.2. Also, every source assigned to the far field must be in the exterior of the smallest disk enclosing the unit cell in order to ensure convergence of the local expansion. Therefore, one may have to redefine Λ_{far} to exclude a large number of image cells and redefine Λ_{near} to include those image cells and make a big modification over the underlying fast algorithm.

Remark 1. In the FMM, lattice sums are not used for the evaluation of $K^{far}(\mathbf{t}, \mathbf{s})$ for each source and target. Instead, given a multipole expansion for the unit cell, one constructs a single local expansion of the form

$$\sum_{l=-\infty}^{\infty} \alpha_l I_l(\lambda \|\mathbf{t}\|) e^{il\theta_{\mathbf{t}}} \tag{1.11}$$

that captures the field due to all sources in the far field $\mathcal{F}$ within the unit cell. This is a slight modification of Rayleigh's original method (Rayleigh, 1892). The

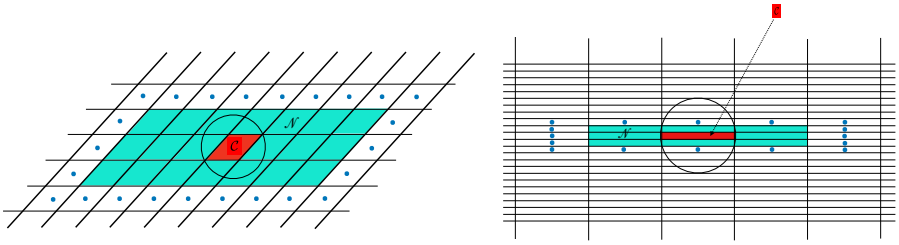

Figure 1.2 Two fundamental unit cells $\mathcal{C}$ in the doubly periodic case. On the left, the indicated 7×3 grid of neighbors define the near region $\mathcal{N}$ when the parameter $m_0 = 3$. On the right, when $m_0 = 1$, the near region corresponds to the 3×3 grid of neighbors, which is sufficient for rectangular lattices. We also plot the centers of the nearest image cells outside $\mathcal{N}$. Note that if the field due to distant images is represented in the unit cell by a Taylor series, the convergence behavior is controlled by the distance from the smallest disk covering the unit cell $\mathcal{C}$ to the nearest such image, which must lie *outside* the disk. For the geometry on the left, all image sources outside $\mathcal{N}$ satisfy this constraint and the Taylor series converges. For high aspect ratio cells, illustrated on the right, several of the images lie within the disk, and a region much larger than $\mathcal{N}$ must be excluded for the corresponding Taylor series to be convergent.

coefficients α_l are determined from the multipole coefficients through a formula which involves the lattice sums S_l.

Recently, two new approaches were developed that carry out a free space calculation of the form Equation (1.5) over sources in Λ_{near} and correct for the lack of periodicity using an integral representation (Barnett and Greengard, 2010; Barnett and Greengard, 2011) or a representation in terms of discrete auxiliary Green's functions, see (Barnett et al., 2018; Liu and Barnett, 2016; Wang et al., 2021). Both of these approaches are effective, even for the unit cells with high aspect ratio, but they require the solution of a possibly ill-conditioned linear system of equations in the correction step.

In this dissertation, we describe a new scheme to treat periodic boundary conditions based on an explicit, low-rank representation for the influence of all distant sources in the far field (those in image cells indexed by Λ_{far}). It not only avoids the lattice sum/Taylor series formalism altogether and but also is insensitive to the aspect ratio of the unit cell. It was motivated by, and makes use of, the fast algorithms for lattice sums and elliptic functions developed in previous work (Dienstfrey et al., 2001; Enoch et al., 2001; Huang, 1999; McPhedran et al., 2000)

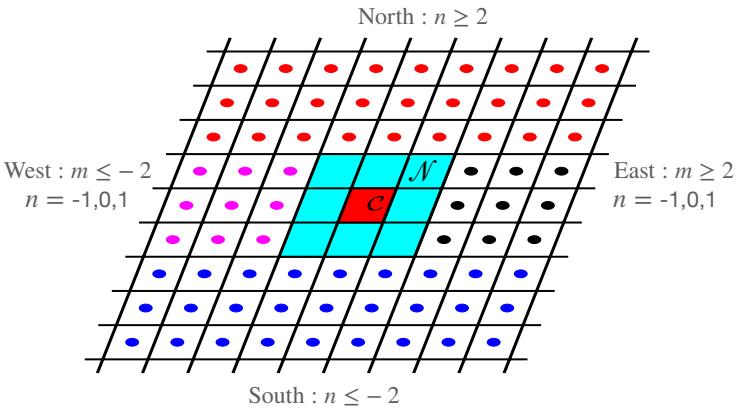

Figure 1.3 The tiling of the plane in the far region (for doubly periodic problems with $m_0 = 1$) can be decomposed into four parts. The fundamental unit cell is indicated by $\mathcal{C}$ and the near field by $\mathcal{N}$. All other copies of the unit cell lie to the "south" (blue, with $n \leq -2$), the "north" (red, with $n \geq 2$), the "west" (magenta, with $n = -1, 0, 1$ and $m < -1$) or the "east" (black, with $n = -1, 0, 1$ and $m > 1$).

and fast translation operators used in modern versions of the FMM (Cheng et al., 2006; Greengard and Rokhlin, 1997; Hrycak and Rokhlin, 1998).

The essence of this approach is illustrated in the doubly periodic setting (Figure 1.3), where the tiling of the far field is divided into four subregions.

Remark 2. To fix notation, we will denote by $\mathbf{t} = (x, y)$ or $\mathbf{t}_l = (x_l, y_l)$ the coordinates of a target point where we seek to evaluate the field. We will denote by $\mathbf{s} = (x', y')$ or $\mathbf{s}_j = (x'_j, y'_j)$ the coordinates of a source point.

Claim 1. Consider the field induced by all sources lying in image cells with centers lying to the "south": $\{(m, n) \in \mathbb{Z}^2 | m \in \mathbb{Z},\ n \leq -2\}$ (Figure 1.3). Then, for any target $\mathbf{t} \in \mathcal{C}$,

$$\begin{aligned} u(\mathbf{t}) &= \sum_{j=1}^{N_S} \left(\sum_{m=-\infty}^{\infty} \sum_{n=-\infty}^{-2} G(\mathbf{t}, \mathbf{s}_j + \mathbf{l}_{m,n}) \right) q_j \\ &= \sum_{m=-\infty}^{\infty} c_m \, e^{-\sqrt{(2\pi m/d)^2 + \beta^2} y} e^{2\pi i m x/d}, \end{aligned} \tag{1.12}$$

where

$$c_m = \frac{\pi}{d} \left(\frac{e^{-2\sqrt{(2\pi m/d)^2+\beta^2}\eta} e^{-4\pi i m \xi/d}}{1 - e^{-\sqrt{(2\pi m/d)^2+\beta^2}\eta} e^{-2\pi i m \xi/d}} \right) \sum_{j=1}^{N_S} q_j \frac{e^{\sqrt{(2\pi m/d)^2+\beta^2} y'_j} \, e^{-2\pi i m x'_j/d}}{\sqrt{(2\pi m/d)^2 + \beta^2}}.$$

The derivation of this formula will be described in detail in later sections,

but let us briefly examine its consequences. First, the behavior of the series is not controlled by a radius of convergence, as it is for methods based on lattice sums and Taylor series. Second, the series converges exponentially fast. Since $|y|, |y_j| \leq \frac{\eta}{2}$, it is easy to see that the mth term of the series decays faster than $e^{-2\pi m\eta/d}$. Clearly, approximately $6A$ terms yields double precision accuracy, where $A = d/\eta$ is the aspect ratio of the unit cell. Computing the moments c_m requires $O(N_S\, A)$ work. Subsequent evaluation at N_T target points again requires $O(N_T\, A)$ work. Overall, this is an efficient low-rank, separable representation of the potential due to a subset of the image sources, the rank of which grows at most linearly with A. When A is sufficiently large, we will show how to use the non-uniform FFT (NUFFT) (Barnett and Magland, 2018; Dutt and Rokhlin, 1993; Dutt and Rokhlin, 1995; Greengard and Lee, 2004; Lee and Greengard, 2005) to obtain an algorithm whose cost is of the order $O(\log(1/\epsilon)(A \log A + (N_S + N_T) \log(1/\epsilon)))$ with prescribed precion ϵ.

Below, we complete and generalize the representation Equation (1.12), permitting the imposition of periodic boundary conditions in one or two directions for a variety of non-oscillatory PDEs in the plane. We will denote by

$$K_2^{far}(\mathbf{t}, \mathbf{s}) = \sum_{(m,n)\in\Lambda_{far}} G(\mathbf{t}, \mathbf{s} + \mathbf{l}_{mn}) \tag{1.13}$$

the far-field kernel for doubly periodic problems. In the singly periodic case, we denote the corresponding far-field kernel by

$$K_1^{far}(\mathbf{t}, \mathbf{s}) = \sum_{(m,0)\in\Lambda_{far}^{(1)}} G(\mathbf{t}, \mathbf{s} + \mathbf{l}_{m0})\ . \tag{1.14}$$

Definition 3. Let $\mathbf{S} = \{\mathbf{s}_j \,|\, j = 1, \ldots, N_S\}$ and $\mathbf{T} = \{\mathbf{t}_l \,|\, l = 1, \ldots, N_T\}$ denote collections of sources and targets, respectively, in the unit cell $\mathcal{C}$ and let $\mathbf{q} = (q_1, \ldots, q_{N_S})$ denote a vector of "charge" strengths. With a slight abuse of notation, we define the $N_T \times N_S$ *periodizing operators* $\mathbf{P}_1 = \mathbf{P}_1^{\mathcal{C}}(\mathbf{T}, \mathbf{S})$ and

$\mathbf{P}_2 = \mathbf{P}_2^{\mathcal{C}}(\mathbf{T}, \mathbf{S})$ by

$$\mathbf{P}_1(l, j) = K_1^{far}(\mathbf{t}_l, \mathbf{s}_j)$$

and

$$\mathbf{P}_2(l, j) = K_2^{far}(\mathbf{t}_l, \mathbf{s}_j),$$

where the far field kernels K_1^{far} and K_2^{far} are given by Equation (1.13) and Equation (1.14). The vectors

$$\mathbf{P}_1\mathbf{q}, \quad \mathbf{P}_2\mathbf{q}$$

will be referred to as the *periodizing potentials*.

It is worth noting that our method yields an explicit, low-rank representation of the periodic Green's function, without the need to solve any auxiliary linear systems. In fact, the periodizing operators $\mathbf{P}_2, \mathbf{P}_1$ admit plane-wave factorizations of rank $O(A)$ similar to the formula for the "south" images described above, leading to simple fast algorithms for their evaluation. More precisely, letting $r = O(A)$ be the numerical rank of $\mathbf{P}_2$ or $\mathbf{P}_1$ to precision ε, a simple, direct method requires $O(r(N_S + N_T))$ work. When r is large, a more elaborate algorithm using the NUFFT requires only $O(\log(1/\epsilon)(r \log r + (N_S + N_T) \log(1/\epsilon)))$ work.

In Chapter 2, we review the mathematical and computational foundations of the method. In Chapter 3, we discuss the modified Helmholtz case in detail. In Chapter 4, we discuss the Poisson equation, where charge neutrality is a necessary constraint. The Stokes and modified Stokes problems are considered in Chapter 5. In Chapter 6, we describe the full scheme including NUFFT acceleration. We illustrate the performance of the method in Chapter 7 with several numerical examples and describe future extensions of the method in Chapter 8. An extension of our representation for multipole sources is provided in Appendix B and Appendix C.

CHAPTER 2

ANALYTICAL APPARATUS

2.1 The Poisson Summation Formula

Let $\hat{f}$ be the Fourier transform of f, that is,

$$\hat{f}(k) = \int_{\mathbb{R}} e^{-ikx} f(x) dx, \qquad f(x) = \frac{1}{2\pi} \int_{\mathbb{R}} e^{ikx} \hat{f}(k) dk. \tag{2.1}$$

The Poisson summation formula (for example, see (Dym and McKean, 1972)) states that

$$\sum_{n=-\infty}^{\infty} f\left(x + \frac{2\pi n}{h}\right) = \frac{h}{2\pi} \sum_{m=-\infty}^{\infty} \hat{f}(mh) e^{imhx}. \tag{2.2}$$

This formula holds for a wide class of functions, in particular, the Dirac delta function. In this case, we have (Jones, 1966)

$$\sum_{n=-\infty}^{\infty} \delta\left(x + \frac{2\pi n}{h}\right) = \frac{h}{2\pi} \sum_{m=-\infty}^{\infty} e^{imhx}. \tag{2.3}$$

2.2 Generalized Gaussian Quadrature For The Doubly Periodic Case

In evaluating the integrals in Equation 3.7 or Equation 3.9, we will require suitable quadrature rules. More generally, we would like efficient rules of the form

$$\begin{aligned} &\int_0^{\infty} \frac{e^{-\sqrt{\lambda^2+\beta^2}x}}{\sqrt{\lambda^2+\beta^2}} \left[M_1(\lambda) e^{i\lambda y} + M_1(-\lambda) e^{-i\lambda y}\right] d\lambda \\ &\approx \sum_{k=1}^{N} \frac{e^{-\sqrt{\lambda_k^2+\beta^2}x}}{\sqrt{\lambda_k^2+\beta^2}} \left[M_1(\lambda_k) e^{i\lambda_k y} + M_1(-\lambda_k) e^{-i\lambda_k y}\right] w_k \end{aligned}$$

and

$$\int_0^{\infty} e^{-\lambda z} M(\lambda) d\lambda \approx \sum_{k=1}^{N} e^{-\lambda_k z} M(\lambda_k) w_k$$

for (x, y) in a bounded domain of $\mathbb{R}^2$. The functions $M_1(\lambda)$ and $M(\lambda)$ here are smooth functions of λ that depend on the source locations and strengths and are derived from the infinite series that appear in the periodizing operators. The remaining cases in Equation 3.7 or Equation 3.9 are treated using the same nodes and weights. Because we have separated the near and far fields, we will be using these rules under restrictive conditions on x, y. As we shall see below in more detail, for the doubly periodic case we will typically invoke the quadrature under suitable rescaling so that $x \in [1, 7]$ and $y \in [-2, 2]$. Finding optimal weights and nodes for this restricted range of arguments leads to a nonlinear optimization problem which can be solved by what is known as generalized Gaussian quadrature (Bremer et al., 2010a; Ma et al., 1996; Yarvin and Rokhlin, 1998).

For the modified Hemholtz equation, if β is bounded away from zero, the integral converges and the number of nodes depends rather weakly on β itself. We note, however, that in the limit $\beta = 0$, the modified Helmholtz integral (for $x > 0$) becomes

$$\int_0^\infty \frac{e^{-\lambda x}}{\lambda}[M_1(\lambda)e^{i\lambda y} + M_1(-\lambda)e^{-i\lambda y}]d\lambda, \quad x > 0,$$

with $M_1(\lambda) = O(1/\lambda)$. Thus, significant adjustments would be required as $\beta \to 0$ to handle the near hypersingularity at the origin. In the present context, where we seek to impose periodicity, charge neutrality is a natural condition.

For the modified Helmholtz equation, special purpose quadratures have been constructed for β in different ranges. The number of quadrature nodes decreases as β increases. For $\beta \in [10^{-6}, +\infty)$, $x \in [1, 7]$, $y \in [-2, 2]$, at most 21 nodes have been found to yield six digits of accuracy and at most 41 nodes have been found to yield twelve digits of accuracy. When $\beta > 22$, only 1 node is sufficient for six digits of accuracy. When $\beta > 37$, 3 nodes are sufficient for twelve digits of accuracy. For the Poisson equation, with $x \in [1, 7]$, $y \in [-2, 2]$, 18 nodes yield six digits of accuracy and 29 nodes yield twelve digits of accuracy. We omit consideration of the modified Helmholtz equation when $\beta < 10^{-6}$ but charge neutrality is not satisfied, as this is a highly ill-conditioned problem. Assuming charge neutrality,

one may simply use the quadrauture designed for the Poisson equation.

2.3 The Non-Uniform Fast Fourier Transform

For high aspect ratio unit cells, we will require the evaluation of discrete Fourier transforms where the nodes, frequencies, or both are not uniformly spaced. By combining the standard fast Fourier transform (FFT) with careful analysis and fast interpolation techniques, these sums can be computed with nearly optimal computational complexity. The resulting algorithms are known as non-uniform fast Fourier transforms (NUFFTs). They were originally described in (Dutt and Rokhlin, 1993; Dutt and Rokhlin, 1995). We refer the reader to (Barnett and Magland, 2018; Barnett et al., 2019) for recent references and a state-of-the-art implementation.

The type-I NUFFT evaluates sums of the form

$$f_k = \sum_{j=1}^{N} c_j e^{ikx_j} \ , \ \text{for } k = -M, \ldots, M. \tag{2.4}$$

Letting $\mathbf{f} = (f_{-M}, \ldots, f_{M-1}, f_M)$ and letting $\mathbf{c} = (c_1, \ldots, c_N)$, we will write

$$\mathbf{f} = \mathbf{N}^{(1)}\mathbf{c}.$$

When the explicit dependence on the point locations $\{x_j\}$ and the number of Fourier modes M are needed, we will denote the operator $\mathbf{N}^{(1)}$ by $\mathbf{N}^{(1)}(\{x_j\}; M)$. The operator $\mathbf{N}^{(1)}$ can be applied using $O(M \log M + N \log(1/\epsilon))$ operations with nearly the same performance as the standard FFT.

Given the vector $\mathbf{f}$, The type-II NUFFT evaluates sums of the form

$$v_j = \sum_{k=-M}^{M} f_k e^{-ix_j k} \ , \ \text{for } j = 1, \ldots, N \ , \tag{2.5}$$

corresponding to the adjoint of $\mathbf{N}^{(1)}$:

$$\mathbf{v} = \mathbf{N}^{(2)}\mathbf{f},$$

with the same computational complexity, where $\mathbf{v} = (v_1, \ldots, v_N)$.

2.4 Legendre Polynomials And Barycentric Interpolation

The standard Legendre polynomials can be defined by setting $P_0 \equiv 1$ and $P_1(t) = t$, with higher degree polynomials defined by the recurrence formula

$$(l+1)P_{l+1}(t) = (2l+1)tP_l(t) - lP_{l-1}(t) \ .$$

Let $-1 < t_1 < \cdots < t_M < 1$ be the roots of P_M, known as the Legendre nodes of order M.

Letting f be a function defined on $[-1, 1]$, the degree $M-1$ polynomial, $p_M[f]$, which interpolates f at the Legendre nodes of order M, can be written in the form

$$p_M[f](t) = \frac{\sum_{i=1}^{M} \frac{\sigma_i}{t-t_i} f(t_i)}{\sum_{i=1}^{M} \frac{\sigma_i}{t-t_i}} \ , \tag{2.6}$$

where

$$\sigma_i = \frac{1}{\prod_{j \neq i} (t_i - t_j)} \ . \tag{2.7}$$

This is known as the second form of the barycentric formula for the interpolant.

As observed in (Wang and Xiang, 2012), if f is analytic in the Bernstein ellipse with foci at ± 1 and semi-major and semi-minor lengths adding up to $\rho > 1$, then

$$\|f - p_M[f]\|_\infty \leq (1 + \Lambda_M) \frac{2C}{\rho^M(\rho - 1)} \ , \tag{2.8}$$

where $\|\cdot\|_\infty$ is the maximum norm on $[-1, 1]$, C is a constant so that $|f| \leq C$ on the Bernstein ellipse, and $\Lambda_M = O(\sqrt{M})$ is the Lebesgue constant for the nodes.

Thus, the interpolant is a spectrally accurate approximation of f. See (Fornberg, 1998; Hesthaven et al., 2007; Trefethen, 2008; Wang and Xiang, 2012) for further details.

CHAPTER 3

PLANEWAVE EXPANSIONS OF VARIOUS KERNELS

3.1 The Helmholtz Kernel

The Sommerfeld integral representation (Sommerfeld and Strauss, 1949) for the first kind Hankel function of order zero states that

$$\frac{i}{4}H_0^{(1)}\left(\beta\sqrt{x^2+y^2}\right) = \begin{cases} \dfrac{1}{4\pi}\displaystyle\int_{-\infty}^{\infty} \frac{e^{-\sqrt{\lambda^2-\beta^2}y}}{\sqrt{\lambda^2-\beta^2}} e^{i\lambda x} d\lambda, & y > 0, \\ \dfrac{1}{4\pi}\displaystyle\int_{-\infty}^{\infty} \frac{e^{\sqrt{\lambda^2-\beta^2}y}}{\sqrt{\lambda^2-\beta^2}} e^{i\lambda x} d\lambda, & y < 0. \end{cases} \tag{3.1}$$

Similar expressions can be derived for left and right half planes. By applying the so-called raising operator $(\partial/\partial x + i\partial/\partial y)/(-\beta)$ l times on both sides of Equation 3.1, we obtain (McPhedran et al., 2000)

$$H_l^{(1)}\left(\beta\sqrt{x^2+y^2}\right)e^{il\phi} = \begin{cases} \dfrac{(-i)^{l+1}}{\pi\beta^l}\displaystyle\int_{-\infty}^{\infty} \left(\lambda - \sqrt{\lambda^2-\beta^2}\right)^l \frac{e^{-\sqrt{\lambda^2-\beta^2}y}}{\sqrt{\lambda^2-\beta^2}} e^{i\lambda x} d\lambda, & y > 0, \\ \dfrac{(-i)^{l+1}}{\pi\beta^l}\displaystyle\int_{-\infty}^{\infty} \left(\lambda + \sqrt{\lambda^2-\beta^2}\right)^l \frac{e^{\sqrt{\lambda^2-\beta^2}y}}{\sqrt{\lambda^2-\beta^2}} e^{i\lambda x} d\lambda, & y < 0, \end{cases} \tag{3.2}$$

with $\phi = \arg(x+iy)$.

Using the connection formula (Olver et al., 2010)

$$K_l(z) = \frac{\pi}{2} i^{l+1} H_l^{(1)}(iz), \tag{3.3}$$

we obtain

$$K_0\left(\beta\sqrt{x^2+y^2}\right) = \begin{cases} \dfrac{1}{2}\displaystyle\int_{-\infty}^{\infty} \frac{e^{-\sqrt{\lambda^2+\beta^2}y}}{\sqrt{\lambda^2+\beta^2}} e^{i\lambda x} d\lambda, & y > 0, \\ \dfrac{1}{2}\displaystyle\int_{-\infty}^{\infty} \frac{e^{\sqrt{\lambda^2+\beta^2}y}}{\sqrt{\lambda^2+\beta^2}} e^{i\lambda x} d\lambda, & y < 0, \end{cases} \tag{3.4}$$

and

$$K_l\left(\beta\sqrt{x^2+y^2}\right)e^{il\phi} = \begin{cases} \dfrac{i^l}{2\beta^l}\displaystyle\int_{-\infty}^{\infty}\left(\sqrt{\lambda^2+\beta^2}-\lambda\right)^l \dfrac{e^{-\sqrt{\lambda^2+\beta^2}y}}{\sqrt{\lambda^2+\beta^2}}e^{i\lambda x}d\lambda, & y>0, \\ \dfrac{(-i)^l}{2\beta^l}\displaystyle\int_{-\infty}^{\infty}\left(\sqrt{\lambda^2+\beta^2}+\lambda\right)^l \dfrac{e^{\sqrt{\lambda^2+\beta^2}y}}{\sqrt{\lambda^2+\beta^2}}e^{i\lambda x}d\lambda, & y<0, \end{cases} \tag{3.5}$$

respectively. For completeness, we also list the plane wave expansion for left and right half planes:

$$K_l\left(\beta\sqrt{x^2+y^2}\right)e^{il\phi} = \begin{cases} \dfrac{1}{2\beta^l}\displaystyle\int_{-\infty}^{\infty}\left(\sqrt{\lambda^2+\beta^2}+\lambda\right)^l \dfrac{e^{-\sqrt{\lambda^2+\beta^2}x}}{\sqrt{\lambda^2+\beta^2}}e^{i\lambda y}d\lambda, & x>0, \\ \dfrac{(-1)^l}{2\beta^l}\displaystyle\int_{-\infty}^{\infty}\left(\sqrt{\lambda^2+\beta^2}-\lambda\right)^l \dfrac{e^{\sqrt{\lambda^2+\beta^2}x}}{\sqrt{\lambda^2+\beta^2}}e^{i\lambda y}d\lambda, & x<0, \end{cases} \tag{3.6}$$

After all, the Green's function for the modified Bessel function, $K_0(\beta\sqrt{x^2+y^2})$, and its higher order multipole terms can be expressed as this Sommerfeld integral representation (Mores and Feshbach, 1953; McPhedran et al., 2000; Olver et al., 2010):

$$K_l\left(\beta\sqrt{x^2+y^2}\right)e^{il\phi} = \begin{cases} \dfrac{i^l}{2\beta^l}\displaystyle\int_{-\infty}^{\infty}\left(\sqrt{\lambda^2+\beta^2}-\lambda\right)^l \dfrac{e^{-\sqrt{\lambda^2+\beta^2}y}}{\sqrt{\lambda^2+\beta^2}}e^{i\lambda x}d\lambda, & y>0, \\ \dfrac{(-i)^l}{2\beta^l}\displaystyle\int_{-\infty}^{\infty}\left(\sqrt{\lambda^2+\beta^2}+\lambda\right)^l \dfrac{e^{\sqrt{\lambda^2+\beta^2}y}}{\sqrt{\lambda^2+\beta^2}}e^{i\lambda x}d\lambda, & y<0, \\ \dfrac{1}{2\beta^l}\displaystyle\int_{-\infty}^{\infty}\left(\sqrt{\lambda^2+\beta^2}+\lambda\right)^l \dfrac{e^{-\sqrt{\lambda^2+\beta^2}x}}{\sqrt{\lambda^2+\beta^2}}e^{i\lambda y}d\lambda, & x>0, \\ \dfrac{(-1)^l}{2\beta^l}\displaystyle\int_{-\infty}^{\infty}\left(\sqrt{\lambda^2+\beta^2}-\lambda\right)^l \dfrac{e^{\sqrt{\lambda^2+\beta^2}x}}{\sqrt{\lambda^2+\beta^2}}e^{i\lambda y}d\lambda, & x<0, \end{cases} \tag{3.7}$$

for $l \geq 0$.

3.2 The Laplace Kernel

The plane-wave expansion of the Green's function for the Laplacian is typically

invoked for the complex analytic function

$$\frac{1}{z} = \frac{1}{x+iy} = \frac{x-iy}{x^2+y^2} = -\left(\frac{\partial}{\partial x} - i\,\frac{\partial}{\partial y}\right)\log(1/\sqrt{x^2+y^2})\,,$$

rather than $\log(1/\sqrt{x^2+y^2})$ itself. This is sufficient for our purposes, where we assume the collection of sources in the unit cell $\mathcal{C}$ satisfies charge neutrality:

$$\sum_{j=1}^{N_S} q_j = 0. \tag{3.8}$$

In Appendix C, we will consider multipole sources as well as charge distributions, and will make use of the representations below. Let $z = x + iy \in \mathbb{C}$. Then

$$\frac{1}{z^l} = \begin{cases} \dfrac{1}{(l-1)!}\displaystyle\int_0^\infty \lambda^{l-1}e^{-\lambda z}d\lambda, & x > 0, \\ \dfrac{(-1)^l}{(l-1)!}\displaystyle\int_0^\infty \lambda^{l-1}e^{\lambda z}d\lambda, & x < 0, \\ \dfrac{(-i)^l}{(l-1)!}\displaystyle\int_0^\infty \lambda^{l-1}e^{i\lambda z}d\lambda, & y > 0, \\ \dfrac{i^l}{(l-1)!}\displaystyle\int_0^\infty \lambda^{l-1}e^{-i\lambda z}d\lambda, & y < 0. \end{cases} \tag{3.9}$$

for $l \geq 1$.These representations are useful in developing diagonal translation operators for FMMs (Cheng et al., 2006; Hrycak and Rokhlin, 1998) as well as for the computation of harmonic lattice sums and elliptic functions (Huang, 1999). Note that the integrals in Equation 3.9 are consistent with Equation 3.7 . In the case $l = 1$, for example, this requires taking the limit $\beta \to 0$ and using the formula (Olver et al., 2010, §10.30.2):

$$\lim_{\beta\to 0} \beta K_1(\beta r)e^{-i\theta} = \frac{1}{z}, \quad z = re^{i\theta}. \tag{3.10}$$

CHAPTER 4

PERIODICITY FOR THE MODIFIED HELMHOLTZ EQUATION

In this chapter, we consider the imposition of periodic boundary conditions for the two-dimensional modified Helmholtz equation with either one or two directions of periodicity. This requires an efficient scheme for the evaluation of the field due to all image sources in the far field (outside the nearest neighbors of $\mathcal{C}$). For simplicity, we fix $m_0 = 1$ when considering periodicity in the the $\hat{\mathbf{e}}_1 = (d, 0)$ direction alone and $m_0 = 3$ when considering periodicty in both the $\hat{\mathbf{e}}_1 = (d, 0)$ and $\hat{\mathbf{e}}_2 = (\xi, \eta)$ directions. Since the governing Green's function is exponentially decaying, all of the infinite series in the definition of the periodizing operators in Equation (3) converge absolutely.

Our algorithm is based on splitting the far field kernels into two parts for singly periodic case,

$$\begin{aligned} K_1^{west}(\mathbf{t}, \mathbf{s}) &= \sum_{m=-\infty}^{-2} G(\mathbf{t}, \mathbf{s} + (md, 0)), \\ K_1^{east}(\mathbf{t}, \mathbf{s}) &= \sum_{m=2}^{\infty} G(\mathbf{t}, \mathbf{s} + (md, 0)), \end{aligned} \tag{4.1}$$

and four parts (as in Figure 1.3) for the doubly periodic case:

$$\begin{aligned} K_2^{west}(\mathbf{t}, \mathbf{s}) &= \sum_{n=-1}^{1} \sum_{m=-\infty}^{-4} G(\mathbf{t}, \mathbf{s} + \mathbf{l}_{mn}), \\ K_2^{east}(\mathbf{t}, \mathbf{s}) &= \sum_{n=-1}^{1} \sum_{m=4}^{\infty} G(\mathbf{t}, \mathbf{s} + \mathbf{l}_{mn}), \\ K_2^{south}(\mathbf{t}, \mathbf{s}) &= \sum_{n=-\infty}^{-2} \sum_{m=-\infty}^{\infty} G(\mathbf{t}, \mathbf{s} + \mathbf{l}_{mn}), \\ K_2^{north}(\mathbf{t}, \mathbf{s}) &= \sum_{n=2}^{\infty} \sum_{m=-\infty}^{\infty} G(\mathbf{t}, \mathbf{s} + \mathbf{l}_{mn}). \end{aligned} \tag{4.2}$$

The corresponding operators will be denoted by $\mathbf{P}_1^{west}$, $\mathbf{P}_1^{east}$, $\mathbf{P}_2^{west}$, $\mathbf{P}_2^{east}$,

$\mathbf{P}_2^{south}$ and $\mathbf{P}_2^{north}$, so that

$$\begin{aligned} \mathbf{P}_1 &= \mathbf{P}_1^{west} + \mathbf{P}_1^{east}, \\ \mathbf{P}_2 &= \mathbf{P}_2^{west} + \mathbf{P}_2^{east} + \mathbf{P}_2^{south} + \mathbf{P}_2^{north}. \end{aligned} \tag{4.3}$$

Theorem 4.1. *Let* $\mathbf{S} = \{\mathbf{s}_j \,|\, j = 1, \ldots, N_S\}$ *and* $\mathbf{T} = \{\mathbf{t}_l \,|\, l = 1, \ldots, N_T\}$ *denote collections of sources and targets in the unit cell* $\mathcal{C}$ *and let* $\mathbf{P}_2^{south}$ *denote the* $N_T \times N_S$ *operator with* $\mathbf{P}_2^{south}(l, j) = K_2^{south}(\mathbf{t}_l, \mathbf{s}_j)$*. Given a precision* ϵ*, let*

$$M = \left\lceil \frac{d}{2\pi\eta} \log\left(\frac{1}{1 - e^{-\frac{2\pi\eta}{d}}} \frac{1}{\epsilon} \right) \right\rceil \approx \frac{A}{2\pi} (\log(A) + \log(1/\epsilon)). \tag{4.4}$$

For $m = -M, \ldots, M$*, let*

$$\alpha_m = \frac{2\pi m}{d}, \quad \chi_m = \sqrt{\alpha_m^2 + \beta^2}, \quad Q_m = \chi_m \eta - i\alpha_m \xi \,. \tag{4.5}$$

Let $\mathbf{L}^{south} \in \mathbb{C}^{N_T \times (2M+1)}$ *and* $\mathbf{R}^{south} \in \mathbb{C}^{(2M+1) \times N_S}$ *be dense matrices and let* $\mathbf{D}^{south} \in \mathbb{C}^{(2M+1) \times (2M+1)}$ *be a diagonal matrix with*

$$\begin{aligned} \mathbf{L}^{south}(l, m) &= e^{-\chi_m y_l} e^{i\alpha_m x_l} \,, \\ \mathbf{R}^{south}(m, j) &= e^{\chi_m y'_j} \, e^{-i\alpha_m x'_j} \,, \\ \mathbf{D}^{south}(m, m) &= \frac{1}{2d\,\chi_m} \frac{e^{-2Q_m}}{1 - e^{-Q_m}}. \end{aligned} \tag{4.6}$$

Then

$$\mathbf{P}_2^{south} = \mathbf{L}^{south}\, \mathbf{D}^{south}\, \mathbf{R}^{south} + O(\epsilon). \tag{4.7}$$

Proof. Combining Equation (3.7) and (4.2), we obtain

$$\begin{aligned} K_2^{south}(\mathbf{t},\mathbf{s}_j) &= \sum_{n=-\infty}^{-2}\sum_{m=-\infty}^{\infty}\int_{-\infty}^{\infty}\frac{e^{-\sqrt{\lambda^2+\beta^2}(y-y_j'-n\eta)}}{4\pi\sqrt{\lambda^2+\beta^2}}e^{i\lambda(x-x_j'-md-n\xi)}d\lambda \\ &= \sum_{n=-\infty}^{-2}\sum_{m=-\infty}^{\infty}\int_{-\infty}^{\infty}\frac{e^{-\sqrt{\lambda^2+\beta^2}(y-y_j'-n\eta)}}{\sqrt{\lambda^2+\beta^2}}e^{i\lambda(x-x_j'-n\xi)}\frac{1}{2d}\delta\left(\lambda-\frac{2\pi m}{d}\right)d\lambda \\ &= \sum_{n=-\infty}^{-2}\sum_{m=-\infty}^{\infty}\frac{1}{2d}\frac{e^{-\chi_m(y-y_j'-n\eta)}}{\chi_m}e^{i\alpha_m(x-x_j'-n\xi)}, \end{aligned} \tag{4.8}$$

where χ_m, α_m are given by Equation (4.5). The last two equalities follow from the Poisson summation formula Equation (2.3) and the Dirac delta function property. Exchanging the order of summation and summing the relevant geometric series in n leads to

$$K_2^{south}(\mathbf{t},\mathbf{s}_j) = \frac{1}{2d}\sum_{m=-\infty}^{\infty}\frac{e^{-\chi_m(y-y_j')+i\alpha_m(x-x_j')}}{\chi_m}\frac{e^{-2Q_m}}{1-e^{-Q_m}} \tag{4.9}$$

where Q_m is given in Equation (4.5).

Truncating the sum at $|m| = M$ yields the $(2M+1)$ term approximation

$$K_{2,M}{}^{south}(\mathbf{t},\mathbf{s}_j) = \frac{1}{2d}\sum_{m=-M}^{M}\frac{e^{-\chi_m(y-y_j')+i\alpha_m(x-x_j')}}{\chi_m}\frac{e^{-2Q_m}}{1-e^{-Q_m}} \tag{4.10}$$

and the formulas in Equation (4.6).

We now estimate the truncation error

$$E_s = |K_2{}^{south}(\mathbf{t},\mathbf{s}_j) - K_{2.M}{}^{south}(\mathbf{t},\mathbf{s}_j)|. \tag{4.11}$$

For any $m \in \mathbb{Z}$, it is easy to verify that

$$\chi_m \geq \frac{2\pi|m|}{d},\ \left|e^{-\chi_m(y-y_j)-Q_m}\right| = \left|e^{-\chi_m(\eta+y-y_j)}\right| \leq 1,$$

$$\left|e^{-Q_m}\right| \leq e^{-\chi_m\eta},\ \left|1-e^{-Q_m}\right| \geq 1-e^{-\chi_m\eta}.$$

From these bounds, it follows that

$$\begin{aligned} E_s &\leq \frac{1}{d} \sum_{m=M+1}^{\infty} \frac{1}{\chi_m} \frac{e^{-\chi_m \eta}}{1 - e^{-\chi_m \eta}} < \frac{1}{M+1} \frac{e^{-\frac{2\pi(M+1)\eta}{d}}}{1 - e^{-\frac{2\pi(M+1)\eta}{d}}} \sum_{k=0}^{\infty} e^{-\frac{2\pi k \eta}{d}} \\ &= \frac{1}{2\pi(M+1)} \frac{e^{-\frac{2\pi(M+1)\eta}{d}}}{\left(1 - e^{-\frac{2\pi(M+1)\eta}{d}}\right)\left(1 - e^{-\frac{2\pi\eta}{d}}\right)}. \end{aligned} \tag{4.12}$$

with M given by Equation (4.4). The estimate Equation (4.7) follows, completing the proof. □

Remark 3. Theorem 4.1 yields a truncated version of the formula in Equation (1.12) with weights $\mathbf{c} = (c_{-M}, c_{-M+1}, \ldots, c_{M-1}, c_M)$ given by

$$\mathbf{c} = \mathbf{D}^{south}\, \mathbf{R}^{south} \mathbf{q}\,,$$

where $\mathbf{q} = (q_1, \ldots, q_{N_S})$ is the vector of charge strengths.

Remark 4. When $\beta \gg 1$, the value of M in Equation (4.4) can be shown to be even smaller, but since the cost is logarithmic in A and ϵ we omit this more detailed analysis.

Remark 5. The observation that Poisson summation yields rapidly converging series approximations for lines or half spaces of lattice points that do not pass through the origin was made in (Enoch et al., 2001; McPhedran et al., 2000) for the purpose of computing lattice sums.

By applying the same analysis, we have

Corollary 1. *The matrix* $\mathbf{P}_2^{north}$ *has the low-rank factorization*

$$\mathbf{P}_2^{north} = \mathbf{L}^{north}\, \mathbf{D}^{north}\, \mathbf{R}^{north} + O(\epsilon)$$

where $\mathbf{D}^{north} = \overline{\mathbf{D}^{south}}$,

$$\begin{aligned} \mathbf{L}^{north}(l, m) &= e^{\chi_m y_l} e^{i\alpha_m x_l}\,, \\ \mathbf{R}^{north}(m, j) &= e^{-\chi_m y'_j}\, e^{-i\alpha_m x'_j}\,. \end{aligned} \tag{4.13}$$

Definition 4. Since the rank is precision-dependent, we say that $\mathbf{P}_2^{north}$ has an ϵ-rank of $2M+1$.

It remains to consider the "west" and "east" contributions.

Theorem 4.2. *Let $\mathbf{t}, \mathbf{s}_j$ lie in a unit cell $\mathcal{C}$ and $m_0 = 1$. Then, the kernels K_1^{west} and K_1^{east} have the integral representations*

$$\begin{aligned} K_1^{west}(\mathbf{t}, \mathbf{s}_j) &= \int_{-\infty}^{\infty} \frac{e^{-\sqrt{\lambda^2+\beta^2}(x-x'_j)}}{4\pi\sqrt{\lambda^2+\beta^2}} e^{i\lambda(y-y'_j)} \frac{e^{-2\sqrt{\lambda^2+\beta^2}d}}{1-e^{-\sqrt{\lambda^2+\beta^2}d}} d\lambda, \\ K_1^{east}(\mathbf{t}, \mathbf{s}_j) &= \int_{-\infty}^{\infty} \frac{e^{\sqrt{\lambda^2+\beta^2}(x-x'_j)}}{4\pi\sqrt{\lambda^2+\beta^2}} e^{i\lambda(y-y'_j)} \frac{e^{-2\sqrt{\lambda^2+\beta^2}d}}{1-e^{-\sqrt{\lambda^2+\beta^2}d}} d\lambda. \end{aligned} \tag{4.14}$$

Letting $m_0 = 3$ with the additional assumption with $d \geq \sqrt{\xi^2+\eta^2}$, the kernels K_2^{west} and K_2^{east} have the integral representations

$$\begin{aligned} K_2^{west}(\mathbf{t}, \mathbf{s}_j) &= \sum_{n=-1}^{1} \int_{-\infty}^{\infty} \frac{e^{-\sqrt{\lambda^2+\beta^2}(x-x'_j-n\xi)}}{4\pi\sqrt{\lambda^2+\beta^2}} e^{i\lambda(y-y'_j-n\eta)} \frac{e^{-4\sqrt{\lambda^2+\beta^2}d}}{1-e^{-\sqrt{\lambda^2+\beta^2}d}} d\lambda, \\ K_2^{east}(\mathbf{t}, \mathbf{s}_j) &= \sum_{n=-1}^{1} \int_{-\infty}^{\infty} \frac{e^{\sqrt{\lambda^2+\beta^2}(x-x'_j-n\xi)}}{4\pi\sqrt{\lambda^2+\beta^2}} e^{i\lambda(y-y'_j-n\eta)} \frac{e^{-4\sqrt{\lambda^2+\beta^2}d}}{1-e^{-\sqrt{\lambda^2+\beta^2}d}} d\lambda. \end{aligned} \tag{4.15}$$

Proof. These formulas follow directly from Equation (3.7) and Equation (4.1) and summation of the geometric series in m. In the singly periodic case, excluding one nearest neighbor from either side is sufficient to ensure the exponential decay of the integrand in Equation (4.14). In the doubly periodic case, with a parallelogram as the unit cell, we must ensure that we are using the integral representation of the modified Bessel function where it is valid and that the resulting integrand decays exponentially fast. For this, we must have that $x - x' - md - n\xi > d$ for all $m \leq -(m_0+1)$ and $|n| \leq 1$ in the "west" case, and $x - x' + md - n\xi > d$ for all $m \geq m_0 + 1$ and $|n| \leq 1$ in the "east" case. It is straightforward to verify that if $m_0 = 3$, then $x - x' - md - n\xi \geq 4d - (d+\xi) - \xi > d$ in the first instance and that $x - x' + md - n\xi > d$ in the second instance under the stated assumption about the unit cell. □

There is a major difference between the east/west representations and those for the north and south. The latter are fully discrete, while for the east and west representations, we have an integral that needs to be evaluated before we can develop a low-rank decomposition. For this, we will make use of numerical quadrature, in order to develop a low-rank approximation of precision ϵ. This provides a discrete approximation of the Sommerfeld representation for $K_1^{west}(\mathbf{t}, \mathbf{s}_j)$ and $K_2^{west}(\mathbf{t}, \mathbf{s}_j)$ in Equation (4.14) and Equation (4.15) rewritten in the form

$$
\begin{aligned}
K_1^{west}(\mathbf{t}, \mathbf{s}_j) &= \Re\left(\int_0^\infty \frac{e^{-\sqrt{\lambda^2+\beta^2}(x-x_j')}}{2\pi\sqrt{\lambda^2+\beta^2}}\, e^{i\lambda(y-y_j')} \frac{e^{-2\sqrt{\lambda^2+\beta^2}d}}{1-e^{-\sqrt{\lambda^2+\beta^2}d}} d\lambda \right) \\
&\approx \Re\left(\sum_{n=1}^{N_q^1(\beta,d,\eta)} w_{n,1}(\beta,d,\eta) \frac{e^{-\sqrt{\lambda_{n,1}^2+\beta^2}(x-x_j')}}{2\pi\sqrt{\lambda_{n,1}^2+\beta^2}}\, e^{i\lambda_{n,1}(y-y_j')} \frac{e^{-2\sqrt{\lambda_{n,1}^2+\beta^2}d}}{1-e^{-\sqrt{\lambda_{n,1}^2+\beta^2}d}} \right). \\
K_2^{west}(\mathbf{t}, \mathbf{s}_j) &= \Re\Bigg(\int_0^\infty \frac{e^{-\sqrt{\lambda^2+\beta^2}(x-x_j')}}{2\pi\sqrt{\lambda^2+\beta^2}}\, e^{i\lambda(y-y_j')} \frac{e^{-4\sqrt{\lambda^2+\beta^2}d}}{1-e^{-\sqrt{\lambda^2+\beta^2}d}} \\
&\qquad\qquad \left[e^{-\sqrt{\lambda^2+\beta^2}\xi+i\lambda\eta} + e^{\sqrt{\lambda^2+\beta^2}\xi-i\lambda\eta} + 1\right] d\lambda \Bigg) \\
&\approx \Re\Bigg(\sum_{n=1}^{N_q^2(\beta,d,\eta)} w_{n,2}(\beta,d,\eta) \frac{e^{-\sqrt{\lambda_{n,2}^2+\beta^2}(x-x_j')}}{2\pi\sqrt{\lambda_{n,2}^2+\beta^2}}\, e^{i\lambda_{n,2}(y-y_j')} \frac{e^{-4\sqrt{\lambda_{n,2}^2+\beta^2}d}}{1-e^{-\sqrt{\lambda_{n,2}^2+\beta^2}d}} \\
&\qquad\qquad \left[e^{-\sqrt{\lambda_{n,2}^2+\beta^2}\xi+i\lambda_{n,2}\eta} + e^{\sqrt{\lambda_{n,2}^2+\beta^2}\xi-i\lambda_{n,2}\eta} + 1\right] \Bigg).
\end{aligned}
\tag{4.16}
$$

Note that different numbers of nodes may be needed for the two cases. We denote by N_q^1 and N_q^2 the number of nodes needed for K_1^{west} and K_2^{west}, respectively, with weights and nodes $\{w_{n,1}, \lambda_{n,1}\}$ and $\{w_{n,2}, \lambda_{n,2}\}$.

In both cases, we define $\lambda' = \lambda/d$ so that the decaying exponential in the integrand decays at least as fast as $e^{-\sqrt{\lambda'^2+\tilde{\beta}^2}}$ ($\tilde{\beta} = \beta \cdot d$). In the doubly periodic case, this leads to the consideration of the integrals in Section 2.2 where $(x, y) \in [1, 7] \times [-2, 2]$. Generalized Gaussian quadrature can be applied to construct numerical quadratures for a given precision ϵ, with a weak dependence on β. These quadratures are valid for unit cells with arbitrary geometric parameters and thus can be precomputed and stored (Bremer et al., 2010a; Ma et al., 1996;

Yarvin and Rokhlin, 1998).

In the singly periodic case, x lies in $[1, 3]$, while the range of y can be very large when $\eta \gg d$, leading to highly oscillatory integrals. In this case, the quadrature is constructed as follows. First, the interval $[0, \infty)$ is truncated to $[0, L]$, which can be accomplished easily due to the exponential decay in the x variable, with $L = \sqrt{(\log(1/\epsilon))^2 - \beta^2}$. If $\log(1/\epsilon) \leq \beta$, we can set $L = 0$, since the whole integral is then negligible. Second, in order to accurately capture the oscillatory behavior in the y variable, the interval $[0, L]$ is further divided into subintervals $[j\lambda_0, (j+1)\lambda_0]$ for $j = 0, \ldots, \lceil L/\lambda_0 \rceil$, where $\lambda_0 = 2\pi d/\eta$. A shifted and scaled n point Gauss-Legendre quadrature rule (with $n = O(\log(1/\epsilon))$) is then applied to discretize the integral on each subinterval $[j\lambda_0, (j+1)\lambda_0]$ for $j \geq 1$. Third, when β is very small, a new difficulty emerges - namely that the integrand is nearly singular at the origin. In that case, we further divide $[0, \lambda_0]$ into dyadic subintervals $[0, a]$ and $[2^{k-1}a, 2^k a]$ for $k = 1, \ldots, l_{\max}$, where $l_{\max} = \lceil \log_2(\lambda_0/\beta) \rceil$ and $a = \lambda_0/l_{\max}$. A shifted and scaled n point Gauss-Legendre quadrature rule is again applied to discretize the integral on each such subinterval. To summarize, the total number of quadrature nodes N_q^1 (i.e., the numerical rank of the periodizing operator) is $O\left(\log(1/\epsilon)\left(\log(1/\beta) + \log(1/\epsilon) \cdot \lceil \frac{\eta}{d} \rceil\right)\right)$. In the limit $\beta \to 0$, it is also possible to develop asymptotic expansions in β, which we do not consider here.

Remark 6. The difference between the singly and doubly periodic cases seems rather significant in terms of quadrature design. However, this distinction is somewhat artificial. The reason that the quadrature problem is simple in the doubly periodic case is that we have the freedom to choose which lattice vector is oriented along the x-axis. The difficult direction to deal with is the *short* axis of the unit cell and, by our convention, this makes the north/south periodizing kernels more oscillatory which are already discrete. Thus, the number of terms in the plane-wave expansion for the north/south parts will grow linearly with respect to the aspect ratio $\frac{d}{\eta}$ but without the need for quadrature design.

To summarize, the numerical rank of the periodizing operators may grow lin-

early with respect to the aspect ratio for both singly and doubly periodic problems. When the rank r is large, the NUFFT can be used to reduce the computational cost from $O(r(N_T + N_S))$ to $O(\log(1/\epsilon)(r \log r + (N_T + N_S)\log(1/\epsilon)))$ with ϵ the prescribed precision.

Theorem 4.3. *Let* $\mathbf{S} = \{\mathbf{s}_j \,|\, j = 1, \ldots, N_S\}$ *and* $\mathbf{T} = \{\mathbf{t}_l \,|\, l = 1, \ldots, N_T\}$ *denote collections of sources and targets in the unit cell* $\mathcal{C}$ *and let* $\mathbf{P}_1^{west}, \mathbf{P}_2^{west}$ *denote the* $N_T \times N_S$ *operators with* $\mathbf{P}_1^{west}(l,j) = K_1^{west}(\mathbf{t}_l, \mathbf{s}_j)$ *and* $\mathbf{P}_2^{west}(l,j) = K_2^{west}(\mathbf{t}_l, \mathbf{s}_j)$. *Given a precision* ϵ, *let* $N_q^1(\beta, d, \eta), N_q^2(\beta, d, \eta)$ *denote the number of points needed in the numerical quadrature for* $K_1^{west}(\mathbf{t}, \mathbf{s})$ *and* $K_2^{west}(\mathbf{t}, \mathbf{s})$, *with weights and nodes* $\{w_{n,1}, \lambda_{n,1}\}$ $\{w_{n,2}, \lambda_{n,2}\}$, *respectively. Let* $\mathbf{L}_1^{west} \in \mathbb{C}^{N_T \times N_q^1}$, $\mathbf{L}_2^{west} \in \mathbb{C}^{N_T \times N_q^2}$, $\mathbf{R}_1^{west} \in \mathbb{C}^{N_q^1 \times N_S}$, $\mathbf{R}_2^{west} \in \mathbb{C}^{N_q^2 \times N_S}$ *be dense matrices and let* $\mathbf{D}_1^{e/w}$, $\mathbf{D}_2^{west}$ *be diagonal matrices of dimension* N_q^1 *and* N_q^2, *respectively, with*

$$
\begin{aligned}
\mathbf{L}_1^{west}(l,n) &= e^{-\sqrt{\lambda_{n,1}^2+\beta^2}x_l} e^{i\lambda_{n,1}y_l}\,, \\
\mathbf{L}_2^{west}(l,n) &= e^{-\sqrt{\lambda_{n,2}^2+\beta^2}x_l} e^{i\lambda_{n,2}y_l}\,, \\
\mathbf{R}_1^{west}(n,j) &= e^{\sqrt{\lambda_{n,1}^2+\beta^2}x'_j}\, e^{-i\lambda_{n,1}y'_j}\,, \\
\mathbf{R}_2^{west}(n,j) &= e^{\sqrt{\lambda_{n,2}^2+\beta^2}x'_j}\, e^{-i\lambda_{n,2}y'_j}\,, \\
\mathbf{D}_1^{e/w}(n,n) &= \frac{1}{2\pi} \frac{w_{n,1}}{\sqrt{\lambda_{n,1}^2+\beta^2}} \frac{e^{-2\sqrt{\lambda_{n,1}^2+\beta^2}d}}{1 - e^{-\sqrt{\lambda_{n,1}^2+\beta^2}d}}\,, \\
\mathbf{D}_2^{west}(n,n) &= \frac{w_{n,2}}{\sqrt{\lambda_{n,2}^2+\beta^2}} \frac{e^{-4\sqrt{\lambda_{n,2}^2+\beta^2}d}}{1 - e^{-\sqrt{\lambda_{n,2}^2+\beta^2}d}} \frac{[e^{-\sqrt{\lambda_{n,2}^2+\beta^2}\xi + i\lambda_{n,2}\eta} + e^{\sqrt{\lambda_{n,2}^2+\beta^2}\xi - i\lambda_{n,2}\eta} + 1]}{2\pi}.
\end{aligned}
\tag{4.17}
$$

Let

$$
\begin{aligned}
\mathbf{P}_1^{west} &= \mathbf{L}_1^{west}\, \mathbf{D}_1^{e/w}\, \mathbf{R}_1^{west}, \\
\mathbf{P}_2^{west} &= \mathbf{L}_2^{west}\, \mathbf{D}_2^{west}\, \mathbf{R}_2^{west}.
\end{aligned}
$$

Then the real parts of the vectors

$$
\mathbf{P}_1^{west}\mathbf{q},\ \mathbf{P}_2^{west}\mathbf{q}
$$

denote the contributions from the west sources to the corresponding periodizing

potentials.

Corollary 2. *The matrices* $\mathbf{P}_1^{east}$ *and* $\mathbf{P}_2^{east}$ *have the low-rank factorizations*

$$\begin{aligned}\mathbf{P}_1^{east} &= \mathbf{L}_1^{east}\,\mathbf{D}_1^{e/w}\,\mathbf{R}_1^{east} + O(\epsilon)\\ \mathbf{P}_2^{east} &= \mathbf{L}_2^{east}\,\mathbf{D}_2^{east}\,\mathbf{R}_2^{east} + O(\epsilon)\end{aligned}$$

where $\mathbf{D}_2^{east} = \overline{\mathbf{D}_2^{west}}$,

$$\begin{aligned}\mathbf{L}_1^{east}(l,n) &= e^{\sqrt{\lambda_{n,1}^2+\beta^2}x_l}e^{i\lambda_{n,1}y_l}\,,\\ \mathbf{L}_2^{east}(l,n) &= e^{\sqrt{\lambda_{n,2}^2+\beta^2}x_l}e^{i\lambda_{n,2}y_l}\,,\\ \mathbf{R}_1^{east}(n,j) &= e^{-\sqrt{\lambda_{n,1}^2+\beta^2}x'_j}\,e^{-i\lambda_{n,1}y'_j}\,,\\ \mathbf{R}_2^{east}(n,j) &= e^{-\sqrt{\lambda_{n,2}^2+\beta^2}x'_j}\,e^{-i\lambda_{n,2}y'_j}\,.\end{aligned} \tag{4.18}$$

CHAPTER 5

PERIODIZING OPERATOR FOR THE LAPLACE KERNEL

In this chapter, we derive formulas for $\mathbf{P}_1^{west}$, $\mathbf{P}_1^{east}$, $\mathbf{P}_2^{west}$, $\mathbf{P}_2^{east}$, $\mathbf{P}_2^{south}$ and $\mathbf{P}_2^{north}$ in the limit $\beta \to 0$, allowing us to impose periodic boundary conditions for the Poisson equation using the same formalism

$$\begin{aligned} \mathbf{P}_1 &= \mathbf{P}_1^{west} + \mathbf{P}_1^{east}, \\ \mathbf{P}_2 &= \mathbf{P}_2^{west} + \mathbf{P}_2^{east} + \mathbf{P}_2^{south} + \mathbf{P}_2^{north}. \end{aligned} \tag{5.1}$$

As noted earlier, we require charge neutrality for the periodic problem to be well-posed. Moreover, as is well-known, the potential is only unique up to an arbitrary constant.

Theorem 5.1. *Let* $\mathbf{S} = \{\mathbf{s}_j \,|\, j = 1, \ldots, N_S\}$, $\mathbf{q} = (q_1, \ldots, q_{N_S})$, *and* $\mathbf{T} = \{\mathbf{t}_l \,|\, l = 1, \ldots, N_T\}$ *denote collections of source locations, charge strengths and targets in the unit cell* $\mathcal{C}$ *with* $\sum_{j=1}^{N_S} q_j = 0$. *Given a precision* ϵ, *let*

$$M = \left\lceil \frac{d}{2\pi\eta} \log\left(\frac{1}{1 - e^{-\frac{2\pi\eta}{d}}} \frac{1}{\epsilon} \right) \right\rceil \approx \frac{A}{2\pi} (\log(A) + \log(1/\epsilon)). \tag{5.2}$$

For $m = -M \ldots, M$, *let*

$$\alpha_m = \frac{2\pi m}{d}, \quad Q_m = \alpha_m \eta - i\alpha_m \xi \,. \tag{5.3}$$

Let $\mathbf{L}^{south} \in \mathbb{C}^{N_T \times (2M+1)}$ *and* $\mathbf{R}^{south} \in \mathbb{C}^{(2M+1)\times N_S}$ *be dense matrices and let* $\mathbf{D}^{south} \in \mathbb{C}^{(2M+1)\times(2M+1)}$ *be a diagonal matrix with*

$$\begin{aligned}
L^{south}(l,m) &= e^{-|\alpha_m| y_l} e^{i\alpha_m x_l} \quad \text{for } m \neq 0, \\
L^{south}(l,0) &= y_l, \\
\mathbf{R}^{south}(m,j) &= e^{|\alpha_m| y'_j}\, e^{-i\alpha_m x'_j} \quad \text{for } m \neq 0, \\
\mathbf{R}^{south}(0,j) &= y'_j, \\
\mathbf{D}^{south}(m,m) &= \frac{1}{4\pi|m|} \frac{e^{-2Q_m}}{1-e^{-Q_m}} \quad \text{for } m \neq 0 \\
\mathbf{D}^{south}(0,0) &= -\frac{1}{2d\eta}.
\end{aligned} \tag{5.4}$$

Then

$$\mathbf{P}_2^{south} = \mathbf{L}^{south}\, \mathbf{D}^{south}\, \mathbf{R}^{south} + O(\epsilon).$$

Proof. For all modes $m \neq 0$, this result follows directly from taking the limit $\beta \to 0$ in the corresponding term for the modified Helmholtz equation. For $m = 0$, the relevant contribution to $K_2^{south}(\mathbf{t}, \mathbf{s}_j)$ in (4.9) is

$$\frac{1}{2d}\frac{1}{\beta}\frac{e^{-2\beta\eta}}{1-e^{-\beta\eta}} e^{-\beta(y-y'_j)}.$$

Letting u_{south} denote the field due to all sources in the "south" image cells and summing over all sources yields

$$u_{south}(\mathbf{t}) = \frac{1}{2d}\frac{1}{\beta}\sum_{j=1}^{N_S} \frac{e^{-2\beta\eta}}{1-e^{-\beta\eta}} e^{-\beta(y-y'_j)} q_j. \tag{5.5}$$

Differentiating both sides of Equation 5.5 with respect to y, we have

$$\frac{\partial u_{south}(x,y)}{\partial y} = -\frac{1}{2d}\frac{e^{-2\beta\eta}}{1-e^{-\beta\eta}} \sum_{j=1}^{N_S} e^{-\beta(y-y'_j)} q_j. \tag{5.6}$$

Taylor expansion of the various terms yields:

$$\frac{\partial u_{south}(x,y)}{\partial y} = -\frac{1}{2d}\,\frac{1-O(\beta)}{\beta\eta+O(\beta^2)}\,e^{-\beta y}\,\left[\sum_{j=1}^{N_S} q_j + \beta\sum_{j=1}^{N_S} q_j y_j'\right]$$

Taking the limit $\beta \to 0$ and using charge neutrality as Equation 3.8, we obtain

$$\lim_{\beta\to 0}\frac{\partial u_{south}(x,y)}{\partial y} = -\frac{1}{2d\eta}\sum_{j=1}^{N_S} y_j q_j. \tag{5.7}$$

Hence, $u_{south}(x,y)$ is given by

$$\lim_{\beta\to 0} u_{south}(x,y) = -\frac{1}{2d\eta}\left(\sum_{j=1}^{N_S} y_j q_j\right) y \tag{5.8}$$

up to an arbitrary constant, completing the derivation. □

Then we can verify the following corollary.

Corollary 3. *Under the hypotheses of Theorem 5.1, let* $\mathbf{L}^{north} \in \mathbb{C}^{N_T\times(2M+1)}$ *and* $\mathbf{R}^{north} \in \mathbb{C}^{(2M+1)\times N_S}$ *be dense matrices with*

$$\begin{aligned}
\mathbf{L}^{north}(l,m) &= e^{|\alpha_m| y_l} e^{i\alpha_m x_l} \quad \text{for } m \neq 0,\\
\mathbf{L}^{north}(l,0) &= y_l,\\
\mathbf{R}^{north}(m,j) &= e^{-|\alpha_m| y_j'}\, e^{-i\alpha_m x_j'} \quad \text{for } m \neq 0,\\
\mathbf{R}^{north}(0,j) &= y_j'.
\end{aligned} \tag{5.9}$$

Then

$$\mathbf{P}_2^{north} = \mathbf{L}^{north}\,\mathbf{D}^{north}\,\mathbf{R}^{north} + O(\epsilon),$$

where $\mathbf{D}^{north} = \overline{\mathbf{D}^{south}}$.

We can take care this similar issue in the steps of deriving the east and the west formulas in the limit of $\beta \to 0$.

Theorem 5.2. *Let* $\mathbf{S} = \{\mathbf{s}_j \,|\, j = 1,\ldots,N_S\}$, $\mathbf{q} = (q_1,\ldots,q_{N_S})$, *and* $\mathbf{T} = \{\mathbf{t}_l \,|\, l = 1,\ldots,N_T\}$ *denote collections of source locations, charge strengths, and targets in*

the unit cell $\mathcal{C}$*, with* $\sum_{j=1}^{N_S} q_j = 0$*. Given a precision* ϵ*, let* $N_q^1(d,\eta), N_q^2(d,\eta)$ *denote the number of points needed in the numerical quadrature for the* K_1^{west} *and* K_2^{west} *kernels (see 5.11 and 5.12 below), with weights and nodes* $\{w_{n,1}, \lambda_{n,1}\}$ $\{w_{n,2}, \lambda_{n,2}\}$*, respectively. Let* $\mathbf{L}_1^{west}, \mathbf{L}_1^{east} \in \mathbb{C}^{N_T \times N_q^1}$*,* $\mathbf{L}_2^{west}, \mathbf{L}_2^{east} \in \mathbb{C}^{N_T \times N_q^2}$*,* $\mathbf{R}_1^{west}, \mathbf{R}_1^{east} \in \mathbb{C}^{N_q^1 \times N_S}$*,* $\mathbf{R}_2^{west}, \mathbf{R}_2^{east} \in \mathbb{C}^{N_q^2 \times N_S}$ *be dense matrices and let* $\mathbf{D}_1^{e/w}$*,* $\mathbf{D}_2^{west}$ *and* $\mathbf{D}_2^{east}$ *be diagonal matrices of dimension* N_q^1 *and* N_q^2*, respectively, with*

$$
\begin{aligned}
\mathbf{L}_1^{west}(l,n) &= e^{-\lambda_{n,1}x_l} e^{i\lambda_{n,1}y_l}\,,\ \mathbf{L}_2^{west}(l,n) = e^{-\lambda_{n,2}x_l} e^{i\lambda_{n,2}y_l}\,,\\
\mathbf{L}_1^{east}(l,n) &= e^{\lambda_{n,1}x_l} e^{i\lambda_{n,1}y_l}\,,\ \mathbf{L}_2^{east}(l,n) = e^{\lambda_{n,2}x_l} e^{i\lambda_{n,2}y_l}\,,\\
\mathbf{R}_1^{west}(n,j) &= e^{\lambda_{n,1}x'_j}\, e^{-i\lambda_{n,1}y'_j}\,,\ \mathbf{R}_2^{west}(n,j) = e^{\lambda_{n,2}x'_j}\, e^{-i\lambda_{n,2}y'_j}\,,\\
\mathbf{R}_1^{east}(n,j) &= e^{-\lambda_{n,1}x'_j}\, e^{-i\lambda_{n,1}y'_j}\,,\ \mathbf{R}_2^{east}(n,j) = e^{-\lambda_{n,2}x'_j}\, e^{-i\lambda_{n,2}y'_j}\,,\\
\mathbf{D}_1^{e/w}(n,n) &= \frac{1}{2\pi}\frac{w_{n,1}}{\lambda_{n,1}}\frac{e^{-2\lambda_{n,1}d}}{1-e^{-\lambda_{n,1}d}}\,,\\
\mathbf{D}_2^{west}(n,n) &= \frac{1}{2\pi}\frac{w_{n,2}}{\lambda_{n,2}}\frac{e^{-4\lambda_{n,2}d}}{1-e^{-\lambda_{n,2}d}}[e^{-\lambda_{n,2}\xi+i\lambda_{n,2}\eta} + e^{\lambda_{n,2}\xi-i\lambda_{n,2}\eta} + 1],
\end{aligned}
\tag{5.10}
$$

and $\mathbf{D}_2^{east} = \overline{\mathbf{D}_2^{west}}$*. Let*

$$
\begin{aligned}
\mathbf{P}_1^{west} &= \mathbf{L}_1^{west}\,\mathbf{D}_1^{e/w}\,\mathbf{R}_1^{west},\\
\mathbf{P}_2^{west} &= \mathbf{L}_2^{west}\,\mathbf{D}_2^{west}\,\mathbf{R}_2^{west}.\\
\mathbf{P}_1^{east} &= \mathbf{L}_1^{east}\,\mathbf{D}_1^{e/w}\,\mathbf{R}_1^{east},\\
\mathbf{P}_2^{east} &= \mathbf{L}_2^{east}\,\mathbf{D}_2^{east}\,\mathbf{R}_2^{east}.
\end{aligned}
$$

Then the real parts of the vectors

$$
\mathbf{P}_1^{west}\mathbf{q},\ \mathbf{P}_1^{east}\mathbf{q},\ P_2^{west}\mathbf{q}, \mathbf{P}_2^{east}\mathbf{q}
$$

denote the contributions from the west or east sources to the corresponding periodizing potentials.

Proof. Focusing on the "west" sources, the formulas themselves follow directly from the modified Helmholtz case, letting $\beta \to 0$ in Equation 4.16 and applying generalized Gaussian quadrature. As noted in section 2.2, however, the quadrature

rule is now being used to evaluate an integral of the apparent form

$$\int_0^\infty \frac{e^{-\lambda x}e^{i\lambda y}}{\lambda} M_1(\lambda) \frac{e^{-2\lambda d}}{1-e^{-\lambda d}} d\lambda \tag{5.11}$$

for the singly periodic case or

$$\int_0^\infty \frac{e^{-\lambda x}e^{i\lambda y}}{\lambda} M_1(\lambda) \frac{e^{-4\lambda d}}{1-e^{-\lambda d}} [e^{-\lambda\xi+i\lambda\eta} + e^{\lambda\xi-i\lambda\eta} + 1] d\lambda \tag{5.12}$$

for the doubly periodic case. Since $\frac{e^{-2\lambda d}}{1-e^{-\lambda d}}$ and $\frac{e^{-4\lambda d}}{1-e^{-\lambda d}}$ are both of the order $O(\frac{1}{\lambda})$ as $\lambda \to 0$, the integrals appear to be strongly singular, with a $\frac{1}{\lambda^2}$ singularity at the origin. However, in applying the periodizing operator, we limit ourselves to charge neutral distributions, so that we have

$$M_1(\lambda) = \sum_{j=1}^{N_S} q_j e^{\lambda(x_j - iy_j)} = O(\lambda).$$

Moreover, in computing any physical quantity, such as the gradient of the potential, a second factor of λ is introduced in the numerator and thus, the generalized Gaussian quadrature rule is only being applied to integrals of the form

$$\int_0^\infty e^{-\lambda x}e^{i\lambda y} M_2(\lambda)\, d\lambda,$$

where $M_2(\lambda)$ is smooth. The analysis for the "east" sources is identical. □

CHAPTER 6

PERIODIZING OPERATOR FOR THE MODIFIED STOKES EQUATIONS

The modified Stokeslet is the fundamental solution to the modified Stokes equations

$$\begin{aligned}(\beta^2 - \Delta)\mathbf{u} + \nabla p &= 0 \\ \nabla \cdot \mathbf{u} &= 0\end{aligned} \tag{6.1}$$

and is given at $\mathbf{t} = (x, y)$ by

$$\mathbf{G}^{(\mathrm{MS})}(\mathbf{t}) = (\nabla \otimes \nabla - \Delta \mathbf{I}) G_{\mathrm{MB}}(\mathbf{t}) = \begin{pmatrix} -\partial_{yy} & \partial_{xy} \\ \partial_{xy} & -\partial_{xx} \end{pmatrix} G_{\mathrm{MB}}(\mathbf{t}) \tag{6.2}$$

where

$$G_{\mathrm{MB}}(\mathbf{t}) = -\frac{1}{2\pi\beta^2} \left[K_0(\beta|\mathbf{t}|) - \log(1/|\mathbf{t}|) \right]. \tag{6.3}$$

This is the fundamental solution for the modified biharmonic equation:

$$\Delta(\Delta - \beta^2) G_{\mathrm{MB}}(\mathbf{t}) = \delta(\mathbf{t}). \tag{6.4}$$

Taking the Fourier transform of both sides yields the representation

$$G_{\mathrm{MB}}(\mathbf{t}) = \frac{1}{4\pi^2} \int_{-\infty}^{\infty} \int_{-\infty}^{\infty} \frac{1}{(k_1^2 + k_2^2)(\beta^2 + k_1^2 + k_2^2)} e^{i(k_1 x + k_2 y)} dk_1 dk_2. \tag{6.5}$$

Substituting Equation (6.5) into Equation (6.2), we obtain the Fourier representation of the modified Stokeslet:

$$\mathbf{G}_{ij}^{(\mathrm{MS})}(\mathbf{t}) = \frac{1}{4\pi^2} \int_{-\infty}^{\infty} \int_{-\infty}^{\infty} \frac{(k_1^2 + k_2^2)\delta_{ij} - k_i k_j}{(k_1^2 + k_2^2)(\beta^2 + k_1^2 + k_2^2)} e^{i(k_1 x + k_2 y)} dk_1 dk_2. \tag{6.6}$$

We now extend Sommerfeld's method to derive a plane-wave expansion for the modified Stokeslet (valid for $x > 0$) by contour integration in the k_1 variable and the residue theorem. Note that in the complex k_1-plane, the integrand has four

poles: namely $\pm i\sqrt{\beta^2+k_2^2}$ and $\pm i|k_2|$. Under the assumption: $x>0$, consider the closed contour from $-R$ to R along the real k_1 axis and returning along a semicircle of radius R in the upper half of the complex plane, the integral along the semicircle vanishes as $R\to\infty$, since

$$|e^{ik_1x}|\le 1\,,\quad \frac{1}{\beta^2+R^2e^{2i\theta}+k_2^2}\to 0\quad \text{as } R\to\infty$$

and the remaining terms in the integrand are bounded by 2. From the Residue Theorem, it follows that the integral is due to the residues at the two poles $i\sqrt{\beta^2+k_2^2}$ and $i|k_2|$ that lie within the contour, leading to:

$$\begin{aligned}\mathbf{G}^{(\mathrm{MS})}(\mathbf{t}) &= \frac{1}{4\pi\beta^2}\int_{-\infty}^{\infty}\frac{e^{-\sqrt{\beta^2+\lambda^2}x}}{\sqrt{\beta^2+\lambda^2}}e^{i\lambda y}\begin{bmatrix}-\lambda^2 & i\lambda\sqrt{\beta^2+\lambda^2}\\ i\lambda\sqrt{\beta^2+\lambda^2} & \beta^2+\lambda^2\end{bmatrix}d\lambda\\ &+\frac{1}{4\pi\beta^2}\int_{-\infty}^{\infty}e^{-|\lambda|x+i\lambda y}\begin{bmatrix}|\lambda| & -i\lambda\\ -i\lambda & -|\lambda|\end{bmatrix}d\lambda,\qquad x>0.\end{aligned}\tag{6.7}$$

The plane-wave expansions for $x<0, y>0$, and $y<0$ are obtained similarly. Here, we have renamed the k_2 Fourier variable as λ to be consistent with our earlier notation.

6.1 Low Rank Factorization

The periodizing operators $\mathbf{P}_1$ and $\mathbf{P}_2$ can be constructed by the same method as for the modified Helmholtz equation:

$$\begin{aligned}\mathbf{P}_1 &= \mathbf{P}_1^{west}+\mathbf{P}_1^{east},\\ \mathbf{P}_2 &= \mathbf{P}_2^{west}+\mathbf{P}_2^{east}+\mathbf{P}_2^{south}+\mathbf{P}_2^{north}.\end{aligned}\tag{6.8}$$

For a source to the "south", we have

$$\begin{aligned}\mathbf{K}_2^{south}(\mathbf{t},\mathbf{s}_j) &= \sum_{n=-\infty}^{-2}\sum_{m=-\infty}^{\infty}\mathbf{G}^{(\mathrm{MS})}(\mathbf{t}-(\mathbf{s}+\mathbf{l}_{mn}))\\ &= \frac{1}{4\pi\beta^2}\sum_{n=-\infty}^{-2}\sum_{m=-\infty}^{\infty}\left\{\int_{-\infty}^{\infty}\frac{e^{-\sqrt{\beta^2+\lambda^2}(y-y_j'-n\eta)}}{\sqrt{\beta^2+\lambda^2}}e^{i\lambda(x-x_j'-md-n\xi)}\right.\\ &\qquad\cdot\begin{bmatrix}\beta^2+\lambda^2 & i\lambda\sqrt{\beta^2+\lambda^2}\\ i\lambda\sqrt{\beta^2+\lambda^2} & -\lambda^2\end{bmatrix}d\lambda\\ &\quad\left.+\int_{-\infty}^{\infty}e^{-|\lambda|(y-y_j'-n\eta)+i\lambda(x-x_j'-md-n\xi)}\begin{bmatrix}-|\lambda| & -i\lambda\\ -i\lambda & |\lambda|\end{bmatrix}d\lambda\right\}.\end{aligned}\tag{6.9}$$

Following the same procedure used for the modified Helmholtz equation above, we obtain

$$\begin{aligned}\mathbf{K}_2^{south}(\mathbf{t},\mathbf{s}_j) = \frac{1}{2d\beta^2}\sum_{m=-\infty}^{\infty}\left(\begin{bmatrix}\chi_m & i\alpha_m\\ i\alpha_m & -\frac{\alpha_m^2}{\chi_m}\end{bmatrix}\frac{e^{-2Q_m^{(\beta)}}}{1-e^{-Q_m^{(\beta)}}}e^{-\chi_m(y-y_j')+i\alpha_m(x-x_j')}\right.\\ \left.+\begin{bmatrix}-|\alpha_m| & -i\alpha_m\\ -i\alpha_m & |\alpha_m|\end{bmatrix}\frac{e^{-2Q_m}}{1-e^{-Q_m}}e^{-|\alpha_m|(y-y_j')+i\alpha_m(x-x_j')}\right),\end{aligned}\tag{6.10}$$

where

$$Q_m^{(\beta)} = \chi_m\eta - i\alpha_m\xi, \quad Q_m = |\alpha_m|\eta - i\alpha_m\xi, \tag{6.11}$$

with α_m, χ_m given in Equation (4.5).

This establishes

Theorem 6.1. *Let* $\mathbf{S} = \{\mathbf{s}_j \,|\, j = 1,\ldots,N_S\}$ *and* $\mathbf{T} = \{\mathbf{t}_l \,|\, l = 1,\ldots,N_T\}$ *denote collections of sources and targets in the unit cell* $\mathcal{C}$ *and let* $\mathbf{P}_2^{south}$ *denote the* $N_T\times N_S$ *block matrix with* $\mathbf{P}_2^{south}(l,j) = \mathbf{K}_2^{south}(\mathbf{t}_l,\mathbf{s}_j)$. *Given a precision* ϵ, *let* M *be given by Equation* (4.4). *For* $m = -M\ldots,M$, *let* $Q_m^{(\beta)}, Q_m$ *be given by Equation* (6.11) *and let* α_m, χ_m *be given by Equation* (4.5). *Let* $\mathbf{L}_\beta^{south}, \mathbf{L}^{south}, \mathbf{L}_\beta^{north}, \mathbf{L}^{north} \in \mathbb{C}^{2N_T\times 2(2M+1)}$ *and* $\mathbf{R}_\beta^{south}, \mathbf{R}^{south}, \mathbf{R}_\beta^{north}, \mathbf{R}^{north} \in \mathbb{C}^{2(2M+1)\times 2N_S}$ *be dense* $N_T \times (2M+1)$ *and* $(2M+1)\times N_S$ *block matrices, respectively, with* 2×2 *blocks,*

let $\mathbf{D}_\beta^{south}, \mathbf{D}^{south}, \mathbf{D}_\beta^{north}, \mathbf{D}^{north} \in \mathbb{C}^{2(2M+1)\times 2(2M+1)}$ *be* $(2M+1)\times(2M+1)$ *block diagonal matrices with* 2×2 *diagonal blocks, let* $\mathbf{I}_2$ *denote the identity matrix of size 2, and let*

$$
\begin{aligned}
\mathbf{L}_\beta^{south}(l,m) &= e^{-\chi_m y_l} e^{i\alpha_m x_l}\mathbf{I}_2, \quad \mathbf{L}_\beta^{north}(l,m) = e^{\chi_m y_l} e^{i\alpha_m x_l}\mathbf{I}_2\,,\\
\mathbf{L}^{south}(l,m) &= e^{-|\alpha_m| y_l} e^{i\alpha_m x_l}\mathbf{I}_2, \quad \mathbf{L}^{north}(l,m) = e^{|\alpha_m| y_l} e^{i\alpha_m x_l}\mathbf{I}_2\,,\\
\mathbf{R}_\beta^{south}(m,j) &= e^{\chi_m y'_j} e^{-i\alpha_m x'_j}\mathbf{I}_2, \quad \mathbf{R}_\beta^{north}(m,j) = e^{-\chi_m y'_j} e^{-i\alpha_m x'_j}\mathbf{I}_2\,,\\
\mathbf{R}^{south}(m,j) &= e^{|\alpha_m| y'_j} e^{-i\alpha_m x'_j}\mathbf{I}_2, \quad \mathbf{R}^{north}(m,j) = e^{-|\alpha_m| y'_j} e^{-i\alpha_m x'_j}\mathbf{I}_2\,,\\
\mathbf{D}_\beta^{south}(m,m) &= \frac{1}{2\beta^2 d}\frac{e^{-2Q_m^{(\beta)}}}{1-e^{-Q_m^{(\beta)}}}\begin{pmatrix}\chi_m & i\alpha_m\\ i\alpha_m & -\alpha_m^2/\chi_m\end{pmatrix}, \quad \mathbf{D}_\beta^{north}(m,m) = \overline{\mathbf{D}_\beta^{south}(m,m)}\,,\\
\mathbf{D}^{south}(m,m) &= \frac{1}{2\beta^2 d}\frac{e^{-2Q_m}}{1-e^{-Q_m}}\begin{pmatrix}-|\alpha_m| & -i\alpha_m\\ -i\alpha_m & |\alpha_m|\end{pmatrix}, \quad \mathbf{D}^{north}(m,m) = \overline{\mathbf{D}^{south}(m,m)}\,.
\end{aligned}
\tag{6.12}
$$

Then

$$
\begin{aligned}
\mathbf{P}_2^{south} &= \mathbf{L}_\beta^{south}\,\mathbf{D}_\beta^{south}\,\mathbf{R}_\beta^{south} + \mathbf{L}^{south}\,\mathbf{D}^{south}\,\mathbf{R}^{south} + O(\epsilon),\\
\mathbf{P}_2^{north} &= \mathbf{L}_\beta^{north}\,\mathbf{D}_\beta^{north}\,\mathbf{R}_\beta^{north} + \mathbf{L}^{north}\,\mathbf{D}^{north}\,\mathbf{R}^{north} + O(\epsilon).
\end{aligned}
$$

For the sources in image boxes to the "west", we have

$$
\begin{aligned}
\mathbf{K}_1^{west}(\mathbf{t},\mathbf{s}_j) &= \sum_{m=-\infty}^{-2} \mathbf{G}^{(\mathrm{MS})}\left(\mathbf{t}-(\mathbf{s}_j+\mathbf{l}_{m0})\right) \\
&= \frac{1}{4\pi\beta^2}\left\{\int_{-\infty}^{\infty} e^{-\sqrt{\beta^2+\lambda^2}(x-x_j')}e^{i\lambda(y-y_j')}\right. \\
&\qquad\qquad \cdot \begin{bmatrix} -\frac{\lambda^2}{\sqrt{\beta^2+\lambda^2}} & i\lambda \\ i\lambda & \sqrt{\beta^2+\lambda^2} \end{bmatrix} \frac{e^{-2\sqrt{\beta^2+\lambda^2}d}}{1-e^{-\sqrt{\beta^2+\lambda^2}d}}d\lambda \\
&\qquad\qquad + \int_{-\infty}^{\infty} e^{-|\lambda|(x-x_j')+i\lambda(y-y_j')} \\
&\qquad\qquad \left. \cdot \begin{bmatrix} |\lambda| & -i\lambda \\ -i\lambda & -|\lambda| \end{bmatrix} \frac{e^{-2|\lambda|d}}{1-e^{-|\lambda|d}}d\lambda \right\}, \\
\mathbf{K}_2^{west}(\mathbf{t},\mathbf{s}_j) &= \sum_{m=-\infty}^{-4}\sum_{n=-1}^{1} \mathbf{G}^{(\mathrm{MS})}\left(\mathbf{t}-(\mathbf{s}_j+\mathbf{l}_{mn})\right) \\
&= \frac{1}{4\pi\beta^2}\sum_{n=-1}^{1}\left\{\int_{-\infty}^{\infty} e^{-\sqrt{\beta^2+\lambda^2}(x-x_j'-n\xi)}e^{i\lambda(y-y_j'-n\eta)}\right. \\
&\qquad\qquad \cdot \begin{bmatrix} -\frac{\lambda^2}{\sqrt{\beta^2+\lambda^2}} & i\lambda \\ i\lambda & \sqrt{\beta^2+\lambda^2} \end{bmatrix} \frac{e^{-4\sqrt{\beta^2+\lambda^2}d}}{1-e^{-\sqrt{\beta^2+\lambda^2}d}}d\lambda \\
&\qquad\qquad + \int_{-\infty}^{\infty} e^{-|\lambda|(x-x_j'-n\xi)+i\lambda(y-y_j'-n\eta)} \\
&\qquad\qquad \left. \cdot \begin{bmatrix} |\lambda| & -i\lambda \\ -i\lambda & -|\lambda| \end{bmatrix} \frac{e^{-4|\lambda|d}}{1-e^{-|\lambda|d}}d\lambda \right\}.
\end{aligned}
\tag{6.13}
$$

Theorem 6.2. *Let* $\mathbf{S} = \{\mathbf{s}_j \,|\, j = 1,\ldots,N_S\}$ *and* $\mathbf{T} = \{\mathbf{t}_l \,|\, l = 1,\ldots,N_T\}$ *denote collections of sources and targets in the unit cell* $\mathcal{C}$ *and let* $\mathbf{P}_1^{west}, \mathbf{P}_2^{west}$ *denote the* $N_T \times N_S$ *block matrices with* 2×2 *blocks* $\mathbf{P}_1^{west}(l,j) = \mathbf{K}_1^{west}(\mathbf{t}_l,\mathbf{s}_j)$ *and* $\mathbf{P}_2^{west}(l,j) = K_2^{west}(\mathbf{t}_l,\mathbf{s}_j)$. *Given a precision* ϵ, *let* $N_q^1(\beta,d,\eta), N_q^1(0,d,\eta)$ *and* $N_q^2(\beta,d,\eta), N_q^2(0,d,\eta)$ *denote the number of points needed in the numerical quadratures for the two integrals in each of* $\mathbf{K}_1^{west}(\mathbf{t},\mathbf{s})$ *and* $\mathbf{K}_2^{west}(\mathbf{t},\mathbf{s})$, *with weights and nodes* $\{w_{n,\beta,1},\lambda_{n,\beta,1}\}$, $\{w_{n,0,1},\lambda_{n,0,1}\}$, $\{w_{n,\beta,2},\lambda_{n,\beta,2}\}$, *and* $\{w_{n,0,2},\lambda_{n,0,2}\}$, *respectively. Let* $\mathbf{L}_{1,\beta}^{west}$, $\mathbf{L}_1^{west}$, $\mathbf{L}_{2,\beta}^{west}$, $\mathbf{L}_2^{west}$, $\mathbf{R}_{1,\beta}^{west}$, $\mathbf{R}_1^{west}$, $\mathbf{R}_{2,\beta}^{west}$, $\mathbf{R}_2^{west}$ *be dense block*

matrices with 2×2 *blocks given by:*

$$\begin{aligned}
\mathbf{L}^{west}_{1,\beta}(l,n) &= e^{-\sqrt{\lambda^2_{n,\beta,1}+\beta^2}x_l} e^{i\lambda_{n,\beta,1}y_l}\mathbf{I}_2 \,| \quad l=1,\dots,N_T,\ n=1,\dots,N^1_q(\beta,d,\eta)\\
\mathbf{L}^{west}_{1}(l,n) &= e^{-|\lambda_{n,0,1}|x_l} e^{i\lambda_{n,0,1}y_l}\mathbf{I}_2 \quad\ | \quad l=1,\dots,N_T,\ n=1,\dots,N^1_q(0,d,\eta)\\
\mathbf{L}^{west}_{2,\beta}(l,n) &= e^{-\sqrt{\lambda^2_{n,\beta,2}+\beta^2}x_l} e^{i\lambda_{n,\beta,2}y_l}\mathbf{I}_2 \,| \quad l=1,\dots,N_T,\ n=1,\dots,N^2_q(\beta,d,\eta)\\
\mathbf{L}^{west}_{2}(l,n) &= e^{-|\lambda_{n,0,2}|x_l} e^{i\lambda_{n,0,2}y_l}\mathbf{I}_2 \quad\ | \quad l=1,\dots,N_T,\ n=1,\dots,N^2_q(0,d,\eta)\\
\mathbf{R}^{west}_{1,\beta}(n,j) &= e^{\sqrt{\lambda^2_{n,\beta,1}+\beta^2}x'_j} e^{-i\lambda_{n,\beta,1}y'_j}\mathbf{I}_2 \,| \quad n=1,\dots,N^1_q(\beta,d,\eta),\ j=1,\dots,N_S\\
\mathbf{R}^{west}_{1}(n,j) &= e^{|\lambda_{n,0,1}|x'_j} e^{-i\lambda_{n,0,1}y'_j}\mathbf{I}_2 \quad\ | \quad n=1,\dots,N^1_q(0,d,\eta),\ j=1,\dots,N_S\\
\mathbf{R}^{west}_{2,\beta}(n,j) &= e^{\sqrt{\lambda^2_{n,\beta,2}+\beta^2}x'_j} e^{-i\lambda_{n,\beta,2}y'_j}\mathbf{I}_2 \,| \quad n=1,\dots,N^2_q(\beta,d,\eta),\ j=1,\dots,N_S\\
\mathbf{R}^{west}_{2}(n,j) &= e^{|\lambda_{n,0,2}|x'_j} e^{i\lambda_{n,0,2}y'_j}\mathbf{I}_2 \quad\ | \quad n=1,\dots,N^2_q(0,d,\eta),\ j=1,\dots,N_S\,,
\end{aligned} \tag{6.14}$$

and let $\mathbf{D}^{west}_{1,\beta}$, $\mathbf{D}^{west}_{1}$, $\mathbf{D}^{west}_{2,\beta}$, $\mathbf{D}^{west}_{2}$ *be block diagonal matrices with* 2×2 *blocks*

given by:

$$\mathbf{D}^{west}_{1,\beta}(n,n) = \frac{w_{n,\beta,1}}{4\pi\beta^2}\frac{e^{-2\sqrt{\lambda^2_{n,\beta,1}+\beta^2}d}}{1-e^{-\sqrt{\lambda^2_{n,\beta,1}+\beta^2}d}}\begin{bmatrix} -\frac{\lambda^2_{n,1}}{\sqrt{\beta^2+\lambda^2_{n,\beta,1}}} & i\lambda_{n,\beta,1} \\ i\lambda_{n,\beta,1} & \sqrt{\beta^2+\lambda^2_{n,\beta,1}}\end{bmatrix},$$

$$n = 1,\ldots,N^1_q(\beta,d,\eta)$$

$$\mathbf{D}^{west}_{1}(n,n) = \frac{w_{n,0,1}}{4\pi\beta^2}\frac{e^{-2|\lambda_{n,0,1}|d}}{1-e^{-|\lambda_{n,0,1}|d}}\begin{bmatrix} |\lambda_{n,0,1}| & -i\lambda_{n,0,1} \\ -i\lambda_{n,0,1} & -|\lambda_{n,0,1}|\end{bmatrix},$$

$$n = 1,\ldots,N^1_q(0,d,\eta)$$

$$\mathbf{D}^{west}_{2,\beta}(n,n) = \frac{w_{n,\beta,2}}{4\pi\beta^2}[e^{-\sqrt{\beta^2+\lambda_{n,\beta,2}}\xi+i\lambda_{n,\beta,2}\eta}+e^{\lambda_{n,\beta,2}\xi-i\lambda_{n,\beta,2}\eta}+1]\cdot$$
$$\frac{e^{-4\sqrt{\lambda^2_{n,\beta,2}+\beta^2}d}}{1-e^{-\sqrt{\lambda^2_{n,\beta,2}+\beta^2}d}}\begin{bmatrix} -\frac{\lambda^2_{n,\beta,2}}{\sqrt{\beta^2+\lambda^2_{n,\beta,2}}} & i\lambda_{n,\beta,2} \\ i\lambda_{n,\beta,2} & \sqrt{\beta^2+\lambda^2_{n,\beta,2}}\end{bmatrix},$$

$$n = 1,\ldots,N^2_q(\beta,d,\eta)$$

$$\mathbf{D}^{west}_{2}(n,n) = \frac{w_{n,0,2}}{4\pi\beta^2}[e^{-|\lambda_{n,0,2}|\xi+i\lambda_{n,0,2}\eta}+e^{|\lambda_{n,0.2}|\xi-i\lambda_{n,0.2}\eta}+1]\cdot$$
$$\frac{e^{-4|\lambda_{n,0,2}|d}}{1-e^{-|\lambda_{n,0,2}|d}}\begin{bmatrix} |\lambda_{n,0,1}| & -i\lambda_{n,0,1} \\ -i\lambda_{n,0,1} & -|\lambda_{n,0,1}|\end{bmatrix}, \quad n = 1,\ldots,N^2_q(0,d,\eta). \tag{6.15}$$

Let

$$\mathbf{P}^{west}_1 = \mathbf{L}^{west}_{1,\beta}\,\mathbf{D}^{west}_{1,\beta}\,\mathbf{R}^{west}_{1,\beta} + \mathbf{L}^{west}_{1}\,\mathbf{D}^{west}_{1}\,\mathbf{R}^{west}_{1},$$
$$\mathbf{P}^{west}_2 = \mathbf{L}^{west}_{2,\beta}\,\mathbf{D}^{west}_{2,\beta}\,\mathbf{R}^{west}_{2,\beta} + \mathbf{L}^{west}_{2}\,\mathbf{D}^{west}_{2}\,\mathbf{R}^{west}_{2}.$$

Then the real parts of the vectors

$$\mathbf{P}^{west}_1\mathbf{q},\ \mathbf{P}^{west}_2\mathbf{q}$$

denote the contributions from the west sources to the corresponding periodizing potentials. The formulas for $\mathbf{P}^{east}_1$ *and* $\mathbf{P}^{east}_2$ *are identical, except that* $x_l \leftrightarrow -x_l$ *and* $x'_j \leftrightarrow -x'_j$ *in the various* $\mathbf{L}(l,n)$ *and* $\mathbf{R}(n,j)$ *blocks above and that* $\mathbf{D}^{east}_{1,\beta} = \overline{\mathbf{D}^{west}_{1,\beta}}$, $\mathbf{D}^{east}_{1} = \overline{\mathbf{D}^{west}_{1}}$, $\mathbf{D}^{east}_{2,\beta} = \overline{\mathbf{D}^{west}_{2,\beta}}$, $\mathbf{D}^{east}_{2} = \overline{\mathbf{D}^{west}_{2}}$.

CHAPTER 7

PERIODIZING OPERATOR FOR THE STOKES EQUATIONS

While the Stokeslet, i.e., the Green's function for the incompressible Stokes flow, is given by the formula

$$\mathbf{G}^{(\mathrm{S})}(\mathbf{t}) = -\frac{1}{4\pi}\left(\log|\mathbf{t}|\,\mathbf{I} - \frac{\mathbf{t}\otimes\mathbf{t}}{|\mathbf{t}|^2}\right), \tag{7.1}$$

a systematic way of computing the correct limit for the periodizing operators is to let $\beta \to 0$ in the various formulas for the modified Stokes equations, invoking charge neutrality before taking the limit.

Theorem 7.1. *Let* $\mathbf{S} = \{\mathbf{s}_j \,|\, j = 1, \ldots, N_S\}$ *and* $\mathbf{T} = \{\mathbf{t}_l \,|\, l = 1, \ldots, N_T\}$ *denote collections of sources and targets in the unit cell* $\mathcal{C}$ *and let* $\mathbf{P}_2^{south}$ *denote the* $N_T \times N_S$ *block matrix which is the periodizing operator for all "south" sources. Given a precision* ϵ*, let* M *be given by Equation 4.4. With* α_m, Q_m *given in Equation 4.5 and Equation 6.11, let* $\mathbf{L}^{south}$ *and* $\mathbf{R}^{south}$ *be defined as in Equation 6.12 except with*

$$\begin{aligned} \mathbf{L}^{south}(l,0) &= \begin{pmatrix} y_l & 0 \\ 0 & y_l \end{pmatrix} \\ \mathbf{R}^{south}(0,j) &= \begin{pmatrix} y_j' & 0 \\ 0 & y_j' \end{pmatrix}. \end{aligned} \tag{7.2}$$

Let $\mathbf{D}_a^{south}, \mathbf{D}_b^{south} \in \mathbb{C}^{2(2M+1)\times 2(2M+1)}$ *be* $(2M+1)\times(2M+1)$ *block diagonal matrices with* 2×2 *diagonal blocks, and let* $\mathbf{D}_S \in \mathbb{C}^{2N_S\times 2N_S}$, $\mathbf{D}_T \in \mathbb{C}^{2N_T\times 2N_T}$ *be*

block diagonal matrices with 2×2 *diagonal blocks given by*

$$\begin{aligned}
&\mathbf{D}_a^{south}(m,m) \\
&\qquad = \frac{1}{4d}\frac{e^{-2Q_m}}{1-e^{-Q_m}} \left(\frac{1}{|\alpha_m|} \begin{pmatrix} 1 & 0 \\ 0 & 1 \end{pmatrix} - \frac{2-e^{-Q_m}}{1-e^{-Q_m}}\eta \begin{pmatrix} 1 & i\,\mathrm{sign}(m) \\ i\,\mathrm{sign}(m) & -1 \end{pmatrix} \right) \\
&\text{for } m \neq 0 \\
&\mathbf{D}_b^{south}(m,m) = \frac{1}{4d}\frac{e^{-2Q_m}}{1-e^{-Q_m}} \begin{pmatrix} 1 & i\,\mathrm{sign}(m) \\ i\,\mathrm{sign}(m) & -1 \end{pmatrix} \quad \text{for } m \neq 0 \\
&\mathbf{D}_a^{south}(0,0) = -\frac{1}{2d\eta} \begin{pmatrix} 1 & 0 \\ 0 & 0 \end{pmatrix} \\
&\mathbf{D}_b^{south}(0,0) = \begin{pmatrix} 0 & 0 \\ 0 & 0 \end{pmatrix} \\
&\qquad \mathbf{D}_S(j,j) = \begin{pmatrix} y'_j & 0 \\ 0 & y'_j \end{pmatrix} \\
&\qquad \mathbf{D}_T(i,i) = \begin{pmatrix} y_i & 0 \\ 0 & y_i \end{pmatrix} .
\end{aligned} \tag{7.3}$$

Then

$$\mathbf{P}_2^{south} = \mathbf{L}^{south}\,\mathbf{D}_a^{south}\,\mathbf{R}^{south} - \mathbf{D}_T\,\mathbf{L}^{south}\,\mathbf{D}_b^{south}\,\mathbf{R}^{south} + \mathbf{L}^{south}\,\mathbf{D}_b^{south}\,\mathbf{R}^{south}\,\mathbf{D}_S + O(\epsilon)\,.$$

Proof. Consider first one of the terms in Equation 6.10 corresponding to a mode $m \neq 0$. We will denote the limit as $\beta \to 0$ by $\mathbf{K}_2^{south}[m]$. Using L'Hopital's rule,

and taking the limit $\beta \to 0$, it is straightforward to see that

$$\begin{aligned}
\mathbf{K}_2^{south}[m](\mathbf{t}, \mathbf{s}_j) = \lim_{\beta \to 0} \frac{1}{2d\beta^2} \Bigg(& \begin{bmatrix} \chi_m & i\alpha_m \\ i\alpha_m & -\frac{\alpha_m^2}{\chi_m} \end{bmatrix} \frac{e^{-2Q_m^{(\beta)}}}{1 - e^{-Q_m^{(\beta)}}} e^{-\chi_m (y - y_j') + i\alpha_m (x - x_j')} \\
& + \begin{bmatrix} -|\alpha_m| & -i\alpha_m \\ -i\alpha_m & |\alpha_m| \end{bmatrix} \frac{e^{-2Q_m}}{1 - e^{-Q_m}} e^{-|\alpha_m|(y - y_j') + i\alpha_m (x - x_j')} \Bigg) \\
= \frac{1}{4d} & \left\{ \frac{1}{|\alpha_m|} \begin{bmatrix} 1 & 0 \\ 0 & 1 \end{bmatrix} - \left(y - y_0 + \frac{2 - e^{-Q_m}}{1 - e^{-Q_m}} \eta \right) \begin{bmatrix} 1 & i\,\mathrm{sign}(m) \\ i\,\mathrm{sign}(m) & -1 \end{bmatrix} \right\} \\
& \cdot \frac{e^{-2Q_m}}{1 - e^{-Q_m}} e^{-|\alpha_m|(y - y_j') + i\alpha_m (x - x_j')}.
\end{aligned} \tag{7.4}$$

It is easy to check that every column of $\mathbf{K}_2^{south}[m]$ is divergence-free and that every entry of $\mathbf{K}_2^{south}[m]$ is biharmonic.

For the $m = 0$ term, we have

$$\mathbf{K}_2^{south}[0](\mathbf{t}, \mathbf{s}_j) = \lim_{\beta \to 0} \frac{1}{2d\beta^2} \begin{bmatrix} \beta & 0 \\ 0 & 0 \end{bmatrix} \frac{e^{-2\beta\eta}}{1 - e^{-\beta\eta}} e^{-\beta(y - y_j')}. \tag{7.5}$$

As we did for the Poisson equation, using charge neutrality and expanding the exponential terms in a Taylor series, we obtain

$$\mathbf{K}_2^{south}[0](\mathbf{t}, \mathbf{s}_j) = -\frac{1}{2d\eta} \begin{bmatrix} yy_j' & 0 \\ 0 & 0 \end{bmatrix}. \tag{7.6}$$

Combining Equation 7.4 and Equation 7.6, we obtain

$$\begin{aligned}\mathbf{K}_2^{south}(\mathbf{t},\mathbf{s}_j) &= \sum_{m=-\infty}^{\infty} \mathbf{K}_2^{south}[m](\mathbf{t},\mathbf{s}_j) \\ &= -\frac{1}{2d\eta}\begin{bmatrix} yy'_j & 0 \\ 0 & 0 \end{bmatrix} + \frac{1}{4d}\sum_{\substack{m=-\infty \\ m\neq 0}}^{\infty}\Bigg\{\frac{1}{|\alpha_m|}\begin{bmatrix} 1 & 0 \\ 0 & 1 \end{bmatrix} \\ &\quad - \left(y - y'_j + \frac{2-e^{-Q_m}}{1-e^{-Q_m}}\eta\right)\begin{bmatrix} 1 & i\,\mathrm{sign}(m) \\ i\,\mathrm{sign}(m) & -1 \end{bmatrix}\Bigg\} \\ &\quad \cdot \frac{e^{-2Q_m}}{1-e^{-Q_m}} e^{-|\alpha_m|(y-y'_j)+i\alpha_m(x-x'_j)}.\end{aligned} \tag{7.7}$$

□

Remark 7. In an almost identical manner, we can show that

$$\begin{aligned}\mathbf{K}_2^{north}(\mathbf{t},\mathbf{s}_j) &= -\frac{1}{2d\eta}\begin{bmatrix} yy'_j & 0 \\ 0 & 0 \end{bmatrix} + \frac{1}{4d}\sum_{\substack{m=-\infty \\ m\neq 0}}^{\infty}\Bigg\{\frac{1}{|\alpha_m|}\begin{bmatrix} 1 & 0 \\ 0 & 1 \end{bmatrix} \\ &\quad - \left(y - y'_j - \frac{2-e^{-\overline{Q_m}}}{1-e^{-\overline{Q_m}}}\eta\right)\begin{bmatrix} -1 & i\,\mathrm{sign}(m) \\ i\,\mathrm{sign}(m) & 1 \end{bmatrix}\Bigg\} \\ &\quad \cdot \frac{e^{-2\overline{Q_m}}}{1-e^{-\overline{Q_m}}} e^{|\alpha_m|(y-y'_j)+i\alpha_m(x-x'_j)}.\end{aligned} \tag{7.8}$$

And the expression for $\mathbf{P}_2^{north}$ can be derived similarly.

Taking the limit $\beta \to 0$ for Equation 6.13 and using charge neutrality, we

likewise obtain the west part of the periodizing operator for the Stokeslet:

$$\begin{aligned}
\mathbf{K}_1^{west}(\mathbf{t},\mathbf{s}) &= \frac{1}{8\pi}\int_{-\infty}^{\infty} \frac{e^{-2|\lambda|d}}{1-e^{-|\lambda|d}} e^{-|\lambda|(x-x')} e^{i\lambda(y-y')} \cdot \left\{ \frac{1}{|\lambda|} \begin{bmatrix} 1 & 0 \\ 0 & 1 \end{bmatrix} \right. \\
&\quad \left. - \left(x - x' + \frac{2-e^{-|\lambda|d}}{1-e^{-|\lambda|d}} d \right) \begin{bmatrix} -1 & i\,\mathrm{sign}(\lambda) \\ i\,\mathrm{sign}(\lambda) & 1 \end{bmatrix} \right\} d\lambda, \\
\mathbf{K}_2^{west}(\mathbf{t},\mathbf{s}) &= \frac{1}{8\pi}\sum_{n=-1}^{1}\int_{-\infty}^{\infty} \frac{e^{-4|\lambda|d}}{1-e^{-|\lambda|d}} e^{-|\lambda|(x-x'-n\xi)} e^{i\lambda(y-y'-n\eta)} \cdot \left\{ \frac{1}{|\lambda|} \begin{bmatrix} 1 & 0 \\ 0 & 1 \end{bmatrix} \right. \\
&\quad \left. - \left(x - x' - n\xi + \frac{4-3e^{-|\lambda|d}}{1-e^{-|\lambda|d}} d \right) \begin{bmatrix} -1 & i\,\mathrm{sign}(\lambda) \\ i\,\mathrm{sign}(\lambda) & 1 \end{bmatrix} \right\} d\lambda,
\end{aligned} \tag{7.9}$$

It is again easy to check that every column of $\mathbf{K}_1^{west}$ or $\mathbf{K}_2^{west}$ is divergence-free and that every entry is biharmonic. The above representation yields the following theorem.

Theorem 7.2. *Let* $\mathbf{S} = \{\mathbf{s}_j \,|\, j = 1,\ldots,N_S\}$ *and* $\mathbf{T} = \{\mathbf{t}_l \,|\, l = 1,\ldots,N_T\}$ *denote collections of sources and targets in the unit cell* $\mathcal{C}$ *and let* $\mathbf{P}_1^{west}, \mathbf{P}_2^{west}$ *denote the* $N_T \times N_S$ *block matrices with* 2×2 *blocks* $\mathbf{P}_1^{west}(l,j) = \mathbf{K}_1^{west}(\mathbf{t}_l,\mathbf{s}_j)$ *and* $\mathbf{P}_2^{west}(l,j) = K_2^{west}(\mathbf{t}_l,\mathbf{s}_j)$. *Given a precision* ϵ, *let* $N_q^1(d,\eta)$ *and* $N_q^2(d,\eta)$ *denote the number of points needed in the numerical quadratures for the integrals in* $\mathbf{K}_1^{west}(\mathbf{t},\mathbf{s})$ *and* $\mathbf{K}_2^{west}(\mathbf{t},\mathbf{s})$, *with weights and nodes* $\{w_{n,0,1},\lambda_{n,0,1}\}$, $\{w_{n,0,2},\lambda_{n,0,2}\}$, *respectively. Let* $\mathbf{L}_1^{west}$, $\mathbf{L}_2^{west}$, $\mathbf{R}_1^{west}$, $\mathbf{R}_2^{west}$ *be dense block matrices with* 2×2 *blocks given by Equation 6.14, and let* $\mathbf{D}_{1,a}^{west}$, $\mathbf{D}_{1,b}^{west}$, $\mathbf{D}_{2,a}^{west}$, $\mathbf{D}_{2,b}^{west}$ *be block diagonal*

matrices with 2×2 *blocks given by:*

$$\begin{aligned}
\mathbf{D}^{west}_{1,a}(n,n) &= \frac{w_{n,0,1}}{8\pi}\frac{e^{-2|\lambda_{n,0,1}|d}}{1-e^{-|\lambda_{n,0,1}|d}}\left(\begin{bmatrix} 1/|\lambda_{n,0,1}| & 0 \\ 0 & 1/|\lambda_{n,0,1}| \end{bmatrix}\right. \\
&\qquad\left. - \frac{2-e^{-|\lambda_{n,0,1}|d}}{1-e^{-|\lambda_{n,0,1}|d}}\, d \begin{bmatrix} -1 & i\,\mathrm{sign}(\lambda_{n,0,1}) \\ i\,\mathrm{sign}(\lambda_{n,0,1}) & 1 \end{bmatrix}\right), \\
\mathbf{D}^{west}_{1,b}(n,n) &= \frac{w_{n,0,1}}{8\pi}\frac{e^{-2|\lambda_{n,0,1}|d}}{1-e^{-|\lambda_{n,0,1}|d}} \begin{bmatrix} -1 & i\,\mathrm{sign}(\lambda_{n,0,1}) \\ i\,\mathrm{sign}(\lambda_{n,0,1}) & 1 \end{bmatrix}, \\
\mathbf{D}^{west}_{2,a}(n,n) &= \frac{w_{n,0,2}}{8\pi}\frac{e^{-4|\lambda_{n,0,2}|d}}{1-e^{-|\lambda_{n,0,2}|d}}\,[e^{-|\lambda_{n,0,2}|\xi+i\lambda_{n,0,2}\eta} + e^{|\lambda_{n,0,2}|\xi-i\lambda_{n,0,2}\eta} + 1]\times \\
&\qquad\left(\begin{bmatrix} 1/|\lambda_{n,0,2}| & 0 \\ 0 & 1/|\lambda_{n,0,2}| \end{bmatrix} - \frac{4-3e^{-|\lambda_{n,0,2}|d}}{1-e^{-|\lambda_{n,0,2}|d}}\, d \begin{bmatrix} -1 & i\,\mathrm{sign}(\lambda_{n,0,2}) \\ i\,\mathrm{sign}(\lambda_{n,0,2}) & 1 \end{bmatrix}\right. \\
&\qquad\left. - \left[e^{-|\lambda_{n,0,2}|\xi+i\lambda_{n,0,2}\eta} - e^{|\lambda_{n,0,2}|\xi-i\lambda_{n,0,2}\eta}\right]\xi \begin{bmatrix} -1 & i\,\mathrm{sign}(\lambda_{n,0,2}) \\ i\,\mathrm{sign}(\lambda_{n,0,2}) & 1 \end{bmatrix}\right) \\
\mathbf{D}^{west}_{2,b}(n,n) &= \frac{w_{n,0,2}}{8\pi}\frac{e^{-4|\lambda_{n,0,2}|d}}{1-e^{-|\lambda_{n,0,2}|d}}\,[e^{-|\lambda_{n,0,2}|\xi+i\lambda_{n,0,2}\eta} + e^{|\lambda_{n,0,2}|\xi-i\lambda_{n,0,2}\eta} + 1]\times \\
&\qquad \begin{bmatrix} -1 & i\,\mathrm{sign}(\lambda_{n,0,2}) \\ i\,\mathrm{sign}(\lambda_{n,0,2}) & 1 \end{bmatrix}.
\end{aligned} \tag{7.10}$$

Let

$$\begin{aligned}
\mathbf{P}^{west}_1 &= \mathbf{L}^{west}_1\,\mathbf{D}^{west}_{1,a}\,\mathbf{R}^{west}_1 - \mathbf{D}_T\mathbf{L}^{west}_1\mathbf{D}^{west}_{1,b}\,\mathbf{R}^{west}_1 + \mathbf{L}^{west}_1\mathbf{D}^{west}_{1,b}\,\mathbf{R}^{west}_1\,\mathbf{D}_S \\
\mathbf{P}^{west}_2 &= \mathbf{L}^{west}_2\,\mathbf{D}^{west}_{2,a}\,\mathbf{R}^{west}_2 - \mathbf{D}_T\mathbf{L}^{west}_2\mathbf{D}^{west}_{2,b}\,\mathbf{R}^{west}_2 + \mathbf{L}^{west}_2\mathbf{D}^{west}_{2,b}\,\mathbf{R}^{west}_2\,\mathbf{D}_S\,.
\end{aligned}$$

Then the real parts of the vectors

$$\mathbf{P}^{west}_1\mathbf{q},\ \mathbf{P}^{west}_2\mathbf{q}$$

denote the contributions from the west sources to the corresponding periodizing potentials.

Remark 8. In an almost identical manner, we can show that

$$\begin{aligned}
\mathbf{K}_1^{east}(\mathbf{t},\mathbf{s}) &= \frac{1}{8\pi}\int_{-\infty}^{\infty} \frac{e^{-2|\lambda|d}}{1-e^{-|\lambda|d}} e^{|\lambda|(x-x')} e^{i\lambda(y-y')} \cdot \left\{ \frac{1}{|\lambda|}\begin{bmatrix} 1 & 0 \\ 0 & 1 \end{bmatrix} \right. \\
&\quad \left. - \left(x - x' - \frac{2-e^{-|\lambda|d}}{1-e^{-|\lambda|d}} d \right) \begin{bmatrix} 1 & i\,\mathrm{sign}(\lambda) \\ i\,\mathrm{sign}(\lambda) & -1 \end{bmatrix} \right\} d\lambda, \\
\mathbf{K}_2^{east}(\mathbf{t},\mathbf{s}) &= \frac{1}{8\pi}\sum_{n=-1}^{1}\int_{-\infty}^{\infty} \frac{e^{-4|\lambda|d}}{1-e^{-|\lambda|d}} e^{|\lambda|(x-x'-n\xi)} e^{i\lambda(y-y'-n\eta)} \cdot \left\{ \frac{1}{|\lambda|}\begin{bmatrix} 1 & 0 \\ 0 & 1 \end{bmatrix} \right. \\
&\quad \left. - \left(x - x' - n\xi - \frac{4-3e^{-|\lambda|d}}{1-e^{-|\lambda|d}} d \right) \begin{bmatrix} 1 & i\,\mathrm{sign}(\lambda) \\ i\,\mathrm{sign}(\lambda) & -1 \end{bmatrix} \right\} d\lambda.
\end{aligned} \tag{7.11}$$

The expressions for $\mathbf{P}_1^{east}$, $\mathbf{P}_2^{east}$ can be derived similarly.

For both the modified Stokeslet and Stokeslet, the associated pressurelet is given by:

$$\mathbf{p}(\mathbf{t}) = \frac{1}{2\pi}\frac{\mathbf{t}}{|\mathbf{t}|^2} = \frac{1}{2\pi}\nabla \log|\mathbf{t}|. \tag{7.12}$$

Thus, the periodizing operators for the pressurelet can be obtained by simply differentiating those for the logarithmic kernel in Chapter 5, summarized in the following two theorems.

Theorem 7.3. *Let* $\mathbf{S} = \{\mathbf{s}_j \,|\, j = 1,\ldots,N_S\}$ *and* $\mathbf{T} = \{\mathbf{t}_l \,|\, l = 1,\ldots,N_T\}$ *denote collections of sources and targets in the unit cell* $\mathcal{C}$ *and let* $\mathbf{P}_2^{south}$ *denote the* $N_T \times N_S$ *block matrix which is the periodizing operator for all "south" sources for the pressure for both the modified Stokes and Stokes equations. Given a precision* ϵ*, let* M *be given by Equation 5.2. With* α_m, Q_m *given in Equation 5.3, let* $\mathbf{L}^{south}, \mathbf{L}^{north} \in \mathbb{C}^{N_T\times(2M+1)}$ *and* $\mathbf{R}^{south}, \mathbf{R}^{north} \in \mathbb{C}^{(2M+1)\times 2N_S}$ *be dense matrices and let*

$$\mathbf{D}^{south}, \mathbf{D}^{north} \in \mathbb{C}^{(2M+1)\times(2M+1)}$$

be diagonal matrices with

$$\begin{aligned}
\mathbf{L}^{south}(l,m) &= e^{-|\alpha_m|y_l} e^{i\alpha_m x_l}, \quad \text{for } m \neq 0,\\
\mathbf{L}^{north}(l,m) &= e^{|\alpha_m|y_l} e^{i\alpha_m x_l}, \quad \text{for } m \neq 0,\\
\mathbf{L}^{south}(l,0) &= y_l, \quad \mathbf{L}^{north}(l,0) = y_l,\\
\mathbf{R}^{south}(m,j) &= e^{|\alpha_m|y'_j}\, e^{-i\alpha_m x'_j}[i\alpha_m \ -|\alpha_m|] \quad \text{for } m \neq 0,\\
\mathbf{R}^{north}(m,j) &= e^{-|\alpha_m|y'_j}\, e^{-i\alpha_m x'_j}[i\alpha_m \ |\alpha_m|] \quad \text{for } m \neq 0,\\
\mathbf{R}^{south}(0,j) &= [0\ 1], \quad \mathbf{R}^{north}(0,j) = [0\ 1],\\
\mathbf{D}^{south}(m,m) &= -\frac{1}{4\pi|m|}\frac{e^{-2Q_m}}{1-e^{-Q_m}} \quad \text{for } m \neq 0\\
\mathbf{D}^{south}(0,0) &= \frac{1}{2d\eta}, \quad \mathbf{D}^{north} = \overline{\mathbf{D}^{south}}.
\end{aligned} \tag{7.13}$$

Then

$$\begin{aligned}
\mathbf{P}_2^{south} &= \mathbf{L}^{south}\,\mathbf{D}^{south}\,\mathbf{R}^{south} + O(\epsilon),\\
\mathbf{P}_2^{north} &= \mathbf{L}^{north}\,\mathbf{D}^{north}\,\mathbf{R}^{north} + O(\epsilon).
\end{aligned} \tag{7.14}$$

Theorem 7.4. *Under the hypotheses of Theorem 5.2, let* $\mathbf{L}_1^{west}, \mathbf{L}_1^{east} \in \mathbb{C}^{N_T \times N_q^1}$, $\mathbf{L}_2^{west}, \mathbf{L}_2^{east} \in \mathbb{C}^{N_T \times N_q^2}$, *be dense matrices and let* $\mathbf{D}_1^{e/w}$, $\mathbf{D}_2^{west}$ *and* $\mathbf{D}_2^{east}$ *be diagonal matrices of dimension* N_q^1 *and* N_q^2 *defined in Equation 5.10. Let* $\mathbf{R}_1^{west}, \mathbf{R}_1^{east} \in \mathbb{C}^{N_q^1 \times 2N_S}$, $\mathbf{R}_2^{west}, \mathbf{R}_2^{east} \in \mathbb{C}^{N_q^2 \times 2N_S}$ *be dense matrices with*

$$\begin{aligned}
\mathbf{R}_1^{west}(n,j) &= e^{\lambda_{n,1}x'_j}\, e^{-i\lambda_{n,1}y'_j}\, [\lambda_{n,1} \quad -i\lambda_{n,1}],\\
\mathbf{R}_2^{west}(n,j) &= e^{\lambda_{n,2}x'_j}\, e^{-i\lambda_{n,2}y'_j}\, [\lambda_{n,2} \quad -i\lambda_{n,2}],\\
\mathbf{R}_1^{east}(n,j) &= e^{-\lambda_{n,1}x'_j}\, e^{-i\lambda_{n,1}y'_j}\, [-\lambda_{n,1} \quad -i\lambda_{n,1}],\\
\mathbf{R}_2^{east}(n,j) &= e^{-\lambda_{n,2}x'_j}\, e^{-i\lambda_{n,2}y'_j}\, [-\lambda_{n,2} \quad -i\lambda_{n,2}].
\end{aligned} \tag{7.15}$$

Let

$$\begin{aligned}
\mathbf{P}_1^{west} &= \mathbf{L}_1^{west}\,\mathbf{D}_1^{e/w}\,\mathbf{R}_1^{west},\\
\mathbf{P}_2^{west} &= \mathbf{L}_2^{west}\,\mathbf{D}_2^{west}\,\mathbf{R}_2^{west}.\\
\mathbf{P}_1^{east} &= \mathbf{L}_1^{east}\,\mathbf{D}_1^{e/w}\,\mathbf{R}_1^{east},\\
\mathbf{P}_2^{east} &= \mathbf{L}_2^{east}\,\mathbf{D}_2^{east}\,\mathbf{R}_2^{east}.
\end{aligned}$$

Then the real parts of the vectors

$$\mathbf{P}_1^{west}\mathbf{q},\ \mathbf{P}_1^{east}\mathbf{q}, \mathbf{P}_2^{west}\mathbf{q}, \mathbf{P}_2^{east}\mathbf{q}$$

denote the contributions from the west or east sources to the corresponding periodizing pressures.

CHAPTER 8

Basic Algorithm and NUFFT Acceleration

In this chapter, we use the planewave representations derived in the previous chapters to define explicit algorithms for computing fast sums of the periodizing operators $\mathbf{P}^{Y,l}$ and $\mathbf{P}^{L,l}$ for a collection of N_s sources at N_t targets. The first subsection contains a basic algorithm with $O(r(N_s + N_t))$ computational complexity, where r is the rank of $\mathbf{P}^{Y,l}$ or $\mathbf{P}^{L,l}$. Because the rank r grows linearly in the aspect ratio $A = d/\eta$, an acceleration strategy is proposed in the second subsection. There, the NUFFT is used to achieve a computational complexity of the form $O((r + N_s + N_t)\log(r + N_s + N_t))$.

The central idea of both algorithms is to divide the evaluation of $\mathbf{P}^{Y,l}$ and $\mathbf{P}^{L,l}$ into two stages based on the separability of the planewave representations: a "form" stage in which the coefficients for approximating $\mathbf{P}^{Y,l}$ or $\mathbf{P}^{L,l}$ in the plane wave basis are computed and an "apply" stage in which the approximate operators are evaluated at any set of targets by evaluating the planewave expansions at those points. The accelerated algorithm takes advantage of NUFFT-like rank structures in the form and apply operators.

8.1 Basic Algorithm

Consider a collection of N_s sources with strengths q_j and locations $\mathbf{S}_j = (x_j, y_j) \in \mathcal{C}$. Let α_m and χ_m be defined as:

$$\alpha_m = \alpha_0 + \frac{2\pi m}{d}, \qquad \chi_m = \sqrt{\alpha_m^2 + \beta^2}, \tag{8.1}$$

and let M be the order of the planewave expansions for the north and south directions. Further, let

$$Q_m^{(Y)} = \chi_m \eta - i\left((\alpha_m - \alpha_0)\xi + \beta_0 \eta\right) \tag{8.2}$$

and

$$Q_m^{(L)} = \frac{2\pi m}{d}(\eta - i\xi). \tag{8.3}$$

The "form planewave" operators will be written as a matrix-vector multiplication of the form $\mathbf{Fq}$, where $\mathbf{q}$ is the vector of charge strengths. We define the Yukawa form planewave operator for the south direction by

$$\left[\mathbf{F}_s^{Y,l}(\{\mathbf{S}_j\}; M)\mathbf{q}\right]_m = \frac{i^\ell \pi}{\chi_m d}\left(\frac{\beta}{\chi_m + \alpha_m}\right)^\ell \frac{e^{-2Q_m^{(Y)}}}{1 - e^{-Q_m^{(Y)}}} \sum_{j=1}^{N_s} q_j e^{\chi_m y_j - i\alpha_m x_j} \ ,$$

$$\text{for } m = m_0 - M, \ldots, m_0 + M. \tag{8.4}$$

Similarly, we define the Laplace form planewave operator for the south direction by

$$\left[\mathbf{F}_s^{L,l}(\{\mathbf{S}_j\}; M)\mathbf{q}\right]_m = \frac{(-i)^\ell}{m(\ell-1)!}\left(\frac{2\pi m}{d}\right)^\ell \frac{e^{-2Q_m^{(L)}}}{1 - e^{-Q_m^{(L)}}} \sum_{j=1}^{N_s} q_j e^{2\pi m(y_j - ix_j)/d} \ ,$$

$$\text{for } m = 1, \ldots, M. \tag{8.5}$$

The corresponding form planewave operators for the north direction are defined analogously.

The form planewave operators for the west direction take a similar form but now involve the quadrature nodes and weights of the previous section. We define

$$\left[\mathbf{F}_w^{Y,l}(\{\mathbf{S}_j\})\mathbf{q}\right]_m = w_i^{(Y,l)}(\tilde{\beta}) \sum_{j=1}^{N_s} q_j e^{\frac{x_j\sqrt{\left(\lambda_m^{(Y,l)}\right)^2 + \tilde{\beta}^2}}{d}} e^{-i\frac{y_j \lambda_m^{(Y,l)}}{d}} \ ,$$

$$\text{for } m = 1, \ldots, N_q(\tilde{\beta})^{(Y,l)} \tag{8.6}$$

and

$$\left[\mathbf{F}_w^{L,l}(\{\mathbf{S}_j\})\mathbf{q}\right]_m = w_i^{(L,l)} \sum_{j=1}^{N_s} q_j e^{\frac{x_j\sqrt{\left(\lambda_m^{(L,l)}\right)^2+\tilde{\beta}^2}}{d}} e^{i\frac{y_j\lambda_m^{(L,l)}}{d}} ,$$

$$\text{for } m = 1, \ldots, N_q^{(L,l)} . \quad (8.7)$$

The form planewave operators for the east direction are defined analogously. Let $\mathbf{c}$ denote the coefficients returned by any of the form operators defined above. The apply operators evaluate the planewave expansions corresponding to these coefficients at a set of N_t target nodes, which we denote by $\mathbf{T}_i = (v_i, w_i) \in \mathcal{C}$. We define the apply operators for the south direction by

$$\left[\mathbf{A}_s^{Y,l}(\{\mathbf{T}_i\}; M)\mathbf{c}\right]_n = \sum_{m=m_0-M}^{m_0+M} c_m e^{i\alpha_m v_n - \chi_m w_n} , \text{ for } n = 1, \ldots, N_t , \quad (8.8)$$

and

$$\left[\mathbf{A}_s^{L,l}(\{\mathbf{T}_i\}; M)\mathbf{c}\right]_n = \sum_{m=1}^{M} c_m e^{2\pi m(iv_n - w_n)/d} , \text{ for } n = 1, \ldots, N_t . \quad (8.9)$$

The north direction is defined analogously. Similarly, we define the apply operators for the west direction by

$$\left[\mathbf{A}_w^{Y,l}(\{\mathbf{T}_i\}; \tilde{\beta})\mathbf{c}\right]_n = \sum_{m=1}^{N_q^{(Y,l)}(\tilde{\beta})} c_m e^{-\frac{v_n\sqrt{\left(\lambda_m^{(Y,l)}\right)^2+\tilde{\beta}^2}}{d}} e^{i\frac{w_n\lambda_m^{(Y,l)}}{d}} , \text{ for } n = 1, \ldots, N_t , \quad (8.10)$$

and

$$\left[\mathbf{A}_w^{Y,l}(\{\mathbf{T}_i\})\mathbf{c}\right]_n = \sum_{m=1}^{N_q^{(L,l)}} c_m e^{-\frac{v_n\lambda_m^{(L,l)}}{d}} e^{-i\frac{w_n\lambda_m^{(L,l)}}{d}} , \text{ for } n = 1, \ldots, N_t . \quad (8.11)$$

The apply operators for the east direction are defined analogously.

Once these operators are defined, the basic algorithm for evaluating the Yukawa periodizing operator can be stated succinctly; see Algorithm 1. The

cost of the algorithm is clearly $O(M(N_s + N_t) + N_q^{(Y,l)}(\tilde{\beta})(N_s + N_t))$. The M required to achieve a given accuracy, ϵ, grows linearly in the aspect ratio, i.e. $M = O(\log(1/\epsilon)d/\eta)$. The number of quadrature nodes required, $N_q^{(Y,l)}$, is comparable to the number of terms required in a fast multipole method, i.e. $N_q^{(Y,l)}(\tilde{\beta}) = O(\log(1/\epsilon))$, independent of the aspect ratio.

Algorithm 1 Basic algorithm for evaluating $u_i = \sum_{j=1}^{N_s} \mathbf{P}^{Y,l}(\mathbf{T}_i, \mathbf{S}_j)q_j$.

Input: $\{\mathbf{S}_j\}$, $\mathbf{q}$, $\{\mathbf{T}_i\}$, M.
1: $\mathbf{c}_s \leftarrow \mathbf{F}_s^{Y,l}(\{\mathbf{S}_j\}; M)\mathbf{q}$
2: $\mathbf{c}_n \leftarrow \mathbf{F}_n^{Y,l}(\{\mathbf{S}_j\}; M)\mathbf{q}$
3: $\mathbf{c}_w \leftarrow \mathbf{F}_w^{Y,l}(\{\mathbf{S}_j\})\mathbf{q}$
4: $\mathbf{c}_e \leftarrow \mathbf{F}_e^{Y,l}(\{\mathbf{S}_j\})\mathbf{q}$
5: $\mathbf{u} \leftarrow 0$
6: $\mathbf{u} \leftarrow \mathbf{u} + \mathbf{A}_s^{Y,l}(\{\mathbf{T}_i\}; M)\mathbf{c}_s$
7: $\mathbf{u} \leftarrow \mathbf{u} + \mathbf{A}_n^{Y,l}(\{\mathbf{T}_i\}; M)\mathbf{c}_n$
8: $\mathbf{u} \leftarrow \mathbf{u} + \mathbf{A}_w^{Y,l}(\{\mathbf{T}_i\})\mathbf{c}_w$
9: $\mathbf{u} \leftarrow \mathbf{u} + \mathbf{A}_e^{Y,l}(\{\mathbf{T}_i\})\mathbf{c}_e$
Output: $\mathbf{u}$.

8.2 NUFFT Acceleration

To efficiently compute the periodization operators for unit cells with moderate to high aspect ratios, we must accelerate the evaluation of the form and apply operators for the south and north directions.

8.2.1 Accelerated Form Operators

Consider the form south operator for Yukawa potentials, i.e., $\mathbf{F}_s^{Y,l}$. Suppose that we are interested in applying this operator for some set of sources $\mathbf{S}_j^{(0)}$ where the y-coordinate is fixed, i.e. $\mathbf{S}_j^{(0)} = (x_j^{(0)}, y^{(0)}) \in \mathcal{C}$. Setting

$$\begin{aligned} \nu_m^{(Y,l)}(y^{(0)}) &= \frac{i^\ell \pi}{\chi_m d}\left(\frac{\beta}{\chi_m + \alpha_m}\right)^\ell \frac{e^{-2Q_m^{(Y)}}}{1 - e^{-Q_m^{(Y)}}} e^{\chi_m y^{(0)}} \\ \sigma_j^{(Y,l)}(\{x_j^{(0)}\}) &= e^{-i(\alpha_0 + 2\pi m_0/d)x_j^{(0)}}, \end{aligned} \tag{8.12}$$

we have that

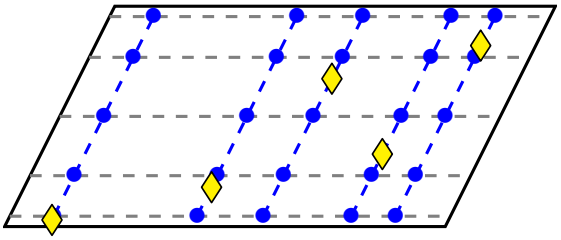

Figure 8.1 An illustration of the auxiliary grids used for the accelerated algorithm. Yellow diamonds represent source locations for the form stage or target locations for the apply stage. The blue dots are the auxiliary points used for anterpolation in the form stage or interpolation in the apply stage.

$$\left[\mathbf{F}_s^{Y,l}(\{\mathbf{S}_j^{(0)}\}; M)\mathbf{q}\right]_m = \nu_m^{(Y,l)}(y^{(0)}) \sum_{j=1}^{N_s} e^{-im'(2\pi x_j/d)} \sigma_j^{(Y,l)}(\{\mathbf{S}_j^{(0)}\}) q_j \ ,$$

$$\text{for } m = m_0 - M, \ldots, m_0 + M \ , \quad (8.13)$$

where $m' = m - m_0$. Thus, the form south operator can be written

$$\mathbf{F}_s^{Y,l}(\{\mathbf{S}_j^{(0)}\}; M) = \mathbf{D}_s^{(Y,l,1)}(y^{(0)}) \mathbf{N}^{(1)}(\{-2\pi x_j^{(0)}/d\}, M) \mathbf{D}_s^{(Y,l,2)}(\{x_j^{(0)}\}) \ , \quad (8.14)$$

where $\mathbf{D}_s^{(Y,l,1)}(y^{(0)})$ and $\mathbf{D}_s^{(Y,l,2)}(\{x_j^{(0)}\})$ are diagonal operators and $\mathbf{N}^{(1)}$ is the type-I NUFFT operator defined in Equation (2.4). The cost of applying $\mathbf{F}_s^{Y,l}$ for such a set of points is then $O((N_s+M)\log(N_s+M))$ using a standard NUFFT algorithm. To apply this acceleration to general sets of source points, $\{\mathbf{S}_j\}$, we use an anterpolation strategy. Observe that each component of $\mathbf{F}_s^{Y,l}$ is an entire function of the source point coordinates, x_j and y_j; the dependence of the m-th output on source location j takes the form

$$f(\mathbf{S}_j; q_j) = \gamma_m q_j e^{\chi_m y_j - i\alpha_m x_j} \ ,$$

where γ_m is a constant. We can thus interpolate this function to any source location by using its value for a small number of fixed y coordinates.

In particular, we define $y^{(i)} = \eta(t_i + 1)/2$, where $t_1 < \cdots < t_{M_{\text{leg}}}$ are the M_{leg}-th order Legendre nodes. To conform to the parallelogram shape of the unit cell, we interpolate this function along lines with slope η/ξ; see Figure 8.1 for an illustration. Defining $\bar{x}_j = x_j - \xi y_j/\eta$, we can then interpolate $f(\mathbf{S}_j; q_j)$ by using the values $f(\mathbf{S}_j^{(i)}; q_j)$ where $\mathbf{S}_j^{(i)} = (\bar{x}_j + \xi y^{(i)}/\eta, y^{(i)})$. Let $\lambda_1, \ldots, \lambda_{M_{\text{leg}}}$ be the barycentric interpolation weights defined in Equation (2.7). Then,

$$c^{(1)}(y_j) f(\mathbf{S}_j^{(1)}; q_j) + \cdots + c^{(M_{\text{leg}})}(y_j) f(\mathbf{S}_j^{(M_{\text{leg}})}; q_j)$$

is a spectrally accurate approximation of $f(\mathbf{S}_j; q_j)$, where

$$c^{(i)}(y_j) = \frac{\frac{\lambda_i}{y_j - y^{(i)}}}{\sum_{n=1}^{M_{\text{leg}}} \frac{\lambda_n}{y_j - y^{(n)}}} \,. \tag{8.15}$$

Interpolation of the operator in this way can be reinterpreted as defining a set of "equivalent sources" through anterpolation, i.e., the source at $\mathbf{S}_j$ with charge q_j is replaced by sources at $\mathbf{S}_j^{(1)}, \ldots, \mathbf{S}_j^{(M_{\text{leg}})}$ with charges $q_j c^{(1)}(y_j), \ldots, q_j c^{(M_{\text{leg}})}(y_j)$. Because each of the sets $\{\mathbf{S}_j^{(i)}\}$ has charges with a fixed y-coordinate, the NUFFT-accelerated approach described above can be applied. The resulting algorithm is provided in Algorithm 2 and has $O(M_{\text{leg}}(N_s + M)\log(N_s + M))$ computational complexity. The anterpolated sources provide a spectrally accurate approximation of the original sources. For non-oscillatory kernels like Yukawa and Laplace, we find that 25 Legendre nodes are sufficient for double precision accuracy.

Algorithm 2 Accelerated algorithm for evaluating $\mathbf{c}_s \approx \mathbf{F}_s^{Y,l}(\mathbf{S}_j; M)\mathbf{q}$.

Input: $\{\mathbf{S}_j\}$, $\mathbf{q}$, M, M_{leg}.

$t_1, \ldots, t_{M_{\text{leg}}} \leftarrow M_{\text{leg}}$-th order Legendre nodes
$\lambda_1, \ldots, \lambda_{M_{\text{leg}}} \leftarrow$ Barycentric weights
for $i = 1, \ldots, M_{\text{leg}}$ **do**
    $y^{(i)} \leftarrow y_j(t_i + 1)/2$
    for $j = 1, \ldots, N_s$ **do**
        $(x_j, y_j) \leftarrow \mathbf{S}_j$
        $\bar{x}_j \leftarrow x_j - \xi y_j/\eta$
        $x_j^{(i)} \leftarrow \bar{x}_j + \xi y^{(i)}/\eta$
        $q_j^{(i)} \leftarrow q_j c^{(i)}(y_j)$
$\mathbf{c}_s \leftarrow 0$
for $i = 1, \ldots, M_{\text{leg}}$ **do**
    $\tilde{\mathbf{q}} \leftarrow \mathbf{D}^{(Y,l,2)}(\{x_j^{(i)}\})\mathbf{q}^{(i)}$
    $\tilde{\mathbf{c}} \leftarrow \mathbf{N}^{(1)}\left(\left\{-2\pi x_j^{(i)}/d\right\}, M\right)\tilde{\mathbf{q}}$
    $\mathbf{c}_s \leftarrow \mathbf{c}_s + \mathbf{D}_s^{(Y,l,1)}(y^{(i)})\tilde{\mathbf{c}}$

Output: $\mathbf{c}_s$.

8.2.2 Accelerated Apply Operators

A similar strategy can be applied to the operator $\mathbf{A}_s^{Y,l}$. Suppose that some target points of interest, $\mathbf{T}_i^{(0)}$, all share the same y-coordinate, i.e. $\mathbf{T}_i^{(0)} = (v_i^{(0)}, w^{(0)}) \in \mathcal{C}$. Setting

$$\sigma_n^{(Y,l)}(\{v_j^{(0)}\}) = e^{i(\alpha_0 + 2\pi m_0/d)v_n^{(0)}} ,$$

we have that

$$\left[\mathbf{A}_s^{Y,l}(\{\mathbf{T}_j^{(0)}\}; M)\mathbf{c}\right]_n = \sigma_n^{(Y,l)} \sum_{m'=-M}^{M} e^{-\chi_{m'+m_0} w^{(0)}} c_{m'+m_0} e^{im'(2\pi v_n/d)} ,$$

$$\text{for } n = 1, \ldots, N_t . \quad (8.16)$$

Thus, the apply south operator can be written

$$\mathbf{A}_s^{Y,l}(\{\mathbf{T}_j^{(0)}\}; M) = \mathbf{D}_s^{(Y,l,3)}(\{v_j^{(0)}\})\mathbf{N}^{(2)}(\{2\pi v_j^{(0)}/d\}, M)\mathbf{D}^{(Y,l,4)}(w^{(0)}) , \quad (8.17)$$

where $\mathbf{D}_s^{(Y,l,3)}(\{v_j^{(0)}\})$ and $\mathbf{D}_s^{(Y,l,4)}(w^{(0)})$ are diagonal operators and $\mathbf{N}^{(2)}$ is the type-II NUFFT operator defined in Equation (2.5). The cost of applying $\mathbf{A}_s^{Y,l}$ for such a set of points is then $O((N_s+M)\log(N_s+M))$ using a standard NUFFT algorithm.

To apply this strategy to general sets of targets, $\{\mathbf{T}_j\}$ where $\mathbf{T}_j = (v_j, w_j) \in \mathcal{C}$, we use an apparatus similar to that used for the form operator. As before, define $w^{(i)} = \eta(t_i + 1)/2$, where $t_1 < \cdots < t_{M_{\text{leg}}}$ are the M_{leg}-th order Legendre nodes. Defining $\bar{v}_j = v_j - \xi w_j/\eta$, we can then interpolate $\mathbf{A}^{Y,l}(\{\mathbf{T}_j\}; M)\mathbf{c}$ by using the values $\mathbf{A}^{Y,l}(\{\mathbf{T}_j^{(i)}\}; M)\mathbf{c}$ where $\mathbf{T}_j^{(i)} = (\bar{v}_j + \xi w^{(i)}/\eta, w^{(i)})$. Let $\lambda_1, \ldots, \lambda_{M_{\text{leg}}}$ be the barycentric interpolation weights defined in Equation (2.7). Then,

$$c^{(1)}(w_j)\mathbf{A}^{Y,l}(\mathbf{T}_j^{(1)}; M)\mathbf{c} + \cdots + c^{(M_{\text{leg}})}(w_j)\mathbf{A}^{Y,l}(\mathbf{T}_j^{(M_{\text{leg}})}; M)\mathbf{c}$$

is a spectrally accurate approximation of $\mathbf{A}^{Y,l}(\mathbf{T}_j; M)\mathbf{c}$, where

$$c^{(i)}(w_j) = \frac{\frac{\lambda_i}{w_j - w^{(i)}}}{\sum_{n=1}^{M_{\text{leg}}} \frac{\lambda_n}{w_j - w^{(n)}}} \,. \tag{8.18}$$

Because each of the sets $\{\mathbf{T}_j^{(i)}\}$ has charges with a fixed y-coordinate, the NUFFT-accelerated approach described above can be applied. The resulting algorithm is provided in Algorithm 3 and has $O(M_{\text{leg}}(N_s + M)\log(N_s + M))$ computational complexity. The interpolated values provide a spectrally accurate approximation. For non-oscillatory kernels like Yukawa and Laplace, we find that 25 Legendre nodes are sufficient for double precision accuracy.

Algorithm 3 Accelerated algorithm for evaluating $\mathbf{u} \approx \mathbf{A}_s^{Y,l}(\{\mathbf{T}_j\}; M)\mathbf{c}$.

Input: $\{\mathbf{T}_j\}$, $\mathbf{c}$, M, M_{leg}.

$t_1, \ldots, t_{M_{\text{leg}}} \leftarrow M_{\text{leg}}$-th order Legendre nodes
$\lambda_1, \ldots, \lambda_{M_{\text{leg}}} \leftarrow$ Barycentric weights ▷ See Equation (2.7).
for $i = 1, \ldots, M_{\text{leg}}$ **do**
    $w^{(i)} \leftarrow w_j(t_i + 1)/2$
    for $j = 1, \ldots, N_s$ **do**
        $(v_j, w_j) \leftarrow \mathbf{S}_j$
        $\bar{v}_j \leftarrow v_j - \xi w_j/\eta$
        $v_j^{(i)} \leftarrow \bar{v}_j + \xi w^{(i)}/\eta$
$\mathbf{u} \leftarrow 0$
for $i = 1, \ldots, M_{\text{leg}}$ **do**
    $\tilde{\mathbf{u}} \leftarrow \mathbf{D}_s^{(Y,l,4)}(w^{(i)})\mathbf{c}$
    $\tilde{\mathbf{u}} \leftarrow \mathbf{N}^{(2)}\left(\left\{2\pi v_j^{(i)}/d\right\}, M\right)\tilde{\mathbf{u}}$
    $\tilde{\mathbf{u}} \leftarrow \mathbf{D}_s^{(Y,l,3)}(\{v_j^{(i)}\})\tilde{\mathbf{u}}$
    for $n = 1, \ldots, n_t$ **do**
        $u_n \leftarrow u_n + c^{(i)}(w_n)\tilde{u}_n$

Output: $\mathbf{u}$.

CHAPTER 9

NUMERICAL RESULTS

We have implemented the algorithms described in this paper in Fortran. Our implementation uses the fmm2d library (Askham et al., 2021) for the free-space FMMs and the finufft package (Barnett and Magland, 2018),(Barnett et al., 2019) for the NUFFTs. The code is compiled using gfortran 9.3.0 with -O3 option. The results shown in this section were obtained on a single core of a laptop with Intel(R) 2.40GH i9-10885H CPU.

We first test the performance of the code in the high accuracy regime. Table 9.1 shows the results for the modified Helmholtz kernel with precision set to 10^{-12}. $40,000$ source points are placed in the fundamental unit cell with a uniform random distribution, with 500 equispaced target points on each side of the unit cell to check the enforcement of periodic conditions. In Table 9.1, A is the aspect ratio defined at Definition 2, t_{per} is the time for applying the periodizing operator, t_{FMM} is the time for the FMM call with sources in the near region $\mathcal{N}$ consisting of $(2m_0+1)\times(2n_0+1)$ copies of the unit cell. $n_0 = 1$ in the doubly periodic case and $n_0 = 0$ in the singly periodic case. $m_0 = 1, 2$, or 3, depending on the precise shape of the unit cell. t_{total} is the total computational time and t^0_{FMM} is the time required by the free-space FMM, with sources restricted to the fundamental unit cell alone for reference as a lower bound. All times are measured in seconds and the error is the estimated relative l^2 error in satisfying periodicity (i.e., the potential difference between the right and left sides for the singly periodic case, and the sum of potentials differences in both x and y for the doubly periodic case). P_1 and P_2 denote the imposition of periodicty in one or two dimensions, respectively. For the singly periodic case, $m_0 = 1$. That is, the central 3 cells are include in the near region. For the doubly periodic case, $m_0 = 1$ for the rectangular cell; $m_0 = 2$ for the parallelogram with $\theta = \pi/3$; and $m_0 = 3$ for the parallelogram with $\theta = \pi/6$, where θ is the angle between $\hat{\mathbf{e}}_1$ and $\hat{\mathbf{e}}_2$. The cost of the periodization step is

insensitive to the geometry of the unit cell, since we make use of acceleration with the NUFFT, and a small fraction of the total cost. The FMM for sources in the near region $\mathcal{N}$ is about one to four times more expensive than for the unit cell alone.

In our current implementation, we simply call the free-space FMM with all near region sources but with targets restricted to the unit cell. A more efficient code could be developed by taking advantage of the fact that the sources in each image cells are identical, as are the corresponding hierarchy of multipole moments. Minor modification of the FMM could reduce the cost to being within a factor of two of the FMM cost for the unit cell alone.

Similar results hold for the other kernels. In Table 9.2 we show the timings obtained for the Laplace kernel with precision $\epsilon = 10^{-9}$, and in Table 9.3, we show the timings obtained for the Stokeslet with precision $\epsilon = 10^{-6}$. The column headings have the same meaning as in Table 9.1.

Table 9.1 Timing results of the periodic FMM for the modified Helmholtz kernel with $\beta = 1$ and $40,000$ sources in the unit cell. The requested precision is $\epsilon = 10^{-12}$.

A	t_{per}	t_{FMM}	t_{total}	t^0_{FMM}	Error
P_1 : rectangle					
1	0.08	1.78	1.87	1.78	0.12e-12
10	0.08	1.95	2.03	1.61	0.69e-14
100	0.12	2.19	2.30	1.37	0.86e-15
1000	0.48	2.88	3.36	1.35	0.16e-14
P_2 : rectangle					
1	0.18	2.45	2.63	1.69	0.31e-13
10	0.17	2.48	2.65	1.62	0.44e-14
100	0.17	3.70	3.87	1.39	0.49e-15
1000	0.19	3.72	3.91	1.36	0.48e-15
P_2 : parallelogram with $\theta = \pi/3$					
2	0.18	3.40	3.59	1.82	0.20e-12
10	0.17	3.45	3.63	1.78	0.35e-12
100	0.17	4.24	4.42	1.39	0.12e-12
1000	0.19	3.84	4.03	1.36	0.45e-12
P_2 : parallelogram with $\theta = \pi/6$					
2	0.18	4.18	4.37	1.53	0.17e-12
10	0.17	3.30	3.48	1.95	0.15e-12
100	0.17	4.25	4.42	1.38	0.32e-12
1000	0.22	3.95	4.18	1.36	0.26e-12

Table 9.2 Timing results of the periodic FMM for the Laplace kernel with $40,000$ sources in the unit cell and a requested precision of $\epsilon = 10^{-9}$.

A	t_{per}	t_{FMM}	t_{total}	t^0_{FMM}	Error
P_1 : rectangle					
1	0.06	0.56	0.62	0.64	0.10D-09
10	0.07	0.83	0.90	0.66	0.98D-11
100	0.08	0.64	0.73	0.44	0.21D-12
1000	0.23	1.02	1.25	0.40	0.15D-12
P_2 : rectangle					
1	0.14	1.03	1.17	0.54	0.11D-10
10	0.12	0.81	0.93	0.66	0.63D-11
100	0.12	1.14	1.27	0.44	0.13D-11
1000	0.13	1.48	1.61	0.40	0.52D-13
P_2 : parallelogram with $\theta = \pi/3$					
2	0.14	1.13	1.27	0.65	0.26D-10
10	0.12	1.17	1.29	0.72	0.13D-09
100	0.12	1.64	1.77	0.44	0.31D-09
1000	0.13	1.29	1.42	0.40	0.24D-09
P_2 : parallelogram with $\theta = \pi/6$					
2	0.13	1.76	1.90	0.46	0.20D-10
10	0.13	1.11	1.24	0.62	0.23D-09
100	0.12	1.66	1.78	0.45	0.60D-10
1000	0.13	1.28	1.42	0.40	0.34D-09

Table 9.3 Timing results of the periodic FMM for the Stokeslet with $40,000$ sources in the unit cell and a requested precision of $\epsilon = 10^{-6}$.

A	t_{per}	t_{FMM}	t_{total}	t^0_{FMM}	Error
P_1 : rectangle					
1	0.09	1.05	1.14	0.81	0.19D-06
10	0.07	1.17	1.24	0.94	0.12D-06
100	0.08	1.09	1.18	0.78	0.16D-08
1000	0.19	1.31	1.50	0.69	0.39D-10
P_2 : rectangle					
1	0.25	1.63	1.89	0.69	0.21D-07
10	0.24	1.31	1.55	0.94	0.53D-07
100	0.23	1.42	1.65	0.79	0.73D-08
1000	0.24	2.30	2.55	0.69	0.12D-09
P_2 : parallelogram with $\theta = \pi/3$					
2	0.25	1.50	1.75	0.78	0.35D-07
10	0.24	1.55	1.80	0.88	0.19D-06
100	0.24	2.30	2.55	0.80	0.57D-06
1000	0.25	2.31	2.56	0.69	0.39D-06
P_2 : parallelogram with $\theta = \pi/6$					
2	0.25	2.24	2.50	0.88	0.72D-07
10	0.24	1.58	1.83	0.77	0.47D-06
100	0.24	2.29	2.53	0.82	0.32D-06
1000	0.25	2.27	2.52	0.68	0.61D-06

Chapter 10

VARIANTS OF GENERALIZED GAUSSIAN QUADRATURE

Boundary integral equations and Nyström discretization methods provide a powerful tool for computing the solution of Laplace and Helmholtz boundary value problems (BVP). Using the fundamental solution (free-space Green's function) for these equations we can convert such problems into boundary integral equations, thereby reducing the dimension of the problem. More precisely, a BVP in two-dimension (2D) is converted via the so-called jump relations to an integral equation for an unknown function on a one-dimension (1D) curve. The resulting geometric simplicity and reduced dimensionality allow for high-order accurate numerical solutions with greater efficiency than standard finite-difference or finite-element discretizations.

Consider the Helmholtz equation:

$$\begin{aligned} (\Delta + k^2)u(\mathbf{x}) &= 0, \text{in } D \\ u(\mathbf{x}) &= g(\mathbf{x}), \text{on } \Gamma \ , \end{aligned} \tag{10.1}$$

where D is a bounded domain with boundary Γ. Let G_k be the Green's function for the Helmholtz equation in two dimensions, i.e.,

$$G_k(\mathbf{x}, \mathbf{y}) = \frac{i}{4} H_0^{(1)}(k|\mathbf{x} - \mathbf{y}|) \ .$$

The standard layer potentials are then the single layer potential,

$$\mathcal{S}[\mu](\mathbf{x}) = \int_\Gamma G_k(\mathbf{x}, \mathbf{y})\mu(\mathbf{y})\, ds \ , \tag{10.2}$$

and the double layer potential,

$$\mathcal{D}[\mu](\mathbf{x}) = \int_\Gamma \mathbf{n}(\mathbf{y}) \cdot \nabla_y G_k(\mathbf{x}, \mathbf{y})\mu(\mathbf{y})\, ds \ , \tag{10.3}$$

where $\mathbf{n}(\mathbf{y})$ denotes the outward unit normal vector at $\mathbf{y} \in \Gamma$. Taking $u(\mathbf{x}) = ic\mathcal{S}[\mu](\mathbf{x}) + \mathcal{D}[\mu](\mathbf{x})$, i.e. using a combined layer potential representation, and applying the jump relations for $\mathcal{S}$ and $\mathcal{D}$, we obtain the following formula as $\mathbf{x} \in D$ tends to some point $\mathbf{y}_0$ on Γ:

$$-\frac{1}{2}\mu(\mathbf{y}_0) + ic\mathcal{S}[\mu](\mathbf{y}_0) + \mathcal{D}[\mu](\mathbf{y}_0) = g(\mathbf{y}_0) \ . \tag{10.4}$$

When k^2 is not an eigenvalue of the Laplace operator for these boundary conditions on D, the Equation (10.4) is an invertible second-kind integral equation (Colton and Kress, 1983).

The Nyström method discretizes the integral Equation (10.4) using a quadrature rule, with the unknown μ represented by its values at the discretization nodes. Thus, Equation (10.4) becomes a linear system of the form

$$-\frac{1}{2}\mu_i + \sum_{j=1}^{N} w_j^{(i)} \left(icG_k(\mathbf{y}_i, \mathbf{y}_j) + \mathbf{n}(\mathbf{y}_j) \cdot \nabla_y G_k(\mathbf{y}_i, \mathbf{y}_j)\right) \mu_j \ , \tag{10.5}$$

where $\{\mathbf{y}_j\}$ is a set of quadrature nodes, $\{w_j^{(i)}\}$ is a set of quadrature weights for each "target" point $\mathbf{y}_i$, and $\mu_i \approx \mu(\mathbf{y}_i)$.

One of the challenges in implementing integral equation methods is that the kernels, e.g., G_k and $\mathbf{n} \cdot \nabla_y G_k$, have logarithmic singularities as functions of the boundary so that standard quadrature rules cannot be applied with high order accuracy. We will briefly review some of the available quadrature schemes for singular integrals. For now, let Γ be a single curve which has the parameterization $\boldsymbol{\gamma}(t) = (\gamma_1(t), \gamma_2(t))$ with $\boldsymbol{\gamma} : [a, b) \to \Gamma$. The most popular discretization schemes can be classified by the arrangement of the nodes $\mathbf{y}_j$ along the curve Γ.

The equispaced schemes defined the set $\{\mathbf{y}_j\}$ using equispaced sampling in either the parameter space $[a, b)$ or arclength along the curve Γ. Typically, the quadrature rule is then based on the trapezoidal rule, which is high order accurate for smooth functions on the curve, with a "local correction" applied to obtain the quadrature rule for each target (Kapur and Rokhlin, 1997; Alpert, 1999). Global

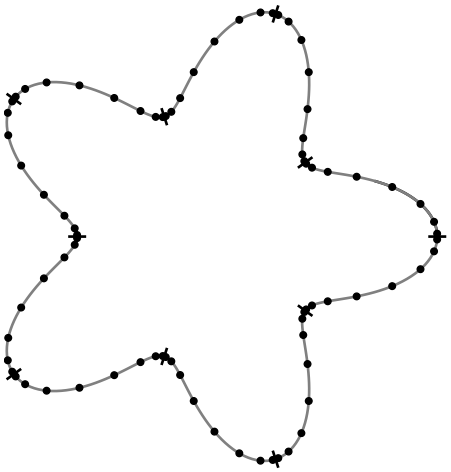

Figure 10.1 Illustration of a panel based discretization.

schemes for equispaced discretizations have also been considered (Kress, 1991).

Equispaced sampling is not efficient when there is some local feature of the boundary, Γ, the boundary data, g, or the unknown density, μ, which needs to be resolved. To address this issue, the panel-based schemes defined the set $\{\mathbf{y}_j\}$ by adaptively dividing the curve into "panels" and taking the nodes $\{\mathbf{y}_j\}$ to be the union of scaled Legendre nodes defined on each panel. See Figure 10.1 for an illustration.

For integration over a given panel, the standard Gauss-Legendre rule provides high precision for targets which are sufficiently far from that panel. The "self" panels which contain the target require a special quadrature rule for the corresponding singular integral over that panel. Likewise, the "neighbor" panels which are adjacent to the self panel require a special rule as well, one which accounts for any of a continuous range of possible nearby singularities. The generalized Gaussian quadrature framework of (Bremer et al., 2010b) is an automated approach to designing quadrature rules for any finite set of integrands based on matrix compression and a robust optimization procedure for the nonlinear problem of finding optimal nodes and weights. In this framework, the continuous range of possible nearby singularities must be discretized, resulting in a large set of integrands. This set can be compressed but the resulting rules ultimately require a relatively large number of nodes. Other approaches include the Helsing

kernel-split quadrature (Helsing, 2009), which leverages analytical knowledge of the singularity, and quadrature-by-expansion (Klöckner et al., 2013), which first computes expansion coefficients for the layer potential away from the boundary and then evaluates that expansion at the target point.

The rest of this chapter is organized as follows. We give a brief explanation of classical Gaussian quadrature rules for integrals with logarithmic singularity as well as some panel-based schemes in section 10.2 and section 10.3. Methods of constructing the three-panel rule are given in detail in section 10.4. Numerical results and convergence performance are demonstrated in section 10.5.

10.1 Details of Panel-Based Quadrature for Layer Potentials

In this chapter, we outline a standard Nyström discretization strategy for integral equations of the form

$$\mu(\mathbf{x}) + \int_{\Gamma} K(\mathbf{x}, \mathbf{y})\mu(\mathbf{y})\, ds = f(\mathbf{x}) \tag{10.6}$$

where $\mathbf{x} \in \Gamma$ and $K(\mathbf{x}, \mathbf{y})$ may be written as $K(\mathbf{x}, \mathbf{y}) = \phi_1(\mathbf{x}, \mathbf{y}) + \phi_2(\mathbf{x}, \mathbf{y}) \log |\mathbf{x} - \mathbf{y}|$ with both $\phi_1(\mathbf{x}, \mathbf{y})$ and $\phi_2(\mathbf{x}, \mathbf{y})$ smooth functions of $\mathbf{x}$ and $\mathbf{y}$. As in the previous section, we assume that the boundary curve Γ is the image of a smooth, 2π-periodic function $\boldsymbol{\gamma}$, i.e. $\boldsymbol{\gamma} : [0, 2\pi) \to \Gamma$. Further, we assume that $\boldsymbol{\gamma}$ is regular, i.e. $\boldsymbol{\gamma}'(t) \neq 0$ for any t.

Remark 9. In the case of the combined-field layer potential, for which $K(\mathbf{x}, \mathbf{y}) = -2(\mathbf{n}(\mathbf{y}) \cdot \nabla_y G_k(\mathbf{x}, \mathbf{y}) + ic G_k(\mathbf{x}, \mathbf{y}))$, the functions ϕ_1 and ϕ_2 are known analytically, see (DLMF, 2020, §10.8). Such explicit knowledge is the basis for applying kernel-split quadrature, see, *inter alia*, (Helsing and Holst, 2015), which requires an algorithm for evaluating the functions ϕ_1 and ϕ_2. For the generalized Gaussian quadrature rules developed in the present work, it is sufficent to know that the functions ϕ_1 and ϕ_2 exist; an explicit algorithm for evaluating these functions is

not required.

Let $t_1, \ldots, t_q$ and $w_1, \ldots, w_q$ be the Gauss-Legendre nodes and weights of order q. A composite Gauss-Legendre discretization of Γ is based on dividing Γ into n contiguous segments, $\Gamma = \cup_{i=1}^{n} \Gamma_i$, called panels and defining the boundary nodes to be given by a scaled copy of the standard Gauss-Legendre nodes on each panel. In particular, if we have $\Gamma_i = \boldsymbol{\gamma}([a_{i-1}, a_i))$ with $0 = a_0 < a_1 < \cdots < a_n = 2\pi$, then the boundary nodes on each panel, $\boldsymbol{y}_j^{(i)} \in \Gamma_i$ for $j = 1, \ldots, q$, may be defined by $\boldsymbol{y}_j^{(i)} = \boldsymbol{\gamma}(t_j^{(i)})$ with

$$t_j^{(i)} = a_{i-1} + (t_j + 1)\frac{a_i - a_{i-1}}{2} \, . \tag{10.7}$$

In a Nyström discretization, μ is represented by its values at the discretization nodes, $\mu_j^{(i)} = \mu\left(\boldsymbol{y}_j^{(i)}\right)$. To solve Equation 10.6, we must then be able to evaluate

$$\int_\Gamma K(\mathbf{x}, \mathbf{y}) \, ds$$

with $\mathbf{x} = \mathbf{y}_j^{(i)}$ for each $i = 1, \ldots, n$ and $j = 1, \ldots, q$. Because of the singularity in K, the standard (scaled) Gauss-Legendre weights cannot achieve high-precision for panels which are too close to $\mathbf{x}$. On the panel Γ_i, we consider three different quadrature strategies, depending on the relative location of $\mathbf{x}$.

Self interaction If $\mathbf{x} \in \Gamma_i$, the integral over Γ_i contains the singularity and requires a special quadrature. After some simplifications and rescaling, the corresponding integral in parameter space is of the form

$$\int_{-1}^{1} \psi_1(t) + \psi_2(t) \log|t - t_j| \, dt \, , \tag{10.8}$$

where ψ_1 and ψ_2 are smooth functions and $j \in \{1, \ldots, q\}$.

Neighbor interaction When $\boldsymbol{x} \in \Gamma_{i-1}$ or $\boldsymbol{x} \in \Gamma_{i+1}$ (setting $\Gamma_0 = \Gamma_n$ and $\Gamma_{n+1} = \Gamma_1$), the kernel $K(\mathbf{x}, \mathbf{y})$ is not singular on Γ_i. However, because the singularity is near the sub-interval, standard quadrature rules for smooth functions are not efficient. Unlike the singular case, the location of this singularity is not drawn from a fixed set after rescaling. We thus require a quadrature rule which is accurate for integrals of the form

$$\int_{-1}^{1} \psi_1(t) + \psi_2(t) \log |t - \tilde{t}| \, dt \, , \tag{10.9}$$

where $\tilde{t} \in [1 + \delta, 5]$ or $[-5, 1 - \delta]$ for some small $\delta > 0$.

Well-separated interaction Finally, we assume that if $\mathbf{x}$ is on any non-self and non-neighbor panel, then it is at a distance greater than some fraction, say $1/4$, of the panel length, $|\Gamma_i|$, from the panel. We approximate this locally by requiring that no panel is more than twice the length of its neighbors; equivalently,

$$|\Gamma_i| \in \left[\frac{\min(|\Gamma_{i-1}|, |\Gamma_{i+1}|)}{2}, 2 \max(|\Gamma_{i-1}|, |\Gamma_{i+1}|) \right] \, , \tag{10.10}$$

which we refer to as a *level-restriction* on the panel discretization.

In this case, the integrand is relatively smooth and we apply the scaled Gauss-Legendre rule, i.e.,

$$\int_{\Gamma_i} K(\mathbf{x}, \mathbf{y}) \mu(\mathbf{y}) \, ds \approx \sum_{j=1}^{q} K\left(\mathbf{x}, \boldsymbol{\gamma}\left(t_j^{(i)}\right)\right) \mu_j^{(i)} \left|\boldsymbol{\gamma}'\left(t_j^{(i)}\right)\right| \frac{w_j (a_i - a_{i-1})}{2} \, . \tag{10.11}$$

As the panels are refined, the error in this rule does not converge to zero under the assumptions above (the lowest precision typically being when $\boldsymbol{x}$ is located on a neighbor of a neighbor panel). However, the error will converge to a precision determined by the order of the quadrature rule and the relative distance of the target node. We find that the level-restriction described above and setting $q = 16$ is sufficient for about 12 digits of precision in our examples. These issues

are discussed in greater detail in, *inter alia*, (Epstein et al., 2013; af Klinteberg and Tornberg, 2017; Davis and Rabinowitz, 1984).

Remark 10. The level-restriction property only guarantees that panels are well-separated locally. For domains with narrow features, it is still possible that nodes beyond the self and neighbor panels are nearby. While this problem is eventually alleviated as the discretization is refined, it may be more efficient to treat these cases using either an oversampled Gauss-Legendre rule or adaptive quadrature.

10.2 Generalized Gaussian Quadrature

The self and neighbor interactions described in the previous section, having either singular or nearly singular integrands, require some specialized quadrature rules. In this section, we briefly review the generalized Gaussian quadrature framework of (Bremer et al., 2010b) for computing such rules and then explain the standard approach to generalized Gaussian quadrature for self and neighbor interactions.

10.2.1 Optimization Procedure

Let ϵ_{quad} be a target precision and let $\{\chi_j\}_{j=1}^{2m}$ be a set of functions on the interval $[-1, 1]$. Consider the problem of finding nodes $\xi_1, \ldots, \xi_{n_{\text{quad}}}$ and weights $\omega_1, \ldots, \omega_{n_{\text{quad}}}$ such that

$$\left| \int_{-1}^{1} \chi_j(t)\, dt - \sum_{l=1}^{n_{\text{quad}}} \chi_j(\xi_l)\omega_l \right| \leq \epsilon_{\text{quad}} \,, \tag{10.12}$$

for each $j = 1, \ldots, 2m$. For any set of $n_{\text{quad}} = 2m$ distinct nodes, computing appropriate weights is a trivial linear problem — though it can be unstable to compute these weights for certain arrangements of nodes — and the resulting rule is termed a generalized Cauchy rule. The challenge is in designing an efficient quadrature rule, i.e., one with as few nodes and weights as possible. A rule with $n_{\text{quad}} = m$ nodes and weights that satisfies Equation (10.12) is optimal in some

sense and termed a generalized Gaussian quadrature rule, though a rule with fewer nodes is possible if the (numerical) dimension of the set $\{\chi_j\}_{j=1}^{2m}$ is less than $2m$.

Let ϵ_{disc} and ϵ_{rank} be two further precision variables (to account for accumulated round-off and other numerical artifacts) satisfying $\epsilon_{\text{disc}} < \epsilon_{\text{rank}} \leq \epsilon_{\text{quad}}$. The algorithm of (Bremer et al., 2010b) attempts to compute a Gaussian quadrature rule in three stages:

Stage 1: discretization and compression To discretize the problem, a highly-refined, composite Gauss-Legendre grid with n_{disc} nodes, $\{\tilde{\xi}_j\}_{j=1}^{n_{\text{disc}}}$, is computed such that the interpolants defined on this grid for the functions in the set $\{\chi_j\}_{j=1}^{2m}$ agree with the functions themselves to precision ϵ_{disc} in the L^2 norm. After scaling, it is then possible to apply the standard singular value decomposition (SVD) or a rank revealing QR decomposition to obtain an L^2-orthonormal set of functions, $\{u_j\}_{j=1}^{r}$ which spans the set $\{\chi_j\}_{j=1}^{2m}$, at least to precision ϵ_{rank}. If there is significant decay in the singular values of this system, r may be smaller than $2m$, meaning that the set of functions to integrate can be compressed.

Stage 2: a generalized Cauchy rule The functions u_j are defined by interpolation of their values on the n_{disc} nodes of the composite Gauss-Legendre grid defined in stage 1. Thus, the natural composite Gauss-Legendre quadrature rule may be considered exact for these functions; in particular, the system

$$\begin{pmatrix} u_1(\tilde{\xi}_1) & u_1(\tilde{\xi}_2) & \cdots & u_1(\tilde{\xi}_{n_{\text{disc}}}) \\ u_2(\tilde{\xi}_1) & u_2(\tilde{\xi}_2) & \cdots & u_2(\tilde{\xi}_{n_{\text{disc}}}) \\ & \vdots & & \\ u_r(\tilde{\xi}_1) & u_r(\tilde{\xi}_2) & \cdots & u_r(\tilde{\xi}_{n_{\text{disc}}}) \end{pmatrix} \mathbf{w} = \begin{pmatrix} \int_{-1}^{1} u_1(t)\,dt \\ \int_{-1}^{1} u_2(t)\,dt \\ \vdots \\ \int_{-1}^{1} u_r(t)\,dt \end{pmatrix} \tag{10.13}$$

has a solution with $\mathbf{w}$ given by the scaled composite Gauss-Legendre weights. An r-sparse solution of Equation (10.13) provides a generalized Cauchy rule, which is the starting point for the next stage. This r-sparse solution must exist and may be computed stably by appropriately scaling the columns and applying a

rank-revealing QR decomposition.

Stage 3: iterated thinning and continuous optimization of nodes In this stage, the algorithm attempts to find an $n-1$ node rule starting from an n node rule. This can be accomplished by removing one node-and-weight pair from the quadrature rule at a time and applying local optimization on the remaining nodes and weights to see if an acceptably precise $n-1$ node rule can be reached from that starting configuration. The local optimization can be performed with a damped Gauss-Newton type iteration. If an acceptable $n-1$ node rule is reached, the process repeats. If no acceptable $n-1$ node rule is found the process terminates.

Remark 11. Generalized Gaussian quadrature rules are typically computed in an offline fashion and stored in a file for later use. As such, these calculations are often performed in quadruple-precision arithmetic to obtain full double precision, i.e. $\epsilon_{\text{quad}} \approx 2 \cdot 10^{-16}$, in the final quadrature rule. Indeed, the quadrature rules reported in this paper were computed using quadruple-precision arithmetic. However, the use of extended precision is not strictly required for rules with high precision, say $\epsilon_{\text{quad}} \approx 10^{-13}$, as the stages outlined above are reasonably stable.

10.2.2 Standard Quadrature for Self and Neighbor Interactions

As noted in Section 10.1, the original GGQ approach to quadrature on curves is based on q "self" quadrature rules, one for each node on the panel, and a universal "neighbor" quadrature rule which treats a range of possible locations for singularities on the neighboring panel. Once the optimization machinery of the previous subsection is in place, computing these quadrature rules is simply a matter of defining the correct set of functions.

For the self interaction, we apply the GGQ optimization procedure to the sets

$$B_{\ell}^{\text{og,self}} = \{t^{j_1} + t^{j_2} \log|t - t_{\ell}| : 0 \leq j_1, j_2 < q\} ,$$

for $\ell = 1, \ldots, q$. This gives an order q rule and a set of functions of size $2q$. We denote the output nodes and weights by $t_{\ell,1}^{\mathrm{og}(q)}, \ldots, t_{\ell,m_\ell}^{\mathrm{og}(q)}$ and $w_{\ell,1}^{\mathrm{og}(q)}, \ldots, w_{\ell,m_\ell}^{\mathrm{og}(q)}$, respectively. In general, a Gaussian rule is found, i.e. $m_\ell = q$.

Remark 12. While a quadrature rule of order higher than q is possible, the overall scheme is limited to order q because of the interpolation step from the original nodes to the nodes output by the GGQ code.

For the neighbor interaction, we must discretize the continuous range of possible singularities to obtain a finite problem. In particular, we select $\delta = 10^{-5}$ and divide $[1+\delta, 5]$ into the exponentially graded intervals $[1+\delta, 1+10\delta], [1+10\delta, 1+10^2\delta], \ldots, [1+10^4\delta, 2], [2, 5]$ and define the grid $\tilde{t}_1, \ldots, \tilde{t}_{\tilde{n}}$ to be the union of 16th order scaled Legendre nodes on these intervals, so that $\tilde{n} = 96$. We then define the set

$$B^{\mathrm{og,near}} = \{t^{j_1} + t^{j_2} \log|t - \tilde{t}_{j_3}| : 0 \leq j_1, j_2 < q \text{ and } 1 \leq j_3 \leq \tilde{n}\} .$$

This set has $97q$ functions, but it is highly compressible. We denote the output nodes and weights for this set by

$$\tilde{t}_1^{\mathrm{og}(q)}, \ldots, \tilde{t}_{\tilde{m}}^{\mathrm{og}(q)}$$

and

$$\tilde{w}_1^{\mathrm{og}(q)}, \ldots, \tilde{w}_{\tilde{m}}^{\mathrm{og}(q)}$$

respectively. See tables below for examples of the number of nodes, $\tilde{m}$, used for these rules:

The neighbor rule defined here is one-sided in that it is only designed to integrate a range of singularities "to the right" of the interval. For singularities to the left, the rule defined here can be reflected.

Remark 13. An independent test of the accuracy of the quadratures obtained by GGQ is available for this kernel in both the original GGQ setting described above

Table 10.1 Cost on self panel.

polynomials	standard GGQ	threepanel
64	37	37
48	34	34
32	30	30
24	24	24
16	16	16

Table 10.2 Nearby Nodes Comparison.

polynomials	standard GGQ	threepanel
48	33	22
32	27	19
24	24	16
16	21	14

and the three panel scheme detailed in the next section. This is because there is a formula for integrals of the form $t^{j_1} \log|t - t_\ell|$ based on the Cauchy-Hadamard Theorem; see, for instance, the recursion formulas defined in (Helsing, 2009). All quadratures were checked using these formulas in quadruple precision.

10.3 Three-Panel Rule

10.3.1 Quadrature for the Merged Panel

As with the original GGQ singular integration strategy, the three panel method is based on defining an appropriate set of functions to send to the GGQ optimization procedure. By the level-restriction assumption, each of the neighbors of a given panel is at least half the length of the self. Thus, we can define a universal quadrature that integrates the density over the self panel and half the self panel length of each neighbor, see Figure 10.2 for an illustration. The remainder of each neighbor is then sufficiently separated to apply a standard, scaled Gauss-Legendre integration rule.

For singular integration on the merged panel, we then apply the GGQ optimization procedure to the sets

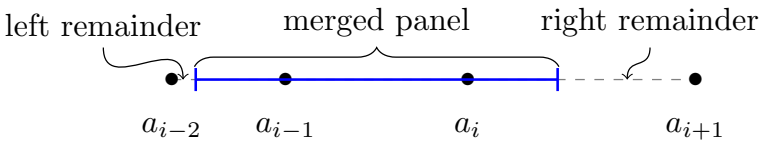

Figure 10.2 Illustration of a merged panel and left and right remainders of neighboring panels.

$$B_\ell^{\text{3p,self}} = \{t^{j_1} + t^{j_2} \log|t - t_\ell/2| : 0 \le j_1, j_2 < p\} ,$$

for $\ell = 1, \ldots, q$. The Gauss-Legendre nodes, t_ℓ, are scaled by $1/2$ because the merged panel is twice the length of the original self panel. We denote the output nodes and weights by $t_{\ell,1}^{\text{3p}(q)}, \ldots, t_{\ell,n_\ell}^{\text{3p}(q)}$ and $w_{\ell,1}^{\text{3p}(q)}, \ldots, w_{\ell,n_\ell}^{\text{3p}(q)}$, respectively.

On the merged panel, the choice of the order of the rule, p, is less obvious than in the original GGQ case. Because densities are being interpolated from degree q polynomials on three panels, the choice $p = 3q$ seems natural. However, the merged panel is only twice the length of the original self panel. Thus, for an oscillatory density, the merged panel would account for twice as many wavelengths as the original and setting $p = 2q$ seems natural. In practice, the functions in $B_\ell^{\text{3p,self}}$ are compressible and the total number of nodes obtained by setting $p = 3q$ is not much larger than the number obtained setting $p = 2q$. For the experiments below, we selected $p = 3q$.

10.3.2 Three Panel Algorithm

Let a boundary curve, Γ, be discretized as in section 10.1 and let $\boldsymbol{y}_\ell^{(i)} = \boldsymbol{\gamma}(t_\ell^{(i)}) \in \Gamma_i$ be a boundary node on the ith panel. In this section, we describe how to apply the three panel quadrature scheme to evaluate the integral corresponding to this target over the self and neighbor panels, i.e. how to evaluate

$$\int_{\Gamma_{i-1} \cup \Gamma_i \cup \Gamma_{i+1}} K(\boldsymbol{y}_\ell^{(i)}, \boldsymbol{y}) \mu(\boldsymbol{y}) \, ds \, . \tag{10.14}$$

The three panels of interest are the image of the interval $[a_{i-2}, a_{i+1})$, i.e.

$$\Gamma_{i-1} \cup \Gamma_i \cup \Gamma_{i+1} = \boldsymbol{\gamma}([a_{i-2}, a_{i+1})) \ .$$

Setting $h_i = a_i - a_{i-1}$, we break $[a_{i-2}, a_{i+1})$ into three subintervals: the merged panel $[a_{i-1} - h_i/2, a_i + h_i/2)$, the left remainder panel $[a_{i-2}, a_{i-1} - h_i/2)$, and the right remainder panel $[a_i + h_i/2, a_{i+1})$. Recall that $t_1, \ldots, t_q$ and $w_1, \ldots, w_q$ denote the standard order q Gauss-Legendre nodes and weights and that, for each panel, we have the scaled nodes $t_j^{(i)}$. To apply the three panel quadrature scheme, we must interpolate from these original nodes to scaled nodes on the merged and remainder panels.

Scaling and translating given nodes and weights defined on $[-1, 1]$ are common operations for this scheme. Let these operations be defined by

$$\begin{aligned} T(t, a, b) &= a + (t + 1)\frac{b - a}{2} \ , \\ W(w, a, b) &= w\frac{b - a}{2} \ . \end{aligned}$$

Another common operation is to interpolate a vector of function values given at some nodes $x_1, \ldots, x_m$ to a different set of nodes, $y_1, \ldots, y_n$. The $n \times m$ matrix which maps function values at the $x_1, \ldots, x_m$ to the polynomial interpolant of those values at the $y_1, \ldots, y_n$ will be denoted by $\boldsymbol{M}(y_1, \ldots, y_n; x_1, \ldots, x_m)$.

The scaled nodes and weights for the merged panel and remainder panels are:

$$
\begin{aligned}
t_j^{\mathrm{merg}} &= T(t_{\ell,j}^{3\mathrm{p}(q)}, a_{i-1} - h_i/2, a_i + h_i/2) \ , \\
w_j^{\mathrm{merg}} &= W(w_{\ell,j}^{3\mathrm{p}(q)}, a_{i-1} - h_i/2, a_i + h_i/2) \ , \\
t_j^{\mathrm{lrem}} &= T(t_j, a_{i-2}, a_{i-1} - h_i/2) \ , \\
w_j^{\mathrm{lrem}} &= W(t_j, a_{i-2}, a_{i-1} - h_i/2) \ , \\
t_j^{\mathrm{rrem}} &= T(t_j, a_i + h_i/2, a_{i+1}) \ , \\
w_j^{\mathrm{rrem}} &= W(t_j, a_i + h_i/2, a_{i+1}) \ .
\end{aligned}
$$

While the interpolation onto the left and right remainder panels should be done from the left and right neighbor panels, respectively, the nodes on the merged panel can lie on any of the three panels. Accordingly, we split the t_j^{merg} into three sets of nodes: the left merged nodes, $t_1^{\mathrm{lmerg}}, \ldots, t_{m_{\mathrm{l}}}^{\mathrm{lmerg}}$, satisfying $t_j^{\mathrm{lmerg}} < a_{i-1}$; the self merged nodes, $t_1^{\mathrm{smerg}}, \ldots, t_{m_{\mathrm{s}}}^{\mathrm{smerg}}$, satisfying $a_{i-1} \leq t_j^{\mathrm{smerg}} \leq a_i$; and the right merged nodes, $t_1^{\mathrm{rmerg}}, \ldots, t_{m_{\mathrm{r}}}^{\mathrm{rmerg}}$, satisfying $t_j^{\mathrm{rmerg}} > a_i$. Note that this splitting can contain a different number of nodes per panel depending on the target at hand, i.e. depending on the index ℓ. These numbers do not depend on which panel is being considered because the relative scales are always the same.

The relevant interpolation operators are then:

$$
\begin{aligned}
\boldsymbol{M}^{\mathrm{lrem}} &= \boldsymbol{M}(t_1^{\mathrm{lrem}}, \ldots, t_q^{\mathrm{lrem}}; t_1^{(i-1)}, \ldots, t_q^{(i-1)}) \ , \\
\boldsymbol{M}^{\mathrm{rrem}} &= \boldsymbol{M}(t_1^{\mathrm{rrem}}, \ldots, t_q^{\mathrm{rrem}}; t_1^{(i+1)}, \ldots, t_q^{(i+1)}) \ , \\
\boldsymbol{M}^{\mathrm{lmerg}} &= \boldsymbol{M}(t_1^{\mathrm{lmerg}}, \ldots, t_{m_{\mathrm{l}}}^{\mathrm{lmerg}}; t_1^{(i-1)}, \ldots, t_q^{(i-1)}) \ , \\
\boldsymbol{M}^{\mathrm{smerg}} &= \boldsymbol{M}(t_1^{\mathrm{smerg}}, \ldots, t_{m_{\mathrm{s}}}^{\mathrm{smerg}}; t_1^{(i-1)}, \ldots, t_q^{(i-1)}) \ , \\
\boldsymbol{M}^{\mathrm{rmerg}} &= \boldsymbol{M}(t_1^{\mathrm{rmerg}}, \ldots, t_{m_{\mathrm{r}}}^{\mathrm{rmerg}}; t_1^{(i-1)}, \ldots, t_q^{(i-1)}) \ .
\end{aligned}
$$

The three panel scheme can then be applied in two steps:

Step 1: Interpolate the density and Jacobian to the merged and remainder nodes Setting

$$\mathbf{f}^{(i)} = \begin{pmatrix} |\boldsymbol{\gamma}(t_1^{(i)})|\mu_1^{(i)} \\ \vdots \\ |\boldsymbol{\gamma}(t_q^{(i)})|\mu_q^{(i)} \end{pmatrix} ,$$

we perform the interpolations using the formulas: $\mathbf{f}^{\text{lrem}} = \boldsymbol{M}^{\text{lrem}}\mathbf{f}^{(i-1)}$, $\mathbf{f}^{\text{rrem}} = \boldsymbol{M}^{\text{rrem}}\boldsymbol{f}^{(i+1)}$, and

$$\mathbf{f}^{\text{merg}} = \begin{pmatrix} \boldsymbol{M}^{\text{lmerg}}\mathbf{f}^{(i-1)} \\ \boldsymbol{M}^{\text{smerg}}\mathbf{f}^{(i)} \\ \boldsymbol{M}^{\text{rmerg}}\mathbf{f}^{(i+1)} \end{pmatrix} ,$$

where the vertical concatenation in the formula for $\mathbf{f}^{\text{merg}}$ is assumed to be done in accordance with the original order of the merged nodes t_j^{merg}.

Step 2: Apply the quadrature rules We set

$$\begin{aligned} S^{\text{lrem}} &= \sum_{j=1}^{q} w_j^{\text{lrem}} f_j^{\text{lrem}} K(\mathbf{y}_\ell^{(i)}, \boldsymbol{\gamma}(t_j^{\text{lrem}})) , \\ S^{\text{rrem}} &= \sum_{j=1}^{q} w_j^{\text{rrem}} f_j^{\text{rrem}} K(\mathbf{y}_\ell^{(i)}, \boldsymbol{\gamma}(t_j^{\text{rrem}})) , \\ S^{\text{merg}} &= \sum_{j=1}^{n_\ell} w_j^{\text{merg}} f_j^{\text{merg}} K(\mathbf{y}_\ell^{(i)}, \boldsymbol{\gamma}(t_j^{\text{merg}})) , \end{aligned}$$

so that the total quadrature approximation of Equation 10.14 is $S^{\text{lrem}} + S^{\text{rrem}} + S^{\text{merg}}$.

10.4 Numerical Results

In this section, we test the accuracy and convergence of the three panel quadrature technique of the previous section on synthetic boundary value problems. The ac-

curacy and convergence are compared against the original GGQ strategy outlined in Section 10.2. In all examples, we solve the Helmholtz equation with Dirichlet boundary condition, Equation (10.1), on the interior of a starfish-like domain, (see Figure 10.3) using a double layer potential. The Dirichlet boundary data is taken to be that induced by sources (charges) on the exterior of the domain. In most examples, there are 100 sources placed around the geometry, with some separation. We compare the solution of the discretized integral equation with the analytic solution at 100 target locations randomly placed in the domain. The reported errors are the relative ℓ^2-norm error in the value of the computed solution at these locations. Typical source and target arrangements are shown in Figure 10.3. In all convergence plots, N is the number of panels used. The Helmholtz frequency is denoted by k.

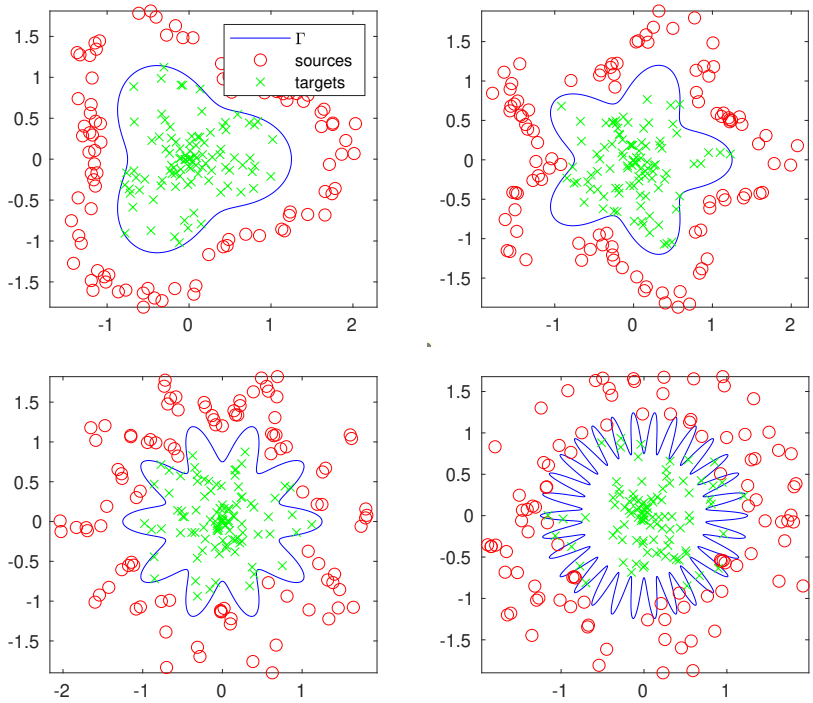

Figure 10.3 Illustration of geometries we will use in the following numerical tests. From top left to bottom right these are 3, 5, 10 and 30 arm starfish.

10.4.1 Three-Panel Rule Versus Standard GGQ

In these comparisons, the three-panel rule consists of a 34-point rule for the self interaction for each target, which integrates degree 48 polynomials and polyno-

mials times a log singularity. Then we use 16 shifted and scaled Gauss-Legendre nodes on the left remaining panel and the right remaining panel respectively. The standard GGQ rule we use in the following comparison has 16 points on the self panel, designed to integrate degree 16 polynomials and polynomials times a log singularity, and 48 points on left and right near-neighbor panels. We compare the performance of these rules on a suite of tests: increasingly complex geometries, increasing problem frequency, and a problem which requires adaptive refinement.

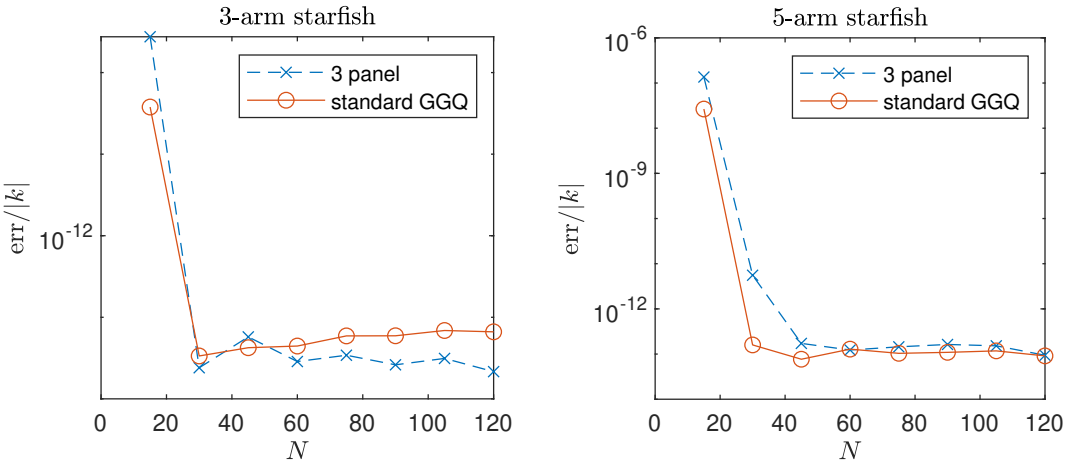

Figure 10.4 Geometry test : 3-arm starfish convergence rate and 5-arm starfish convergence rate. For comparison purpose, both rules are tested with kernel frequency variable $k = 10$ and 100 simulated source points.

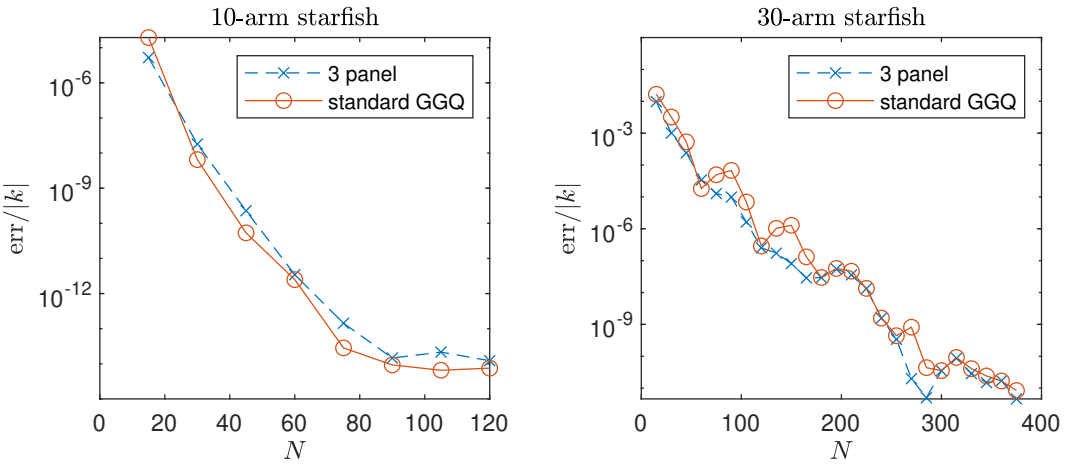

Figure 10.5 Geometry test : 10-arm starfish convergence rate and 30-arm starfish convergence rate.

Increasing the complexity of the geometry: Because the performance of a quadrature rule will depend on the arc-length density, we test on starfish ge-

ometries, see Figure 10.3, with an increasing number of "arms". The boundary in these tests is refined uniformly. In Figure 10.4 and Figure 10.5, we see that both methods have similar performance across geometries and a high rate of convergence.

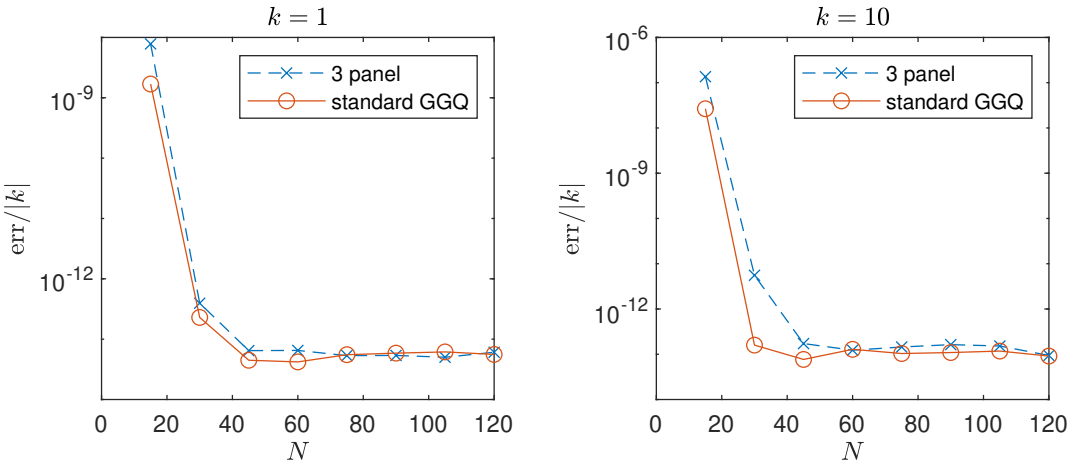

Figure 10.6 Kernel test : frequency $k = 1$ on the left and $k = 10$ on the right.

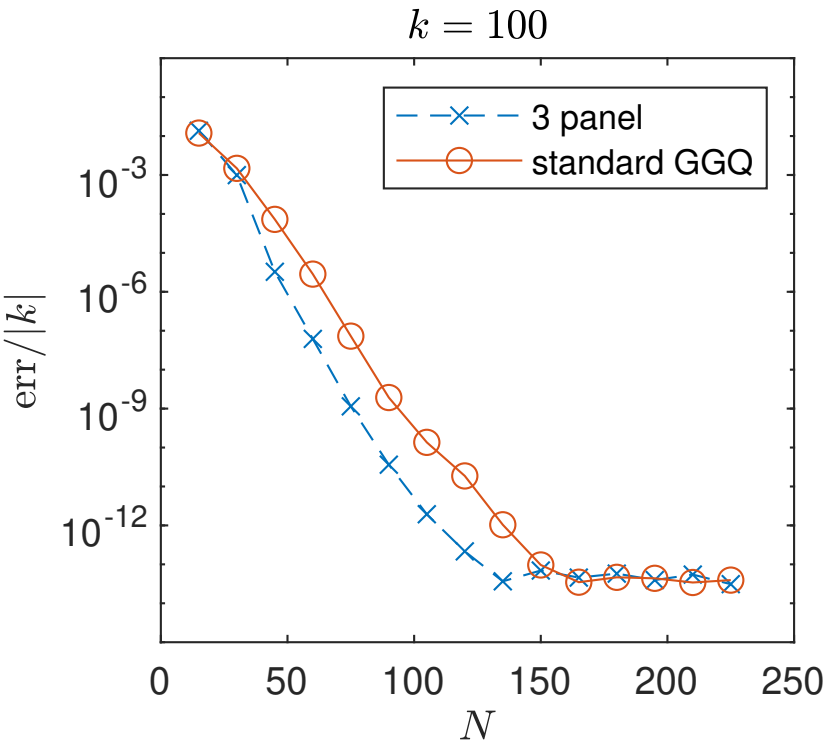

Figure 10.7 Kernel test : frequency $k = 100$

Increasing the complexity of the kernel: The performance of a quadrature rule will also depend on accurately integrating the integral kernel; we thus test

kernels of increasing complexity by solving Helmholtz problems with increasing k on a fixed domain (a five armed starfish). When the kernel frequency is small, both rules have similar performance, and the standard GGQ converges a little earlier than the three-panel rule; see Figure 10.6. When the kernel frequency is large, as in Figure 10.7, the three-panel rule notably outperforms the standard GGQ.

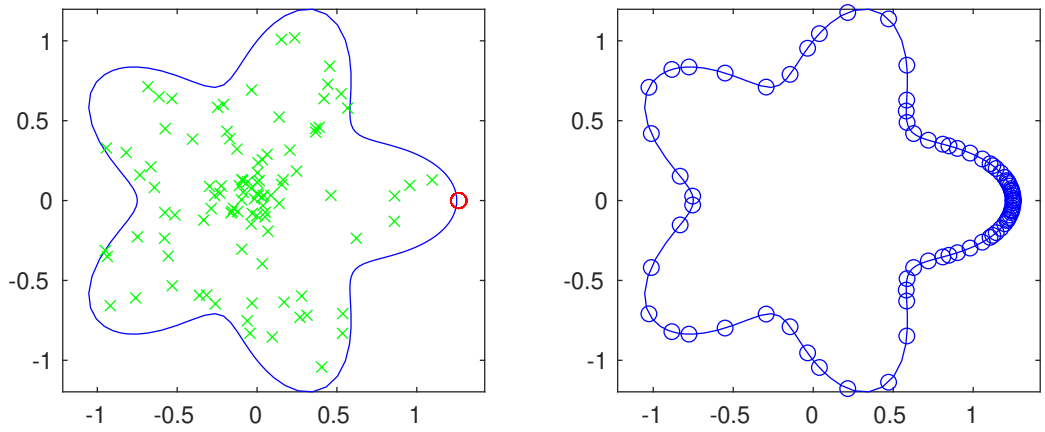

Figure 10.8 On the left is an example problem set up with many sources located close to a small region of the boundary. On the right is a an illustration of the type of adaptive panelization used to solve this problem.

A problem requiring dyadic refinement: The three-panel scheme relies on a 2:1 balance condition across panels. Thus, the quality of the quadrature scheme may suffer on a problem which requires a lot of refinement of the boundary in one region. A problem geometry which requires this is illustrated in Figure 10.8. The sources here are all localized near the point $(1, 0)$. In particular, 100 sources are placed at a distance of 0.01 to the boundary at a random angle with mean zero and standard devation 10^{-7}. The solution corresponding to these sources requires significant refinement near $(1, 0)$. In the test, we define an adaptive mesh that is approximately uniform away from $(1, 0)$ and is geometrically graded near $(1, 0)$. Specifically, for a given m, we define $M_u = 5m$ and $M_d = 5 + m$. The starfish is parameterized in the natural way over $[0, 2\pi]$. We divide $[0, 2\pi]$ uniformly into M_u subintervals. Each of the end subintervals, $[0, 2\pi/M_u]$ and $[2\pi(M_u - 1)/M_u, 2\pi]$,

are subdivide further dyadically toward 0 and 2π, respectively. The number of dyadic refinements is determined by M_d. For example, if $M_d = 4$, the subinterval $[0, 2\pi/M_u]$ is divided into

$$[0, 2\pi/(2^4 M_u)], [2\pi/(2^4 M_u), 2\pi/(2^3 M_u)], \ldots, [2\pi/(2M_u), 2\pi/M_u] \ .$$

This type of panelization is demonstrated in Figure 10.8.

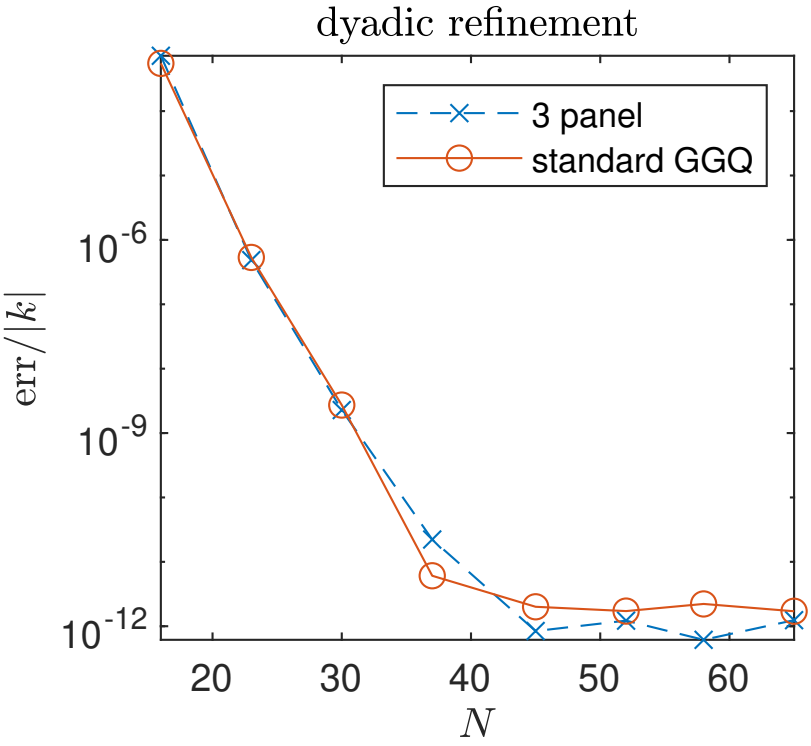

Figure 10.9 Convergence plots for the test requiring dyadic refinement.

In Figure 10.9, the three-panel rule is observed to converge as well as the standard GGQ rule using the dyadic refinement scheme.

10.4.2 Different Order Three-Panel Rules

The tests above were conducted using a three-panel rule designed to integrate 48th order polynomials, with a different rule to handle the singularity corresponding to each of the 16 nodes on any given panel. Note that here we will refer to the order of the rules as the order of these polynomials. All rules here still refer to an underlying 16th order discretization of the domain boundary.

While it is clear that a merged panel will likely require a rule that can integrate higher degree polynomials than the order of the underlying discretization (16th), it is unclear exactly how that order should be chosen. The plots in Figure 10.10 and Figure 10.11 show the convergence obtained for rules designed to integrate 16th, 24th, and 32nd order polynomials on a 5 arm starfish with $k = 10$, with the standard source locations that do not require adaptive refinement.

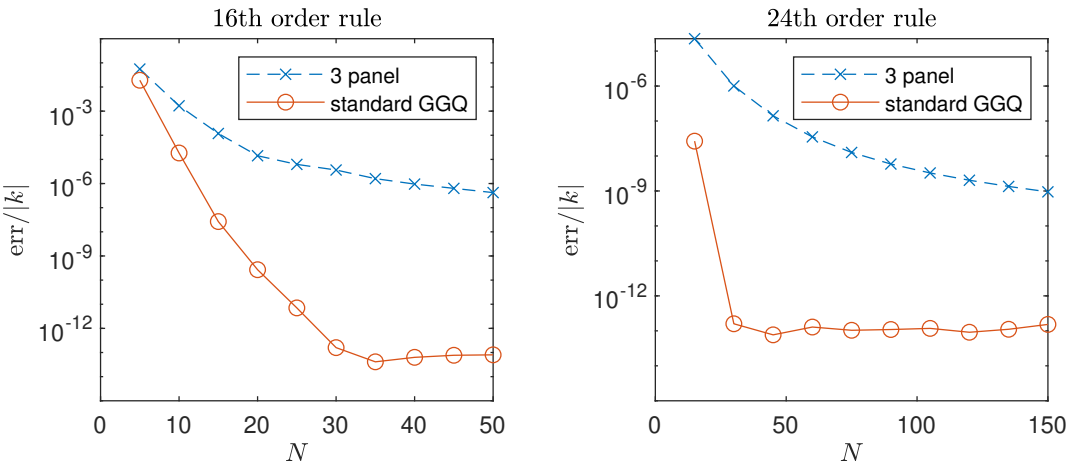

Figure 10.10 Compare different order three-panel rules: 16th order and 24th order

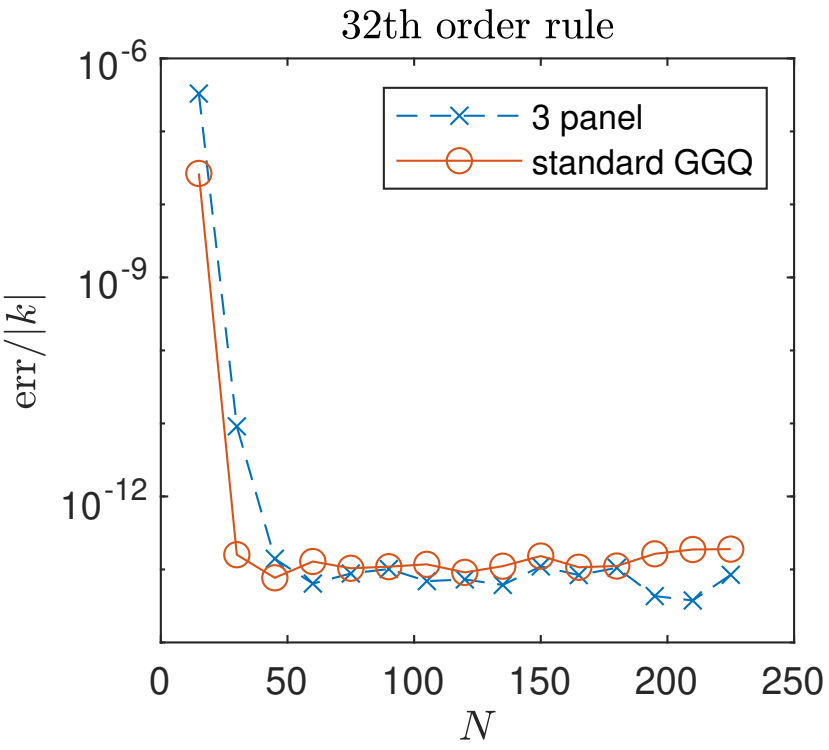

Figure 10.11 Compare different order three-panel rules: 32nd order

These results shows that lower-order (16th and 24th) three-panel rules can not provide as good results as standard GGQ. The 32nd order three-panel rule is sufficient to provide similar performance as the Standard GGQ rule. The 48th order rule only provides a marginal improvement over the 32nd order rule in the convergence rate on the synthetic tests we conducted; however, the 48th order rule only requires roughly 4 more integration nodes, as described further below.

10.4.3 Three-Panel Rule Versus New GGQ

Observing that the improved performance of the three-panel rule may owe to the fact that it is designed to integrate higher order polynomials, we have also designed a new GGQ rule which integrates 32 polynomials in the self panel and near-neighbor panel separately up to quadruple accuracy. We have average 26.875 points on the middle panel and 27 points on left and on right near-neighbor, respectively. Thus, we have this new GGQ rule with average 80.875 points together. This gives a more fair comparison with our three-panel rule because they are pre-computed by integrating same number of polynomials in each panel. The following visulization can show the performance between the 32nd order three-panel rule and the 32nd order new GGQ rule. We compare these rules on the same tests as we did above.

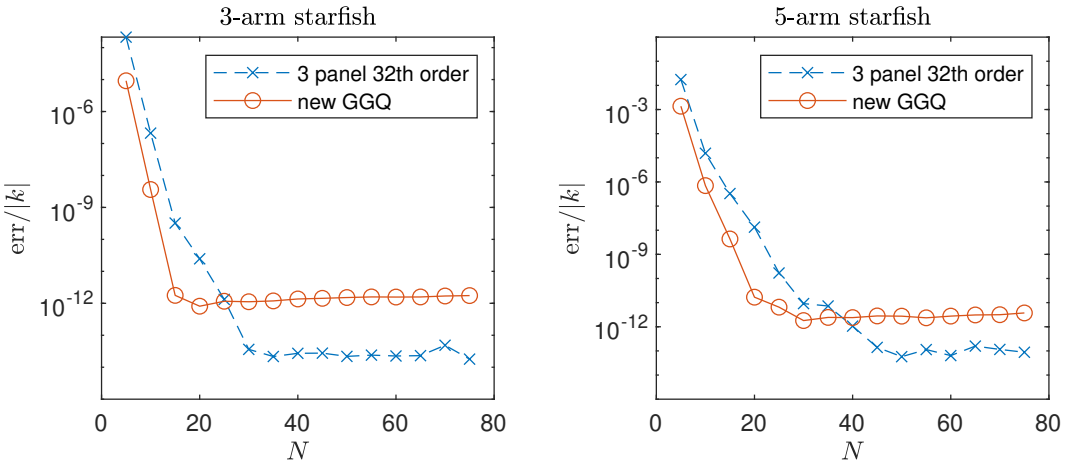

Figure 10.12 Geometry test of the 32nd order three-panel rule and new GGQ: 3-arm starfish convergence rate and 5-arm starfish convergence rate. For the purpose of comparison, both figures are plotted for $k = 10$.

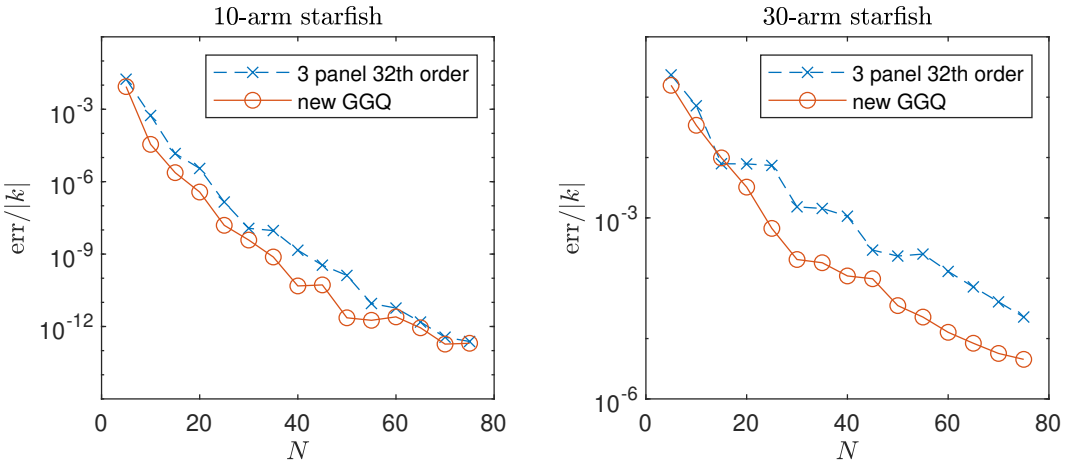

Figure 10.13 Geometry test of the 32nd order three-panel rule and new GGQ: 10-arm starfish convergence rate and 30-arm starfish convergence rate. For the purpose of comparison, both figures are plotted for $k = 10$.

Increasing the complexity of the geometry: In Figure 10.12 and Figure 10.13, we see that both 32nd order rules have similar performance. The new GGQ is converging slightly faster when the geometry is very complicated, such as on the 30-arm starfish.

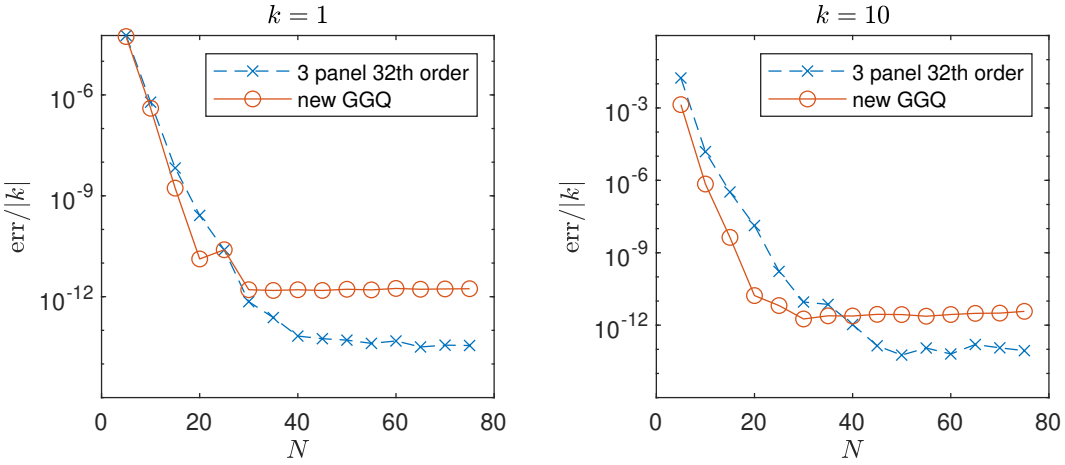

Figure 10.14 Kernel test of the 32nd order three-panel rule and new GGQ: $k = 1$ convergence rate and $k = 10$ convergence rate. For the purpose of comparison, both figures are plotted for the 5-arm starfish.

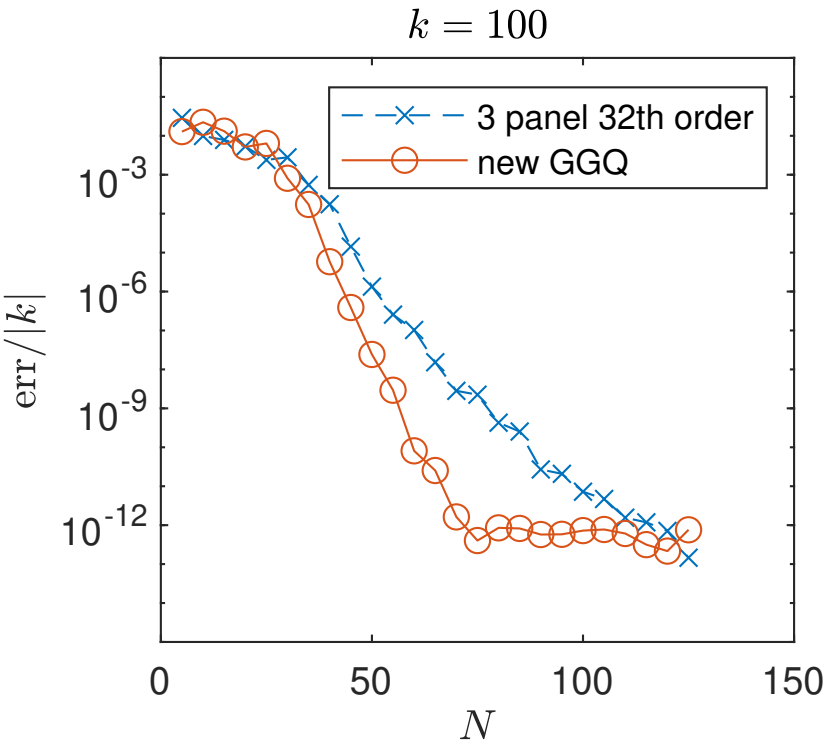

Figure 10.15 Frequency Test: 32nd order three-panel rule and new GGQ with $k = 100$ on a 5 arm starfish.

Increasing the complexity of the kernel: Both rules have similar performance across all the frequency tests; see Figure 10.14 and Figure 10.15.

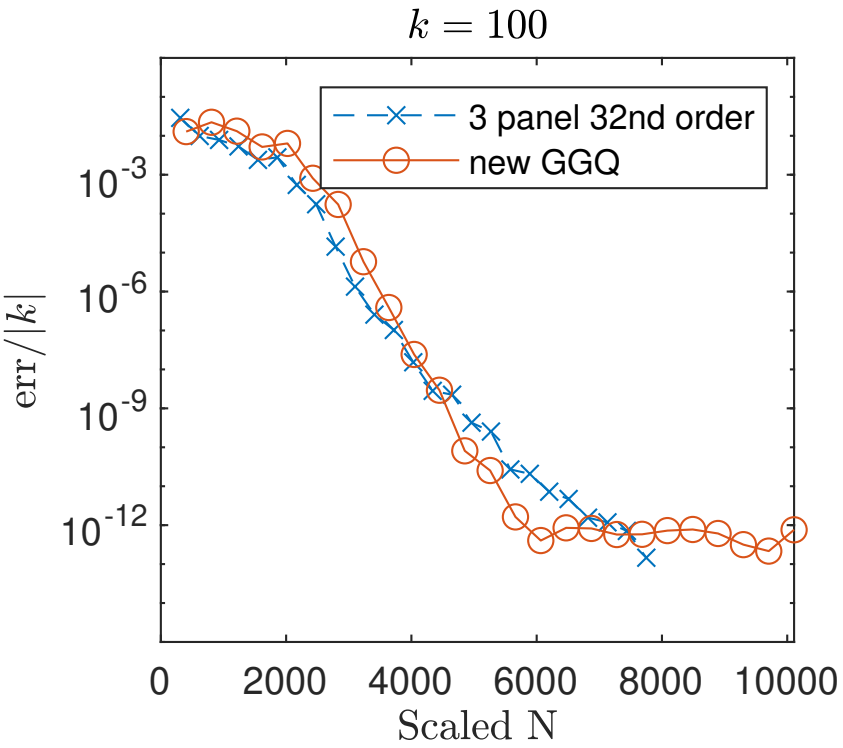

Figure 10.16 Scaled Frequency Test: 32nd order three-panel rule and new GGQ with $k = 100$ on a 5 arm starfish.The three-panel rule is scaled by 62 and the new GGQ is scaled by 80.875.

Scaling the number of panels: In the above tests, especially in Figure 10.15, we see that 32nd order new GGQ rule is outperforming 32nd order three-panel rule in terms of accuracy per panel. Scaling the number of panels by the number of interpolation nodes per target can give an idea of these rules performance in terms of accuracy per interpolation nodes. Therefore, the 32nd order new GGQ is scaled by 80.875 where 26.875 comes from the average self panel nodes for different targets and 27 nodes on each near-neighbor panels. The 32nd order three-panel rule is scaled by 62 where 30 comes from the merged self panel and 16 nodes on each remaning near-neghbor panels. After scaling, see Figure 10.16, both rules have very good and similar performance.

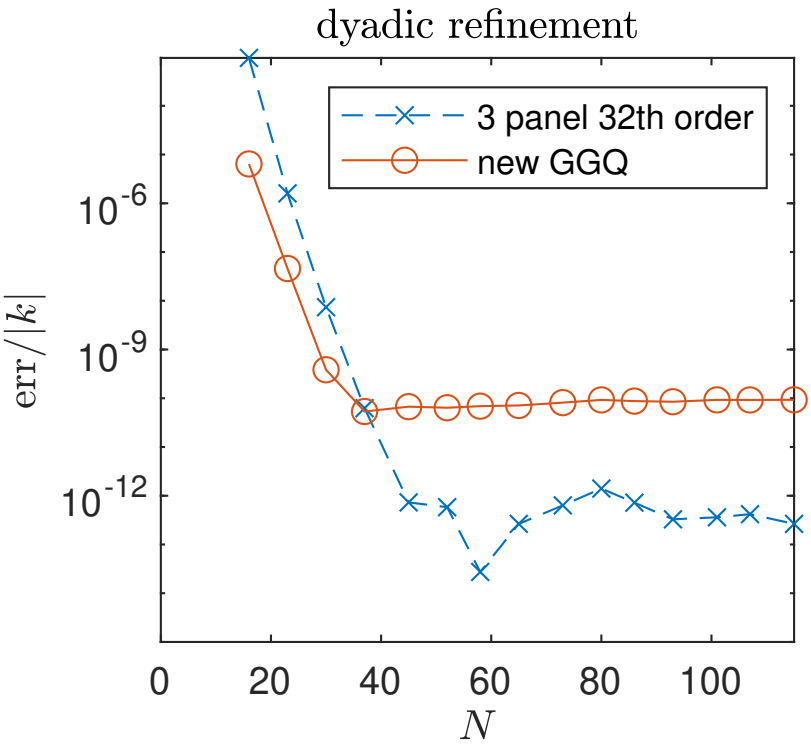

Figure 10.17 Dyadic Refinement Test: For the purpose of comparison, both rules are tested on 5-arm starfish and kernel frequency $k = 10$.

A test with dyadic refinement: On the test requiring dyadic refinement, both 32nd order rules begin converging at a similar rate. However, the new GGQ rule achieves a lower precision before flattening out. This occurs most dramatically on this test; a possible explanation is that the neighbor interaction rule is stressed by the dyadic refinement because the near singularity is effectively closer than in the other tests. See Figure 10.17.

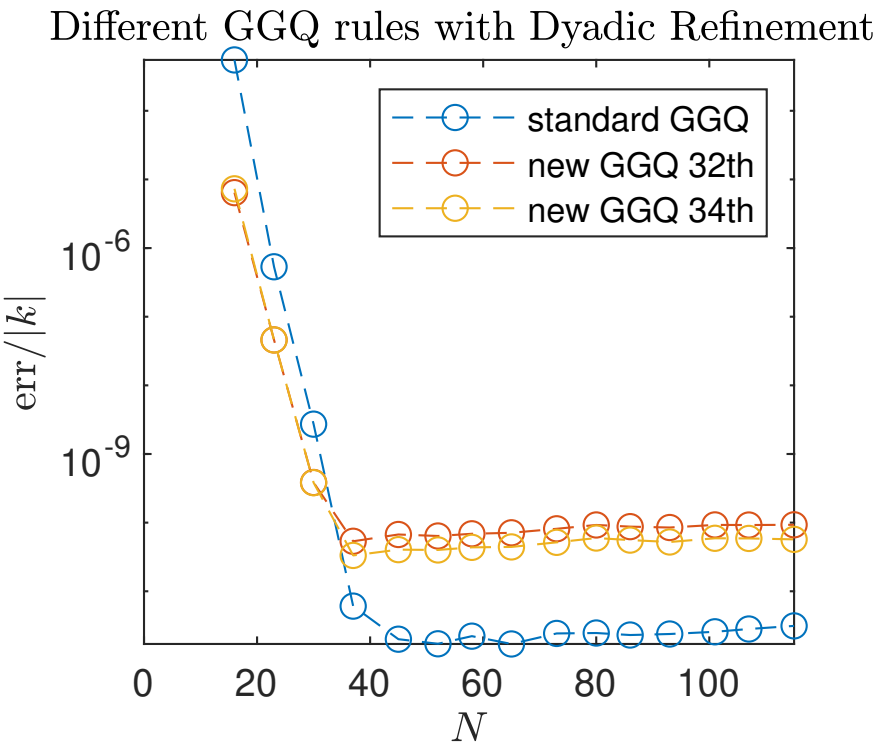

Figure 10.18 Simple comparion among standard GGQ and new GGQ rules.

There is a noticeable difference between the new GGQ and old GGQ on their level of precision when converged, see Figure 10.18 and the other tests above. The exact source of this is still being pursued. Before achieving this precision, however, the new rule appears advantageous, particularly for more complex problems.

10.4.4 Timing Complexity Results

Because the bulk of the matrix interactions are treated using the standard smooth rule, the cost of the self and neighbor interactions constitute a small portion of the overall computation of the full system matrix. Once a fast algorithm is used for the separated interactions, however, the self and neighbor interactions may contribute more significantly to the run time. For these interactions, the primary costs are interpolation and kernel evaluations. In our experience, the interpolation costs are less expensive than the kernel evaluations. We thus take the average number of support nodes used per target to account for the self and neighbor interactions as our measure of the efficiency of these rules.

The standard GGQ self rule was designed to integrate 16th order polynomials and polynomials times the appropriate log singularity, with a different rule for each target. These rules all ended up with 16 support nodes. The standard GGQ also optimized for interpolation costs and employed a symmetric rule for neighbor interactions, using 48 support nodes. Thus, each target requires a total of 112 kernel evaluations for the self and neighbor interactions.

The most performant three-panel rules are designed to integrate either 32nd or 48th order polynomials and polynomials times the appropriate log singularity on the merged panel and uses the standard smooth nodes on the remainders of the neighbors. The new GGQ rules were designed to integrate the same sets of functions but limited to the self panel. We also designed non-symmetric neighbor rules requiring fewer total nodes. The average number of total nodes for these rules is summarized in Table 10.3. In more detail, the three-panel rule requires 30 or 34 nodes on the merged self panel and 16 nodes on each of the remaining near-neighbor panel. The new GGQ requires average 26.875 or 33.625 nodes on the self panel depending on the location of target, and 27 or 33 nodes on each of the near-neighbor panel.

Table 10.3 Number of Nodes in Different Rules

polynomials	**Standard GGQ**	**New GGQ**	**Three-Panel**
48	NA	99.625	66
32	NA	80.875	62
16	112	NA	NA

Chapter 11

Conclusions and Future Work

Explicit, separable low-rank factorizations have been constructed for the periodizing operator for particle interactions governed by the modified Helmholtz, Poisson, modified Stokes, and Stokes equations in two dimensions. The factorization is based on the Sommerfeld integral representation of the Green's function, which is readily available for the modified Helmholtz and Poisson kernels, and can be derived more generally by Fourier analysis and contour integration, as done here for the modified Stokeslet or Stokeslet. In both the singly and doubly periodic cases, the ϵ-rank r of the periodizing operator is shown to be of the order $O\left(\log(1/\epsilon)\left(\log(1/\beta) + A\log(1/\epsilon)\right)\right)$, where A is the aspect ratio of the fundamental unit cell. Here, β is the parameter that defines the modified Helmholtz and modified Stokes kernels. For the Poisson and Stokes kernels, the factor $\log(1/\beta)$ disappears.

Our factorization leads to a simple fast algorithm for the action of the periodizing operators with $O(r(N_T + N_S))$ complexity - linear with respect to the number of targets and sources. When r is large, a more complicated fast algorithm, relying on the NUFFT, can be used to further speed up the calculation, reducing the complexity to $O(\log(1/\epsilon)(r\log r + (N_T + N_S)\log(1/\epsilon)))$.

There are several natural extensions or generalizations of the current work. First, the scheme can easily be extended to treat nonoscillatory kernels in three dimensions. Second, there is no essential obstacle to extending the scheme to treat oscillatory problems (such as the Helmholtz or Maxwell equations) in two and three dimensions. The various sums and integrals, however, must be treated with more care, as they are conditionally convergent, permit "quasi-periodic" boundary conditions and are subject to resonances (Wood anomalies) (Barnett and Greengard, 2010; Barnett and Greengard, 2011; Denlinger et al., 2017; Dienstfrey

et al., 2001; Enoch et al., 2001; McPhedran et al., 2000). Third, the scheme can be coupled with integral equation methods and the fast multipole method to solve periodic boundary value problems when the unit cell contains inclusions of complicated shape. Finally, more efficient versions of the FMM can be deployed to reduce the cost of handling the near region copies of the unit cell, as in the periodic version of the original scheme (Greengard and Rokhlin, 1987). This would bring into closer alignment the time t_{FMM} and t^0_{FMM} in Table 9.1,9.2,9.3. For multiple scattering problems with singly or doubly periodic boundary conditions, where the far field of a scatterer is represented by a multipole expansion, the periodic scattering matrix can be constructed via simple modifications of the algorithms in (Gan et al., 2016; Gimbutas and Greengard, 2013). This requires periodizing operators for multipole sources, which are presented in the appendices of the present paper.

In the first project of the thesis, we have formulated the periodizing operators for the Yukawa kernel and the Laplace kernel with planewave expansion. By splitting the periodizing operator into four parts, we are able to apply the Poisson summation formula on the north and south parts and develop appropriate quadrature rules for the west and east parts. We applied a limiting procedure for lower-order Laplace kernel to obtain the converged periodizing operator. Combining these planewave representations with NUFFT, we reduced the cost from $O(r(N_s + N_t))$ to $O((r + N_s + N_t)log(r + N_s + N_t))$, where r is the rank of the periodizing operators.

For the periodic fast multipole algorithm, our current work on 2D Yukawa and Laplace kernels can be extended to 3D problems for general parallelepipes. In order to have this method work in 3D, we will need to have to apply Poisson's Theorem to two of the dimensions and we use our quadrature nodes on the third dimension. Also, we can generalize this idea to the Stokes problem and the Helmholtz problem. For the Stokes problem, we may need to apply the limiting procedure to obtain the correct periodizing operator in a similar way to what we

did with the lower-order Laplace kernel. For the Helmholtz problem, we can formulate the periodizing operator like the Yukawa kernel, except we need to replace $i\kappa$ with β.

$$\begin{aligned}
\mathbf{P}_s^{(H,l)}(\mathbf{T},\mathbf{S}) &= \sum_{n=-\infty}^{-2}\sum_{m=-\infty}^{\infty} K_l\left(i\kappa R_{mn}\right) e^{il\theta_{mn}} e^{i\mathbf{k}_0\cdot\mathbf{L}_{mn}} \\
&= \sum_{n=-\infty}^{-2}\sum_{m=-\infty}^{\infty} \frac{i^l}{2(i\kappa)^l}\int_{-\infty}^{\infty}\left(\sqrt{\lambda^2+(i\kappa)^2}-\lambda\right)^l \frac{e^{-\sqrt{\lambda^2+(i\kappa)^2}(y-y_0-n\eta)}}{\sqrt{\lambda^2+(i\kappa)^2}} \\
&\cdot e^{i\lambda(x-x_0-md-n\xi)} e^{i(\alpha_0 md+\alpha_0 n\xi+(i\kappa)_0 n\eta)} d\lambda \\
&= \sum_{n=-\infty}^{-2}\sum_{m=-\infty}^{\infty} \frac{1}{2\kappa^l}\int_{-\infty}^{\infty}\left(\sqrt{\lambda^2-\kappa^2}-\lambda\right)^l \frac{e^{-\sqrt{\lambda^2-\kappa^2}(y-y_0-n\eta)}}{\sqrt{\lambda^2-\kappa^2}} \\
&\cdot e^{i\lambda(x-x_0-n\xi)} e^{i(\alpha_0 n\xi+i\kappa_0 n\eta)} \frac{2\pi}{d}\delta\left(\lambda-\alpha_0-\frac{2\pi m}{d}\right) d\lambda,
\end{aligned} \tag{11.1}$$

where the last equality follows from the Poisson summation formula. The integral over λ is now easily carried out using the property of the Dirac delta function:

$$\begin{aligned}
\mathbf{P}_s^{(H,l)}(\mathbf{T},\mathbf{S}) = \sum_{n=-\infty}^{-2}\sum_{m=-\infty}^{\infty} \frac{\pi}{d\kappa^l}\left(\chi_m-\alpha_m\right)^l \frac{e^{-\chi_m(y-y_0-n\eta)-\kappa_0 n\eta}}{\chi_m} \\
\cdot e^{i\alpha_m(x-x_0-n\xi)} e^{i\alpha_0 n\xi},
\end{aligned} \tag{11.2}$$

where

$$\alpha_m = \alpha_0 + \frac{2\pi m}{d}, \qquad \chi_m = \sqrt{\alpha_m^2-\kappa^2}. \tag{11.3}$$

Exchanging the order of summation and summing over a geometric series in n leads to

$$\begin{aligned}
\mathbf{P}_s^{(H,l)}(\mathbf{T},\mathbf{S}) &= \frac{\pi}{d\kappa^l}\sum_{m=-\infty}^{\infty} \frac{\left(\chi_m-\alpha_m\right)^l}{\chi_m} e^{-\chi_m(y-y_0)+i\alpha_m(x-x_0)} \frac{e^{-2Q_m}}{1-e^{-Q_m}} \\
&= \frac{\pi}{d}\sum_{m=-\infty}^{\infty}\left(\frac{\kappa}{\chi_m+\alpha_m}\right)^l \frac{1}{\chi_m} e^{-\chi_m(y-y_0)+i\alpha_m(x-x_0)} \frac{e^{-2Q_m}}{1-e^{-Q_m}}
\end{aligned} \tag{11.4}$$

where

$$Q_m = \chi_m\eta + \kappa\eta - i\left((\alpha_m-\alpha_0)\xi\right). \tag{11.5}$$

By observing the exponential factor on the numerator, we know the Helmholtz kernel will decay slower than the Yukawa kernel. Also, we may face a convergence issue because when $\alpha_m < \kappa$, χ_m is purely imaginary (for real κ). Decay doesn't begin until $\alpha_m > \kappa$, which means Helmholtz will take more M-terms to converge for the south and north parts of summation.

The north part $\mathbf{P}_n^{(H,l)}$ can be analysed in an almost identical fashion.

We now analyse the west part. We obtain

$$\begin{aligned}
\mathbf{P}_w^{(H,l)}(\mathbf{T},\mathbf{S}) &= \sum_{m=-\infty}^{-m_0}\sum_{n=-1}^{1} K_l\left(i\kappa R_{mn}\right) e^{il\theta_{mn}} e^{i\mathbf{k}_0\cdot\mathbf{L}_{mn}} \\
&= \sum_{m=-\infty}^{-m_0}\sum_{n=-1}^{1} \frac{1}{2(i\kappa)^l}\int_{-\infty}^{\infty}\left(\sqrt{\lambda^2-\kappa^2}+\lambda\right)^l \frac{e^{-\sqrt{\lambda^2-\kappa^2}(x-x_0-md-n\xi)}}{\sqrt{\lambda^2-\kappa^2}} \\
&\cdot e^{i\lambda(y-y_0-n\eta)} e^{i(\alpha_0 md+\alpha_0 n\xi+i\kappa_0 n\eta)} d\lambda \\
&= \frac{1}{2(i\kappa)^l}\sum_{n=-1}^{1}\int_{-\infty}^{\infty}\left(\sqrt{\lambda^2-\kappa^2}+\lambda\right)^l \frac{e^{-\sqrt{\lambda^2-\kappa^2}(x-x_0-n\xi)}}{\sqrt{\lambda^2-\kappa^2}} \\
&\cdot e^{i\lambda(y-y_0-n\eta)} e^{i(\alpha_0 n\xi-i\kappa n\eta)} \frac{e^{-m_0\left(\sqrt{\lambda^2-\kappa^2}+i\alpha_0\right)d}}{1-e^{-\left(\sqrt{\lambda^2-\kappa^2}+i\alpha_0\right)d}} d\lambda,
\end{aligned} \tag{11.6}$$

where the third equality follows from summing a geometric series over m. The expression for the east part $\mathbf{P}_e^{(H,l)}$ can be obtained similarly. Also if we choose to rotate the coordinates to avoid excluding 21 cells at high shear rate, we will need to generate more quadrature nodes and weights for the west and east parts of summation.

In the second project of the dissertation, We have designed two efficient and accurate algorithms based on the standard generalized Gaussian quadrature rule, which is more efficient than the standard GGQ. We have introduced and implemented this new GGQ and efficient three-panel generalized Gaussian quadrature rule which can be used to evaluate double-layer potentials with high order accuracy. We have used this new panel-based quadrature rule to compute nodes and weights for Helmholtz problem with an interior boundary condition. Comparing the classic generalized Gaussian quadrature rule, our numerical results shows that

we are using fewer nodes in three-panel rule to achieve the same level of accuracy.

Furthermore, there are some key observations of the three-panel rule that we can make. First, by getting rid of the endpoint singularities, we can integrate more accurately. Second, the merged three panel rule provides a more efficient quadrature rule. Third, we can say the three panel rule and standard GGQ are equally stable with respect to high frequency and complicated geometry. Also, the low-order rule should be used with caution because it is accurate to a certain point but not always stable. Finally, our numerical experiments indicate our three-panel converges within less panels and cost less quadrature nodes on each panel.

Here we only had our new panel-based quadrature rule tested with the weakly singular kernel. In the future, we should test our new panel-based quadrature rule on singular and hypersingular integrals.

APPENDIX A

ROTATED PLANE-WAVE EXPANSIONS FOR THE EAST AND WEST PARTS OF THE DOUBLY PERIODIC PERIODIZING OPERATORS

In the analysis and implementation of the present paper, we have relied on plane-wave expansions that decay in x: either for $x > 0$ (the west part) or for $x < 0$ (the east part). Simple geometric considerations led to the conclusion that we may need to exclude the central 7×3 copies of the unit cell. For non-rectangualr unit cells, it is actually more efficient to align the decay direction in the plane-wave expansion with $\hat{\mathbf{e}}_2^{\perp}$ - that is, orthogonal to the $\hat{\mathbf{e}}_2$ direction. We illustrate the corresponding algorithm in the case of the modified Helmholtz kernel. Consider the coordinate transformation

$$\begin{pmatrix} \tilde{x} \\ \tilde{y} \end{pmatrix} = \begin{pmatrix} \cos\theta & -\sin\theta \\ \sin\theta & \cos\theta \end{pmatrix} \begin{pmatrix} x \\ y \end{pmatrix}. \tag{A.1}$$

In complex notation, this is equivalent to

$$\tilde{x} + i\tilde{y} = e^{i\theta}(x + iy). \tag{A.2}$$

Let us also write

$$\tilde{\xi} + \tilde{\eta} = e^{i\theta}(\xi + i\eta), \quad \tilde{d}_x + i\tilde{d}_y = de^{i\theta}. \tag{A.3}$$

For the west part, if the plane-wave expansion along the $\tilde{x}$ direction is used, we have

$$\begin{aligned} K_2^{west}(\mathbf{t}, \mathbf{s}) &= \frac{1}{2\pi} \sum_{m=-\infty}^{-(m_0+1)} \sum_{n=-1}^{1} K_0\left(\mathbf{t}, \mathbf{s} + \mathbf{l}_{mn}\right) \\ &= \sum_{m=-\infty}^{-(m_0+1)} \sum_{n=-1}^{1} \int_{-\infty}^{\infty} \frac{e^{-\sqrt{\lambda^2+\beta^2}(\tilde{x}-\tilde{x}'-m\tilde{d}_x-n\tilde{\xi})}}{4\pi\sqrt{\lambda^2+\beta^2}} \cdot e^{i\lambda(\tilde{y}-\tilde{y}'-m\tilde{d}_y-n\tilde{\eta})} d\lambda \\ &= \sum_{n=-1}^{1} \int_{-\infty}^{\infty} \frac{e^{-\sqrt{\lambda^2+\beta^2}(\tilde{x}-\tilde{x}'-n\tilde{\xi})}}{4\pi\sqrt{\lambda^2+\beta^2}} \cdot e^{i\lambda(\tilde{y}-\tilde{y}'-n\tilde{\eta})} \frac{e^{-(m_0+1)\left(\sqrt{\lambda^2+\beta^2}\tilde{d}_x - i\lambda\tilde{d}_y\right)}}{1 - e^{-\left(\sqrt{\lambda^2+\beta^2}\tilde{d}_x - i\lambda\tilde{d}_y\right)}} d\lambda. \end{aligned} \tag{A.4}$$

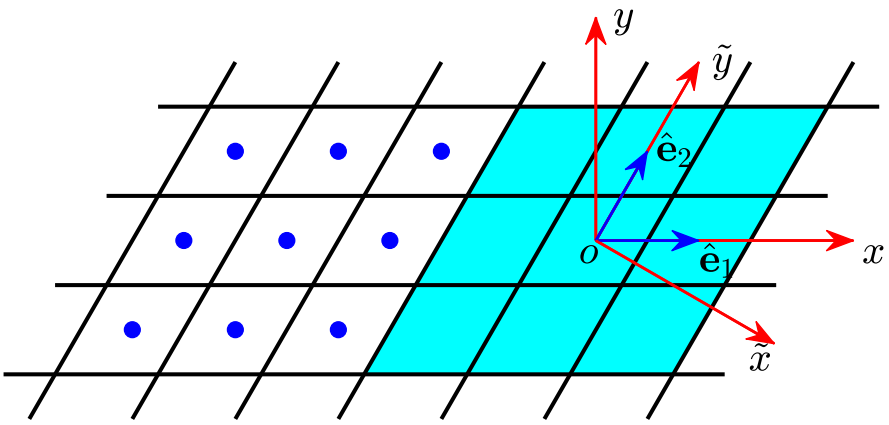

Figure A.1 New direction of the plane-wave expansion for the west part. In the main text, we have chosen the plane-wave expansions along the coordinate axes for all four parts. The advantage is that the east and west parts of the doubly periodic periodizing operators can be discretized via efficient precomputed generalized Gaussian quadrature. But the worst case requires the exclusion of the center 7×3 cells from the periodizing operators. If we choose the plane-wave expansion along the $\tilde{x}$-axis, then one only needs to exclude the center 3×3 cells from the doubly periodic periodizing operators. But the number of plane waves may increase if the angle between $\hat{\mathbf{e}}_1$ and $\hat{\mathbf{e}}_2$ is very small and $|\hat{\mathbf{e}}_2|$ is very close to $|\hat{\mathbf{e}}_1|$.

It is now clear that if we choose $\mathbf{e}_{\tilde{x}} = \hat{\mathbf{e}}_2^{\perp}$ - that is, we choose θ such that $\tilde{\xi} = 0$ and $\tilde{d}_x > 0$, then $m_0 = 1$ is sufficient to ensure that the decaying exponential in the integrand decays at least as fast as $e^{-\sqrt{\lambda^2+\beta^2}\tilde{d}_x}$. Thus, one only needs to exclude the center 3×3 cells from the periodizing operator rather than the larger near region we have used above. The integrand could still be highly oscillatory, so that an effective high-order quadrature is needed, just as in singly periodic case.

APPENDIX B

PERIODIZING OPERATORS FOR THE MODIFIED HELMHOLTZ EQUATION WITH MULTIPOLE SOURCES

The multipole of order l for the modified Helmholtz multipole is defined by $K_l(\beta r)e^{il\theta}$, where K_l the modified Bessel function of the second kind of order l. The following lemma describes the corresponding plane-wave expansions for the far-field contributions of the periodizing operators.

Lemma 1. *For the standard unit cell $\mathcal{C}$ discussed in the main text, let K_2^{south}, K_2^{north}, K_2^{west}, K_2^{east} denote the far-field parts of the periodizing operator for a multipole source of order l governed by the modified Helmholtz equation subject to doubly periodic boundary conditions. That is,*

$$\begin{aligned}
K_2^{south}(\mathbf{t},\mathbf{s}) &= \sum_{n=-\infty}^{-2}\sum_{m=-\infty}^{\infty} K_l(\mathbf{t},\mathbf{s}+\mathbf{l}_{mn})e^{il\theta_{mn}},\\
K_2^{north}(\mathbf{t},\mathbf{s}) &= \sum_{n=2}^{\infty}\sum_{m=-\infty}^{\infty} K_l(\mathbf{t},\mathbf{s}+\mathbf{l}_{mn})e^{il\theta_{mn}},\\
K_2^{west}(\mathbf{t},\mathbf{s}) &= \sum_{n=-1}^{1}\sum_{m=-\infty}^{-4} K_l(\mathbf{t},\mathbf{s}+\mathbf{l}_{mn})e^{il\theta_{mn}},\\
K_2^{east}(\mathbf{t},\mathbf{s}) &= \sum_{n=-1}^{1}\sum_{m=4}^{\infty} K_l(\mathbf{t},\mathbf{s}+\mathbf{l}_{mn})e^{il\theta_{mn}}.
\end{aligned} \tag{B.1}$$

Let α_m, χ_m and Q_m be given by Equation 4.5. Then

$$
\begin{aligned}
K_2^{south}(\mathbf{t},\mathbf{s}) &= \frac{\pi i^l}{d}\sum_{m=-\infty}^{\infty}\left(\frac{\beta}{\chi_m+\alpha_m}\right)^l \frac{1}{\chi_m} e^{-\chi_m(y-y')+i\alpha_m(x-x')}\frac{e^{-2Q_m}}{1-e^{-Q_m}}\,,\\
K_2^{north}(\mathbf{t},\mathbf{s}) &= \frac{\pi(-i)^l}{d}\sum_{m=-\infty}^{\infty}\left(\frac{\chi_m+\alpha_m}{\beta}\right)^l \frac{1}{\chi_m} e^{\chi_m(y-y')+i\alpha_m(x-x')}\frac{e^{-2\overline{Q_m}}}{1-e^{-\overline{Q_m}}}\,,\\
K_2^{west}(\mathbf{t},\mathbf{s}) &= \frac{1}{2\beta^l}\sum_{n=-1}^{1}\int_{-\infty}^{\infty}\left(\sqrt{\lambda^2+\beta^2}+\lambda\right)^l \frac{e^{-\sqrt{\lambda^2+\beta^2}(x-x'-n\xi)}}{\sqrt{\lambda^2+\beta^2}}\\
&\quad\cdot e^{i\lambda(y-y'-n\eta)}\frac{e^{-4\sqrt{\lambda^2+\beta^2}d}}{1-e^{-\sqrt{\lambda^2+\beta^2}d}}d\lambda\,,\\
K_2^{east}(\mathbf{t},\mathbf{s}) &= \frac{(-1)^l}{2\beta^l}\sum_{n=-1}^{1}\int_{-\infty}^{\infty}\left(\sqrt{\lambda^2+\beta^2}-\lambda\right)^l \frac{e^{\sqrt{\lambda^2+\beta^2}(x-x'-n\xi)}}{\sqrt{\lambda^2+\beta^2}}\\
&\quad\cdot e^{i\lambda(y-y'-n\eta)}\frac{e^{-4\sqrt{\lambda^2+\beta^2}d}}{1-e^{-\sqrt{\lambda^2+\beta^2}d}}d\lambda\,.
\end{aligned}
\tag{B.2}
$$

Similarly, for the singly periodic case,

$$
\begin{aligned}
K_1^{west}(\mathbf{t},\mathbf{s}) &= \sum_{m=-\infty}^{-2} K_l(\mathbf{t},\mathbf{s}+(md,0))e^{il\theta_{m0}},\\
&= \frac{1}{2\beta^l}\int_{-\infty}^{\infty}\left(\sqrt{\lambda^2+\beta^2}+\lambda\right)^l \frac{e^{-\sqrt{\lambda^2+\beta^2}(x-x')}}{\sqrt{\lambda^2+\beta^2}}\\
&\quad\cdot e^{i\lambda(y-y')}\frac{e^{-2\sqrt{\lambda^2+\beta^2}d}}{1-e^{-\sqrt{\lambda^2+\beta^2}d}}d\lambda\,,\\
K_1^{east}(\mathbf{t},\mathbf{s}) &= \sum_{m=2}^{\infty} K_l(\mathbf{t},\mathbf{s}+(md,0))e^{il\theta_{m0}}\\
&= \frac{(-1)^l}{2\beta^l}\int_{-\infty}^{\infty}\left(\sqrt{\lambda^2+\beta^2}-\lambda\right)^l \frac{e^{\sqrt{\lambda^2+\beta^2}(x-x')}}{\sqrt{\lambda^2+\beta^2}}\\
&\quad\cdot e^{i\lambda(y-y')}\frac{e^{-2\sqrt{\lambda^2+\beta^2}d}}{1-e^{-\sqrt{\lambda^2+\beta^2}d}}d\lambda\,.
\end{aligned}
\tag{B.3}
$$

The preceding result yields the following low-rank decompositions for the periodizing operators.

Lemma 2. *Under the hypotheses of Theorem 4.1 and Theorem 4.3, let*

$$\mathbf{L}^{south}, \mathbf{L}^{north} \in \mathbb{C}^{N_T\times(2M+1)}$$

and $\mathbf{R}^{south}, \mathbf{R}^{north} \in \mathbb{C}^{(2M+1)\times N_S}$ *be dense matrices defined in Equation 4.6 and Equation 4.13, and let* $\mathbf{L}_1^{west} \in \mathbb{C}^{N_T \times 2N_q^1}$, $\mathbf{L}_2^{west} \in \mathbb{C}^{N_T \times 2N_q^2}$, $\mathbf{R}_1^{west} \in \mathbb{C}^{2N_q^1 \times N_S}$, $\mathbf{R}_2^{west} \in \mathbb{C}^{2N_q^2 \times N_S}$ *be dense matrices defined in Equation 4.17. Furthermore, let* $\mathbf{D}^{south}, \mathbf{D}^{north} \in \mathbb{C}^{(2M+1)\times(2M+1)}$ *be diagonal matrices with*

$$\begin{aligned}
\mathbf{D}^{south}(m,m) &= \frac{\pi i^l}{d}\left(\frac{\beta}{\chi_m+\alpha_m}\right)^l \frac{1}{\chi_m}\frac{e^{-2Q_m}}{1-e^{-Q_m}}\,, \\
\mathbf{D}^{north}(m,m) &= \frac{\pi(-i)^l}{d}\left(\frac{\chi_m+\alpha_m}{\beta}\right)^l \frac{1}{\chi_m}\frac{e^{-2\overline{Q_m}}}{1-e^{-\overline{Q_m}}}\,,
\end{aligned} \tag{B.4}$$

and let $\mathbf{D}_1^{west}, \mathbf{D}_1^{east}$, *and* $\mathbf{D}_2^{west}$, $\mathbf{D}_2^{east}$ *be diagonal matrices of dimension* $2N_q^1$ *and* $2N_q^2$, *respectively, with*

$$\begin{aligned}
\mathbf{D}_1^{west}(n,n) &= \frac{1}{2\beta^l}\left(\sqrt{\lambda_{n,1}^2+\beta^2}+\lambda_{n,1}\right)^l \frac{w_{n,1}}{\sqrt{\lambda_{n,1}^2+\beta^2}}\frac{e^{-2\sqrt{\lambda_{n,1}^2+\beta^2}d}}{1-e^{-\sqrt{\lambda_{n,1}^2+\beta^2}d}}\,, \\
\mathbf{D}_1^{east}(n,n) &= \frac{(-1)^l}{2\beta^l}\left(\sqrt{\lambda_{n,1}^2+\beta^2}-\lambda_{n,1}\right)^l \frac{w_{n,1}}{\sqrt{\lambda_{n,1}^2+\beta^2}}\frac{e^{-2\sqrt{\lambda_{n,1}^2+\beta^2}d}}{1-e^{-\sqrt{\lambda_{n,1}^2+\beta^2}d}}\,, \\
\mathbf{D}_2^{west}(n,n) &= \frac{1}{2\beta^l}\left(\sqrt{\lambda_{n,2}^2+\beta^2}+\lambda_{n,2}\right)^l \frac{w_{n,2}}{\sqrt{\lambda_{n,2}^2+\beta^2}}\frac{e^{-4\sqrt{\lambda_{n,2}^2+\beta^2}d}}{1-e^{-\sqrt{\lambda_{n,2}^2+\beta^2}d}} \\
&\quad \cdot\left[e^{-\sqrt{\lambda_{n,2}^2+\beta^2}\xi+i\lambda_{n,2}\eta}+e^{\sqrt{\lambda_{n,2}^2+\beta^2}\xi-i\lambda_{n,2}\eta}+1\right], \\
\mathbf{D}_2^{east}(n,n) &= \frac{(-1)^l}{2\beta^l}\left(\sqrt{\lambda_{n,2}^2+\beta^2}-\lambda_{n,2}\right)^l \frac{w_{n,2}}{\sqrt{\lambda_{n,2}^2+\beta^2}}\frac{e^{-4\sqrt{\lambda_{n,2}^2+\beta^2}d}}{1-e^{-\sqrt{\lambda_{n,2}^2+\beta^2}d}} \\
&\quad \cdot\left[e^{-\sqrt{\lambda_{n,2}^2+\beta^2}\xi-i\lambda_{n,2}\eta}+e^{\sqrt{\lambda_{n,2}^2+\beta^2}\xi+i\lambda_{n,2}\eta}+1\right],
\end{aligned} \tag{B.5}$$

where $\lambda_{-n,1} = -\lambda_{n,1}$ *for* $n = 1, \ldots, N_q^1$, *and* $\lambda_{-n,2} = -\lambda_{n,2}$ *for* $n = 1, \ldots, N_q^2$. *Then, the periodizing operators for the modified Helmholtz multipole of order* l *are*

given by

$$
\begin{aligned}
\mathbf{P}_2^{south} &= \mathbf{L}^{south}\,\mathbf{D}^{south}\,\mathbf{R}^{south} + O(\epsilon),\\
\mathbf{P}_2^{north} &= \mathbf{L}^{north}\,\mathbf{D}^{north}\,\mathbf{R}^{north} + O(\epsilon),\\
\mathbf{P}_2^{west} &= \mathbf{L}_2^{west}\,\mathbf{D}_2^{west}\,\mathbf{R}_2^{west} + O(\epsilon),\\
\mathbf{P}_2^{east} &= \mathbf{L}_2^{east}\,\mathbf{D}_2^{east}\,\mathbf{R}_2^{east} + O(\epsilon),\\
\mathbf{P}_1^{west} &= \mathbf{L}_1^{west}\,\mathbf{D}_1^{west}\,\mathbf{R}_1^{west} + O(\epsilon),\\
\mathbf{P}_1^{east} &= \mathbf{L}_1^{east}\,\mathbf{D}_1^{east}\,\mathbf{R}_1^{east} + O(\epsilon).
\end{aligned}
\tag{B.6}
$$

APPENDIX C

PERIODIZING OPERATORS FOR THE LAPLACE EQUATION WITH MULTIPOLE SOURCES

In two dimensions, using complex variables notation, the Laplace multipole of order l is simply $1/z^l$. Here we identify $\mathbf{t}$ with $z = x + iy$, $\mathbf{s}$ with $z' = x' + iy'$, $\hat{\mathbf{e}}_1$ with $e_1 = d$, $\hat{\mathbf{e}}_2$ with $e_2 = \xi + i\eta$, and $\mathbf{l}_{mn}$ with $z_{mn} = m \cdot e_1 + n \cdot e_2$. The following lemma contains the plane-wave expansions for the far-field parts of the corresponding periodic kernels.

Lemma 3. *For the standard unit cell $\mathcal{C}$ discussed in the main text, let K_2^{south}, K_2^{north}, K_2^{west}, K_2^{east} denote the far-field parts of the periodizing operator for a multipole source of order l governed by the Laplace equation subject to doubly periodic boundary conditions. That is,*

$$\begin{aligned}
K_2^{south}(\mathbf{t},\mathbf{s}) &= \sum_{n=-\infty}^{-2}\sum_{m=-\infty}^{\infty}\frac{1}{(z-z'-z_{mn})^l},\\
K_2^{north}(\mathbf{t},\mathbf{s}) &= \sum_{n=2}^{\infty}\sum_{m=-\infty}^{\infty}\frac{1}{(z-z'-z_{mn})^l},\\
K_2^{west}(\mathbf{t},\mathbf{s}) &= \sum_{n=-1}^{1}\sum_{m=-\infty}^{-4}\frac{1}{(z-z'-z_{mn})^l},\\
K_2^{east}(\mathbf{t},\mathbf{s}) &= \sum_{n=-1}^{1}\sum_{m=4}^{\infty}\frac{1}{(z-z'-z_{mn})^l}.
\end{aligned} \tag{C.1}$$

Let $Q_m = 2\pi m(\eta - i\xi)/d$. Then

$$\begin{aligned}
K_2^{south}(\mathbf{t},\mathbf{s}) &= \frac{(-2\pi i)^l}{(l-1)!d^l}\sum_{m=1}^{\infty} m^{l-1}e^{i\frac{2\pi m}{d}(z-z')}\frac{e^{-2Q_m}}{1-e^{-Q_m}} + \delta_{l1}\frac{\pi i}{d\eta}y,\\
K_2^{north}(\mathbf{t},\mathbf{s}) &= \frac{(2\pi i)^l}{(l-1)!d^l}\sum_{m=1}^{\infty} m^{l-1}e^{-i\frac{2\pi m}{d}(z-z')}\frac{e^{-2\overline{Q_m}}}{1-e^{-\overline{Q_m}}} + \delta_{l1}\frac{\pi i}{d\eta}y,\\
K_2^{west}(\mathbf{t},\mathbf{s}) &= \frac{1}{(l-1)!}\int_0^{\infty}\lambda^{l-1}\left(1+e^{\lambda\cdot e_2}+e^{-\lambda\cdot e_2}\right)e^{-\lambda(z-z')}\frac{e^{-4\lambda d}}{1-e^{-\lambda d}}d\lambda,\\
K_2^{east}(\mathbf{t},\mathbf{s}) &= \frac{(-1)^l}{(l-1)!}\int_0^{\infty}\lambda^{l-1}\left(1+e^{\lambda\cdot e_2}+e^{-\lambda\cdot e_2}\right)e^{\lambda(z-z')}\frac{e^{-4\lambda d}}{1-e^{-\lambda d}}d\lambda.
\end{aligned} \tag{C.2}$$

Similarly, for the singly periodic case,

$$
\begin{aligned}
K_1^{west}(\mathbf{t},\mathbf{s}) &= \sum_{m=-\infty}^{-2} \frac{1}{(z-z'-z_{mn})^l} \\
&= \frac{1}{(l-1)!}\int_0^\infty \lambda^{l-1} e^{-\lambda(z-z')} \frac{e^{-2\lambda d}}{1-e^{-\lambda d}} d\lambda, \\
K_1^{east}(\mathbf{t},\mathbf{s}) &= \sum_{m=2}^{\infty} \frac{1}{(z-z'-z_{mn})^l} \\
&= \frac{(-1)^l}{(l-1)!}\int_0^\infty \lambda^{l-1} e^{\lambda(z-z')} \frac{e^{-2\lambda d}}{1-e^{-\lambda d}} d\lambda.
\end{aligned}
\tag{C.3}
$$

The derivation of the associated periodizing operators is straightforward and omitted. Note that the integrals in Equation C.2 and Equation C.3 diverge at the origin when $l = 1$, but the divergence is compensated for in the associated periodizing operators under the assumption of charge neutrality.

APPENDIX D

PERIODIZING OPERATORS FOR THE STOKES STRESSLET

The stresslet for the Stokes equation is defined by the formula

$$T_{ijk}^{(S)}(\mathbf{t},\mathbf{s}) = \frac{\partial G_{ij}^{(S)}(\mathbf{t},\mathbf{s})}{\partial x_k} + \frac{\partial G_{jk}^{(S)}(\mathbf{t},\mathbf{s})}{\partial x_i} - p_j(\mathbf{t},\mathbf{s})\delta_{jk}, \tag{D.1}$$

where $G_{ij}^{(S)}$ is the ij-th component of the Stokeslet in Equation 7.1, p_j is the jth component of the pressurelet in Equation 7.12, and the partial derivatives are with respect to the source point $\mathbf{s}$. It is inconvenient to write down the periodizing operators for the stresslet due to its tensor structure. In practice, it is often combined with a vector $\mathbf{n}$ to form the kernel of the double layer potential operator or its adjoint operator, when $\mathbf{n} = (n_1, n_2)$ is the unit normal vector at the source point $\mathbf{s}$ or the target point $\mathbf{t}$, respectively. Thus, we will write down the periodizing operators for the kernel $\mathbf{D}^{(S)}$ of the double layer potential operator defined by the formula $D_{ij}^{(S)} = T_{jik}^{(S)} n_k$ instead.

Lemma 4. *For the standard unit cell $\mathcal{C}$ discussed in the main text, let K_2^{south}, K_2^{north}, K_2^{west}, K_2^{east} denote the far-field parts of the periodizing operator for the kernel of the Stokes double layer potential subject to doubly periodic boundary conditions. That is,*

$$\begin{aligned}
K_2^{south}(\mathbf{t},\mathbf{s}) &= \sum_{n=-\infty}^{-2}\sum_{m=-\infty}^{\infty} \mathbf{D}^{(S)}(\mathbf{t},\mathbf{s}+\mathbf{l}_{mn}),\\
K_2^{north}(\mathbf{t},\mathbf{s}) &= \sum_{n=2}^{\infty}\sum_{m=-\infty}^{\infty} \mathbf{D}^{(S)}(\mathbf{t},\mathbf{s}+\mathbf{l}_{mn}),\\
K_2^{west}(\mathbf{t},\mathbf{s}) &= \sum_{n=-1}^{1}\sum_{m=-\infty}^{-4} \mathbf{D}^{(S)}(\mathbf{t},\mathbf{s}+\mathbf{l}_{mn}),\\
K_2^{east}(\mathbf{t},\mathbf{s}) &= \sum_{n=-1}^{1}\sum_{m=4}^{\infty} \mathbf{D}^{(S)}(\mathbf{t},\mathbf{s}+\mathbf{l}_{mn}).
\end{aligned} \tag{D.2}$$

Let $\alpha_m = 2\pi m/d$ and $Q_m = 2\pi m(\eta - i\xi)/d$. Then

$$\mathbf{K}_2^{south}(\mathbf{t},\mathbf{s}) = \frac{y}{2d\eta}\begin{bmatrix} n_2 & n_1 \\ n_1 & n_2 \end{bmatrix} + \frac{1}{2d}\sum_{\substack{m=-\infty \\ m\neq 0}}^{\infty}\left\{\begin{bmatrix} 2i\,\mathrm{sign}(m)n_1 - n_2 & -n_1 \\ -n_1 & -n_2 \end{bmatrix}\right.$$
$$\left. -(i\alpha_m n_1 - |\alpha_m| n_2)\left(y - y' + \frac{2 - e^{-Q_m}}{1 - e^{-Q_m}}\eta\right)\begin{bmatrix} 1 & i\,\mathrm{sign}(m) \\ i\,\mathrm{sign}(m) & -1 \end{bmatrix}\right\}$$
$$\cdot \frac{e^{-2Q_m}}{1 - e^{-Q_m}} e^{-|\alpha_m|(y-y') + i\alpha_m(x-x')},$$
$$\mathbf{K}_2^{north}(\mathbf{t},\mathbf{s}) = \frac{y}{2d\eta}\begin{bmatrix} n_2 & n_1 \\ n_1 & n_2 \end{bmatrix} + \frac{1}{2d}\sum_{\substack{m=-\infty \\ m\neq 0}}^{\infty}\left\{\begin{bmatrix} 2i\,\mathrm{sign}(m)n_1 + n_2 & n_1 \\ n_1 & n_2 \end{bmatrix}\right.$$
$$\left. -(i\alpha_m n_1 + |\alpha_m| n_2)\left(y - y' - \frac{2 - e^{-\overline{Q_m}}}{1 - e^{-\overline{Q_m}}}\eta\right)\begin{bmatrix} -1 & i\,\mathrm{sign}(m) \\ i\,\mathrm{sign}(m) & 1 \end{bmatrix}\right\}$$
$$\cdot \frac{e^{-2\overline{Q_m}}}{1 - e^{-\overline{Q_m}}} e^{|\alpha_m|(y-y') + i\alpha_m(x-x')},$$
(D.3)

$$\mathbf{K}_2^{west}(\mathbf{t},\mathbf{s}) = \frac{1}{4\pi}\sum_{n=-1}^{1}\int_{-\infty}^{\infty}\frac{e^{-4|\lambda|d}}{1 - e^{-|\lambda|d}} e^{-|\lambda|(x-x'-n\xi)} e^{i\lambda(y-y'-n\eta)} \cdot \left\{\begin{bmatrix} -n_1 & -n_2 \\ -n_2 & -n_1 + 2i\,\mathrm{sign}(\lambda)n_2 \end{bmatrix}\right.$$
$$\left. -(-|\lambda| n_1 + i\lambda n_2)\left(x - x' - n\xi + \frac{4 - 3e^{-|\lambda|d}}{1 - e^{-|\lambda|d}}d\right)\begin{bmatrix} -1 & i\,\mathrm{sign}(\lambda) \\ i\,\mathrm{sign}(\lambda) & 1 \end{bmatrix}\right\} d\lambda,$$
$$\mathbf{K}_2^{east}(\mathbf{t},\mathbf{s}) = \frac{1}{4\pi}\sum_{n=-1}^{1}\int_{-\infty}^{\infty}\frac{e^{-4|\lambda|d}}{1 - e^{-|\lambda|d}} e^{|\lambda|(x-x'-n\xi)} e^{i\lambda(y-y'-n\eta)} \cdot \left\{\begin{bmatrix} n_1 & n_2 \\ n_2 & n_1 + 2i\,\mathrm{sign}(\lambda)n_2 \end{bmatrix}\right.$$
$$\left. -(|\lambda| n_1 + i\lambda n_2)\left(x - x' - n\xi - \frac{4 - 3e^{-|\lambda|d}}{1 - e^{-|\lambda|d}}d\right)\begin{bmatrix} 1 & i\,\mathrm{sign}(\lambda) \\ i\,\mathrm{sign}(\lambda) & -1 \end{bmatrix}\right\} d\lambda.$$
(D.4)

Similarly, for singly periodic case,

$$
\begin{aligned}
\mathbf{K}_1^{west}(\mathbf{t},\mathbf{s}) &= \sum_{m=-\infty}^{-2} \mathbf{D}^{(S)}(\mathbf{t},\mathbf{s}+\mathbf{l}_{m0}), \\
&= \frac{1}{4\pi}\int_{-\infty}^{\infty} \frac{e^{-2|\lambda|d}}{1-e^{-|\lambda|d}} e^{-|\lambda|(x-x')} e^{i\lambda(y-y')} \cdot \left\{ \begin{bmatrix} -n_1 & -n_2 \\ -n_2 & -n_1 + 2i\,\mathrm{sign}(\lambda) n_2 \end{bmatrix} \right. \\
&\left. -(-|\lambda| n_1 + i\lambda n_2) \left(x - x' + \frac{2-e^{-|\lambda|d}}{1-e^{-|\lambda|d}} d \right) \begin{bmatrix} -1 & i\,\mathrm{sign}(\lambda) \\ i\,\mathrm{sign}(\lambda) & 1 \end{bmatrix} \right\} d\lambda, \\
\mathbf{K}_1^{east}(\mathbf{t},\mathbf{s}) &= \sum_{m=2}^{\infty} \mathbf{D}^{(S)}(\mathbf{t},\mathbf{s}+\mathbf{l}_{m0}), \\
&= \frac{1}{4\pi}\int_{-\infty}^{\infty} \frac{e^{-2|\lambda|d}}{1-e^{-|\lambda|d}} e^{|\lambda|(x-x')} e^{i\lambda(y-y')} \cdot \left\{ \begin{bmatrix} n_1 & n_2 \\ n_2 & n_1 + 2i\,\mathrm{sign}(\lambda) n_2 \end{bmatrix} \right. \\
&\left. -(|\lambda| n_1 + i\lambda n_2) \left(x - x' - \frac{2-e^{-|\lambda|d}}{1-e^{-|\lambda|d}} d \right) \begin{bmatrix} 1 & i\,\mathrm{sign}(\lambda) \\ i\,\mathrm{sign}(\lambda) & -1 \end{bmatrix} \right\} d\lambda.
\end{aligned}
\tag{D.5}
$$

REFERENCES

af Klinteberg, L. and Tornberg, A.-K. (2017). Error estimation for quadrature by expansion in layer potential evaluation. *Advances in Computational Mathematics*, 43(1):195–234.

Alpert, B. K. (1999). Hybrid gauss-trapezoidal quadrature rules. *SIAM Journal on Scientific Computing*, 20(5):1551–1584.

Askham, T., Gimbutas, Z., Greengard, L., Lu, L., O'Neil, M., Rachh, M., and Rokhlin, V. (2021). fmm2d software library. `https://github.com/flatironinstitute/fmm2d`.

Barnett, A. and Greengard, L. (2010). A new integral representation for quasi-periodic fields and its application to two-dimensional band structure calculations. *Journal of Computational Physics*, 229(19):6898–6914.

Barnett, A. and Greengard, L. (2011). A new integral representation for quasi-periodic scattering problems in two dimensions. *Tidskrift för Informationsbehandling Numerical Mathematics*, 51(1):67–90.

Barnett, A. and Magland, J. (2018). Non-uniform fast Fourier transform library of types 1, 2, 3 in dimensions 1, 2, 3. `https://github.com/ahbarnett/finufft`.

Barnett, A., Magland, J., and af Klinteberg, L. (2019). A parallel non-uniform fast Fourier transform library based on an "exponential of semicircle" kernel. *SIAM Journal on Scientific Computing*, 41:C479–C504.

Barnett, A. H., Marple, G. R., Veerapaneni, S., and Zhao, L. (2018). A unified integral equation scheme for doubly periodic laplace and stokes boundary value problems in two dimensions. *Communications on Pure and Applied Mathematics*, 71(11):2334–2380.

Berman, C. L. and Greengard, L. (1994). A renormalization method for the evaluation of lattice sums. *Journal of Mathematical Physics*, 35(11):6036–6048.

Bloch, F. (1928). Über die quantenmechanik der elektronen in kristallgittern. *Zeitschrift für Physik*, 52:555–600.

Bremer, J., Gimbutas, Z., and Rokhlin, V. (2010a). A nonlinear optimization procedure for generalized Gaussian quadratures. *SIAM Journal on Scientific Computing*, 32(4):1761–1788.

Bremer, J., Gimbutas, Z., and Rokhlin, V. (2010b). A nonlinear optimization procedure for generalized gaussian quadratures. *SIAM Journal on Scientific Computing*, 32(4):1761–1788.

Cheng, H., Greengard, L., and Rokhlin, V. (1999). A fast adaptive multipole algorithm in three dimensions. *Journal of Computational Physics*, 155(2):468–498.

Cheng, H., Huang, J., and Leiterman, T. J. (2006). An adaptive fast solver for the modified Helmholtz equation in two dimensions. *Journal of Computational Physics*, 211(2):616–637.

Colton, D. L. and Kress, R. (1983). *Integral equation methods in scattering theory*. Pure and Applied Mathematics. Wiley, New York.

Davis, P. J. and Rabinowitz, P. (1984). *Methods of Numerical Integration*. Academic Press, Orlando, 2nd edition.

Denlinger, R., Gimbutas, Z., Greengard, L., and Rokhlin, V. (2017). A fast summation method for oscillatory lattice sums. *Journal of Mathematical Physics*, 58(2):023511.

Dienstfrey, A., Hang, F., and Huang, J. (2001). Lattice sums and the two-dimensional, periodic green's function for the helmholtz equation. *Proceedings of the Royal Society of London. Series A: Mathematical, Physical and Engineering Sciences*, 457(2005):67–85.

DLMF (2020). *NIST Digital Library of Mathematical Functions*. http://dlmf.nist.gov/, Release 1.0.27 of 2020-06-15. F. W. J. Olver, A. B. Olde Daalhuis, D. W. Lozier, B. I. Schneider, R. F. Boisvert, C. W. Clark, B. R. Miller, B. V. Saunders, H. S. Cohl, and M. A. McClain, eds.

Dutt, A. and Rokhlin, V. (1993). Fast Fourier transforms for nonequispaced data. *SIAM Journal on Scientific Computing*, 14:1368–1393.

Dutt, A. and Rokhlin, V. (1995). Fast Fourier transforms for nonequispaced data. II. *Applied and Computational Harmonic Analysis*, 2:85–100.

Dym, H. and McKean, H. P. (1972). *Fourier Series and Integrals*. Academic Press, Cambridge, Massachusetts.

Enoch, S., McPhedran, R., Nicorovici, N., Botten, L., and Nixon, J. (2001). Sums of spherical waves for lattices, layers, and lines. *Journal of Mathematical Physics*, 42:5859–5870.

Epstein, C. L., Greengard, L., and Klockner, A. (2013). On the convergence of local expansions of layer potentials. *SIAM Journal on Numerical Analysis*, 51(5):2660–2679.

Ewald, P. (1921). Die berechnung optischer und elektrostatischer gitterpotentiale. *Annalen der Physik*, 64:253–287.

Fornberg, B. (1998). *A practical guide to pseudospectral methods*, volume 1. Cambridge University Press, Cambridge, United Kingdom.

Gan, Z., Jiang, S., Luijten, E., and Xu, Z. (2016). A hybrid method for systems of closely spaced dielectric spheres and ions. *SIAM Journal on Scientific Computing*, 38(3):B375–B395.

Gimbutas, Z. and Greengard, L. (2013). Fast multi-particle scattering: a hybrid solver for the Maxwell equations in microstructured materials. *Journal of Computational Physics*, 232:22–32.

Greengard, L. and Lee, J. (2004). Accelerating the nonuniform fast Fourier transform. *SIAM Review*, 46:443–454.

Greengard, L. and Rokhlin, V. (1987). A fast algorithm for particle simulations. *Journal of Computational Physics*, 73(2):325–348.

Greengard, L. and Rokhlin, V. (1997). A new version of the fast multipole method for the Laplace equation in three dimensions. *Acta Numerica*, 6:229–270.

Helsing, J. (2009). Integral equation methods for elliptic problems with boundary conditions of mixed type. *Journal of Computational Physics*, 228(23):8892–8907.

Helsing, J. and Holst, A. (2015). Variants of an explicit kernel-split panel-based nyström discretization scheme for helmholtz boundary value problems. *Advances in Computational Mathematics*, 41(3):691–708.

Hesthaven, J. S., Gottlieb, S., and Gottlieb, D. (2007). *Spectral methods for time-dependent problems*, volume 21. Cambridge University Press, Cambridge, United Kingdom.

Hrycak, T. and Rokhlin, V. (1998). An improved fast multipole algorithm for potential fields. *SIAM Journal on Scientific Computing*, 19:1804–1826.

Huang, J. (1999). Integral representations of harmonic lattice sums. *Journal of Mathematical Physics*, 40(10):5240–5246.

Jones, D. S. (1966). *Generalised functions*. McGraw-Hill, New York, NY.

Kapur, S. and Rokhlin, V. (1997). High-order corrected trapezoidal quadrature rules for singular functions. *SIAM Journal on Numerical Analysis*, 34(4):1331–1356.

Klöckner, A., Barnett, A., Greengard, L., and O'Neil, M. (2013). Quadrature by expansion: A new method for the evaluation of layer potentials. *Journal of Computational Physics*, 252:332–349.

Kress, R. (1991). Boundary integral equations in time-harmonic acoustic scattering. *Mathematical and Computer Modelling*, 15(3-5):229–243.

Lee, J. and Greengard, L. (2005). The type 3 nonuniform FFT and its applications. *Journal of Computational Physics*, 206:1–5.

Linton, C. M. (2010). Lattice sums for the helmholtz equation. *SIAM Review*, 52:630–674.

Liu, Y. and Barnett, A. H. (2016). Efficient numerical solution of acoustic scattering from doubly-periodic arrays of axisymmetric objects. *Journal of Computational Physics*, 324:226–245.

Ma, J., Rokhlin, V., and Wandzura, S. (1996). Generalized Gaussian quadrature rules for systems of arbitrary functions. *SIAM Journal on Numerical Analysis*, 33(3):971–996.

Malhotra, D. and Biros, G. (2015). PVFMM: a parallel kernel independent FMM for particle and volume potentials. *Communications in Computational Physics*, 18(3):808–830.

McPhedran, R., Nicorovici, N., Botten, L., and Grubits, K. (2000). Lattice sums for gratings and arrays. *Journal of Mathematical Physics*, 41(11):7808–7816.

Mikhlin, S. G. and Prossdorf, S. (1986). *Singular integral operators*. Springer–Verlag, Berlin, German.

Mores, P. and Feshbach, H. (1953). *Methods of theoretical physics, McGraw-Hill*. McGraw-Hill, New York, NY.

Moroz, A. (2006). Quasi-periodic Green's functions of the Helmholtz and Laplace equations. *Journal of Physics A: Mathematical and General*, 36:11247.

Olver, F. W. J., Lozier, D. W., Boisvert, R. F., and Clark, C. W., editors (2010). *NIST Handbook of Mathematical Functions*. Cambridge University Press, Cambridge, United Kingdom.

Otani, Y. and Nishimura, N. (2008). A periodic FMM for Maxwell's equations in 3D and its applications to problems related to photonic crystals. *Journal of Computational Physics*, 227(9):4630–4652.

Rayleigh, L. (1892). On the influence of obstacles arranged in rectangular order upon the properties of a medium. *Philosophical Magazine*, 34:481–502.

Sommerfeld, A. and Strauss, E. G. (1949). *Partial Differential Equations in Physics*. The Academic Press, New York, NY.

Stakgold, I. (1968). *Boundary value problems of mathematical physics*. Macmillan, New York, NY.

Trefethen, L. N. (2008). Is gauss quadrature better than clenshaw–curtis? *SIAM Review*, 50(1):67–87.

Wang, H. and Xiang, S. (2012). On the convergence rates of legendre approximation. *Mathematics of Computation*, 81(278):861–877.

Wang, J., Nazockdast, E., and Barnett, A. (2021). An integral equation method for the simulation of doubly-periodic suspensions of rigid bodies in a shearing viscous flow. *Journal of Computational Physics*, 424:109809.

Yan, W. and Shelley, M. (2018). Flexibly imposing periodicity in kernel independent FMM: A multipole-to-local operator approach. *Journal of Computational Physics*, 335:214–232.

Yarvin, N. and Rokhlin, V. (1998). Generalized Gaussian quadratures and singular value decompositions of integral operators. *SIAM Journal on Scientific Computing*, 20(2):699–718.

Ying, L., Biros, G., and Zorin, D. (2004). A kernel-independent adaptive fast multipole algorithm in two and three dimensions. *Journal of Computational Physics*, 196:591–626.